

4n Raman Microscopy

4n-ramanmicroscopie

Alejandro Diaz Tormo



**UNIVERSITEIT
GENT**

**Promotor: prof. dr. ir. N. Le Thomas
Proefschrift ingediend tot het behalen van de graad van
Doctor in de ingenieurswetenschappen: fotonica**

**Vakgroep Informatietechnologie
Voorzitter: prof. dr. ir. B. Dhoedt
Faculteit Ingenieurswetenschappen en Architectuur
Academiejaar 2019 - 2020**

ISBN 978-94-6355-295-0
NUR 950
Wettelijk depot: D/2019/10.500/103



Universiteit Gent
Faculteit Ingenieurswetenschappen en Architectuur
Vakgroep Informatietechnologie

Promotor:

Prof. Dr. Ir. Nicolas Le Thomas

Examencommissie:

| | |
|--|--|
| Prof. Dr. Ir. Patrick De Baets (voorzitter) | Universiteit Gent, INTEC |
| Prof. Dr. Ir. Nicolas Le Thomas (promotor) | Universiteit Gent, INTEC |
| Prof. Andre Skirtach | Universiteit Gent, Dep. of Biotechnology |
| Prof. Dr. Ir. Roel Baets | Universiteit Gent, INTEC |
| Prof. Dr. Ir. Filip Beunis | Universiteit Gent, INTEC |
| Prof. Dr. Ir. Iwan Moreels | Universiteit Gent, Dep. of Chemistry |
| Dr. Didier Beghuin | Lambda-x, Belgium |
| Prof. Dr. Simon-Pierre Gorza | Université Libre de Bruxelles |
| Prof. Dr. Wolfgang Langbein | Cardiff University, School of Physics |

Universiteit Gent
Faculteit Ingenieurswetenschappen en Architectuur
Vakgroep Informatietechnologie
Technologiepark Zwijnaarde 126, 9052 Gent, België

Proefschrift tot het behalen van de graad van
Doctor in de ingenieurswetenschappen: fotonica
Academiejaar 2019-2020

Acknowledgements

This PhD is the result of the support from many people in Ghent, but also from other places. With the following words I would like to thank each and everyone of you, my colleagues, friends and family for your help, advice and support.

First and foremost, I would like to express my deepest gratitude to my supervisor *Nicolas* for guiding me and for the opportunity to learn at his side during these years. You were always willing to discuss whenever I showed up at your office and a fundamental support when I was a bit troubled. *Andre*, thanks for all the motivating discussions and your help in the lab. I also want to express my gratitude to the jury members of this thesis for providing valuable comments to improve this manuscript.

Dmitry, we've been struggling with the measurements together until late hours. It has been a challenging journey for both of us, but I am sure you will graduate soon and I am looking forward to reading your thesis.

There is something about the *Photonics Research Group* I will always remember. Despite the vast number of colleagues that have been part of the group at some point or another, I still felt that they worried about me at a professional level, but also at a personal level. *Nicolas* has been helping me figure out my next professional steps, I appreciate you worrying so much. *Dries*, thanks for considering that I could be of any help in the optomechanics challenge. *Roel*, thanks to you I could spend some extra time writing this manuscript and learn about microfluidics. Perhaps a bit fortuitously, you introduced me to the role of photonics in near-eye displays for virtual reality glasses, which quickly became one of my passions.

During the last months of this PhD I've been helping my fellow colleagues with their measurements as a lab assistant. *Bart* was so kind to think about me to put some order in the labs when Jasper could not be around. Another proof of the social warmth that this group can offer. *Jasper*, I still remember that time biking together towards the city center. I was still talking to you when you suddenly disappeared from my sight. I looked back and you were dramatically falling to the ground. A bit shocking, but it turned out not to be too bad. It was a pleasure to work with such a chilled person.

I had a lot of fun working on the *Megachip* project lead by *Wim*. It was an outreach effort to show how photonic chips work, which took place during the Light Festival. And to the other professors in the group, *Geert*, *Gunther*, *Peter*, thanks for being so approachable and for putting your trust in my colleagues and I to keep pushing the group forwards. *Eva*, you were always willing to help me find the right connections. Thanks for listening to my crazy thoughts and for your advice. I am also thankful to the support and technical staff for selflessly helping all of us: *Ilse M.*, *Liesbet*, *Ilse V.R.*, *Michael* and *Steven*.

Our office got a bit of a fame for being the lunatic office. I like to think that everybody felt welcome to drop by and share their worries and happy stories. Very therapeutic actually. A lot of the blame for this lies on *Mr. Dhoore*, such an old-minded and at the same time fancy guy. He loves wearing pants that are 5 euros too short, and expensive shoes that he can't wear while driving because they would wrinkle. He is also a great fun even though he loves to complain about everything. It is actually great to see those two things come together, the fun and complaining parts, in the form of (sometimes) gifted impersonations. By the way, how are you doing with your Jupiter? Thanks for the all the Dutch translations in this thesis... ik weet het niet, meneer!

To my office mates —you will soon have a quieter office. I hope you will actually miss some of that noise. *Nicolas*, the Aggario and white-hole master. *Parabito*, a.k.a. *Xiaomin*, got that name because apparently that's what Spanish sounds like to him. *Java*, like the programming language! He taught me the real meaning of being a gentleman. We could spend long minutes yielding way to each other before going through any door. *Haolan*, the only adult in the office, and with a British accent. *Rodica*, even though she's been gone for some time, she left a big mark on us, in particulaaaaaaar....

Saurav, please stop spoiling the movies I haven't seen yet. He would spoil the movie or series completely but as soon as he realized he would just say: "Don't worry, it's all in the trailer!". *Sulaaaaaksshna*, *Sulaksssshnnna*, la la la, thanks for all those dinners. *Saurav* always joked around saying he actually cooked the meal that day, but I always knew it was you.

Floris, many great parties at your place. *Isaac*, get a proper app development software already. *Chonghuai*, ma'man! how is it going with the VPI? *Gregorio*, memorable trip to Baltimore, we survived! BEEEEEEEP! *Paul*, your jeans and your waistcoat made for a nice hike in the national parks of Cali. A carbonized fiber also pops in my mind. Good luck, *Ali*!

To my former Master colleagues and people from the office next door —*Arturo*, not everybody knows about your great voice, when is your performance? *Koen*, hope you're doing well in the US. *Yufei*, have you been practicing the Floss dance move? *Kasper*, why do you get startled when you are looking for somebody in an office... and you actually find that person? *Lukas*, keep up the darts training.

Antonio and *Federico*, Planjeeeeeeeeeeeeee!!! They say I do not properly pronounce the name of this amazing pub, but now they do not know any other way. Best DJ in town, but perhaps somebody should tell him to stop playing with the lights.

Zuyang, at some point we ended up literally digging in the trash container looking for a lost component. To our surprise, we found it! Thanks *Pieter* and *Daan* for your help in the PIXAPP project even after you left the group.

To my everyday companions and partners in crime —*Patraña*, I'm still waiting for your promised visit and for that trip to Serbia. *Aleeesio!*, my ping-pong archenemy and responsible for my philosophical drift towards the simultaneous fullness and emptiness of life. Is your optical table pumped yet? *Marghe*, charming, cheerful and one of the best friends I could wish for. I won't forget your comment during the hike in Luxemburg about 'tastes'.... just mind-blooming! *Nina Malina*, thanks for letting us mess up your place so many times. And finally *Masmus*, hoe gaat het met jouw???!!!! Eeeeeeh, have you been able to...? So many trips and weird but funny experiences, let's keep that up. Thanks for putting all the commas in this thesis.

To the other companions that I wish joined more often. —*Savvina*, 'Can I ask you something... It's kind of private?'. *Mimis*, actually you also like to ask if you can ask something, is it a Greek custom? *Omaricio*, there is an IPA waiting for your visit, as well as the 'barritos a espichar'. *Nuria*, my only Spanish companion left in the group. *Banana*, wish you the best in Germany. *Clemencio*, did you get those knobs greased? *Joan*, I still owe you some of that white wine (or should I say vinegar) we squeezed together.

Andrú, just to emphasize: I had a really nice and unforgettable time in Uganda with your friends, family (still not sure if the driver is included here), *Jesper*, *Camilo*, *Dana*... Thanks for treating us like family there.

To the ping-pong guys that lift my spirit almost everyday —*Kristofio*, maaaa-aaaaaan! What a dirty player! It's a good thing I can always trust your serve. *Irfam*, just give him a random word and he will make an 'amazing' joke out of it. How was the dancing last Friday? *Ewoud*, sssssscoca! *Jurun*, thanks meneer for letting me be the semi-automatic setup responsible. *Stijn*, the typical guy wearing shorts in winter. *Abdul*, as a special guy you deserve a special mention. An unbeatable ping pong player but only when he doesn't drink coffee, when he is not wearing his heavy shoes, when the pallet is not too bumpy, when the light from the window is not too bright... Thanks for all the office visits, deep and varied discussions, and for checking my PC screen every single time.

Joris and *Malaria*, my dearest neighbours who always invited me for dinner and to chat at their terrace. If you ever get to know them ask about the story of how we met.

Martin and *Lize*, we shared so many stories: The Mode Locks and all of its misunderstood pieces of art, Colombia hiju..., Cityboyboy, la patineta, the hobbit house with the shower in the kitchen, Cuba, Couleur Café, the players at the ginebritas place, st. Andrews and all of his dramas, Havana Bar, Good Moooorning! Alejaaaaandro..... and so so many others. Thanks guys for all the good memories and the ones to come.

Lastly, I would like to thank my family for their constant support and words of encouragement. ¡Gracias familia! ¡Y un beso enorme a mi sobrina *Lena*, que al amor nos condena!

Ghent, June 2019
Alejandro Diaz Tormo

Contents

| | |
|---|-------------|
| Acknowledgements | i |
| Contents | v |
| Samenvatting | xiii |
| Summary | xix |
| 1 Introduction | 1-1 |
| 1.1 Background and rationale | 1-1 |
| 1.2 Thesis outline | 1-3 |
| 1.3 Attribution of work | 1-4 |
| 1.4 Publications | 1-6 |
| 1.4.1 Publications in international journals | 1-6 |
| 1.4.2 Publications in international conferences | 1-6 |
| 1.4.3 Publications in national conferences | 1-7 |
| 2 Fundamentals of 4π Raman Microscopy | 2-1 |
| 2.1 Introduction | 2-2 |
| 2.2 Raman microscopy | 2-3 |
| 2.2.1 Classical theory of Raman scattering | 2-4 |
| 2.2.1.1 First-order induced electric dipole | 2-4 |
| 2.2.1.2 Selection rules | 2-8 |
| 2.3 4π Microscopy | 2-10 |

| | | |
|----------|---|------------|
| 2.3.1 | Signal Enhancement | 2-13 |
| 2.3.2 | The phase problem | 2-13 |
| 2.3.3 | Secondary lobes | 2-14 |
| 2.3.4 | Commercial availability | 2-16 |
| 2.3.5 | State of the art | 2-18 |
| 2.4 | Conclusion | 2-19 |
| 3 | Implementation of the Microscope Setup | 3-1 |
| 3.1 | Introduction | 3-2 |
| 3.2 | Mach-Zehnder vs. Michelson Interferometry | 3-4 |
| 3.3 | Description of the 4π Raman Optical Setup | 3-6 |
| 3.3.1 | Isolator | 3-8 |
| 3.3.2 | Partial reflector | 3-10 |
| 3.4 | Stabilization and phase control | 3-11 |
| 3.4.1 | Phase linearization | 3-11 |
| 3.4.1.1 | Different optical modes | 3-14 |
| 3.4.1.2 | 3x3 splitter | 3-14 |
| 3.4.1.3 | Off-axis interferogram | 3-15 |
| 3.4.1.4 | Phase modulation | 3-15 |
| 3.4.1.5 | Dedicated wavelength | 3-17 |
| 3.4.2 | Stabilization in the 4π Raman microscope | 3-17 |
| 3.4.2.1 | Axial scans | 3-20 |
| 3.5 | Conclusion | 3-22 |
| 4 | Nanolayers & Super-resolution | 4-1 |
| 4.1 | Introduction | 4-1 |
| 4.2 | Interaction between a standing wave pattern and a nanolayer | 4-3 |
| 4.2.1 | Raman contrast and detection visibility | 4-4 |
| 4.2.2 | Silicon membrane | 4-7 |

| | | |
|----------|--|------------|
| 4.3 | Super-resolution 4π Raman microscopy | 4-10 |
| 4.3.1 | Phase shifting super-resolution principle in three steps . . . | 4-11 |
| 4.3.2 | Experimentally super-resolving a stack of nanolayers . . . | 4-11 |
| 4.4 | Conclusion | 4-18 |
| 5 | Imaging of Biological Samples | 5-1 |
| 5.1 | Introduction | 5-1 |
| 5.2 | Point spread function characterization | 5-2 |
| 5.3 | 4π Raman Imaging of HeLa cells | 5-6 |
| 5.4 | Conclusion | 5-12 |
| 6 | A New Modality for the 4π Raman Microscope: Quantitative Phase | 6-1 |
| 6.1 | Introduction | 6-2 |
| 6.2 | Combining 4π Raman with quantitative phase microscopy | 6-3 |
| 6.2.1 | Solving the 4π phase problem | 6-4 |
| 6.2.2 | Principle of sample-induced quantitative phase retrieval . . . | 6-6 |
| 6.2.3 | State of the art of quantitative phase microscopy | 6-8 |
| 6.2.4 | Phase calibration for quantitative measurements | 6-9 |
| 6.2.5 | 4π Raman and quantitative phase microscopy on HeLa cells | 6-11 |
| 6.3 | Conclusions | 6-14 |
| 7 | Conclusion and Perspectives | 7-1 |
| 7.1 | Conclusion | 7-1 |
| 7.2 | Future perspectives | 7-2 |
| A | The Matrix Transfer Method to Analyze Multilayer Stacks | A-1 |
| | References | R-1 |

List of Acronyms

C

CaF₂
CARS

Calcium fluoride
Coherent Anti-Stokes Raman Spectroscopy

H

HBSS

Hanks' Balanced Salt Solution

N

NA

Numerical Aperture

O

OTF

Optical Transfer Function

P

| | |
|------|----------------------------------|
| PID | Proportional-Integral-Derivative |
| PMMA | Polymethyl methacrylate |
| PSF | Point Spread Function |

Q

| | |
|-----|-------------------------------|
| QPM | Quantitative Phase Microscopy |
|-----|-------------------------------|

S

| | |
|------------------|-------------------------------------|
| SERS | Surface-Enhanced Raman spectroscopy |
| Si | Silicon |
| SiO ₂ | Silicon dioxide |
| SRS | Stimulated Raman Scattering |
| STED | Stimulated Emission Depletion |

T

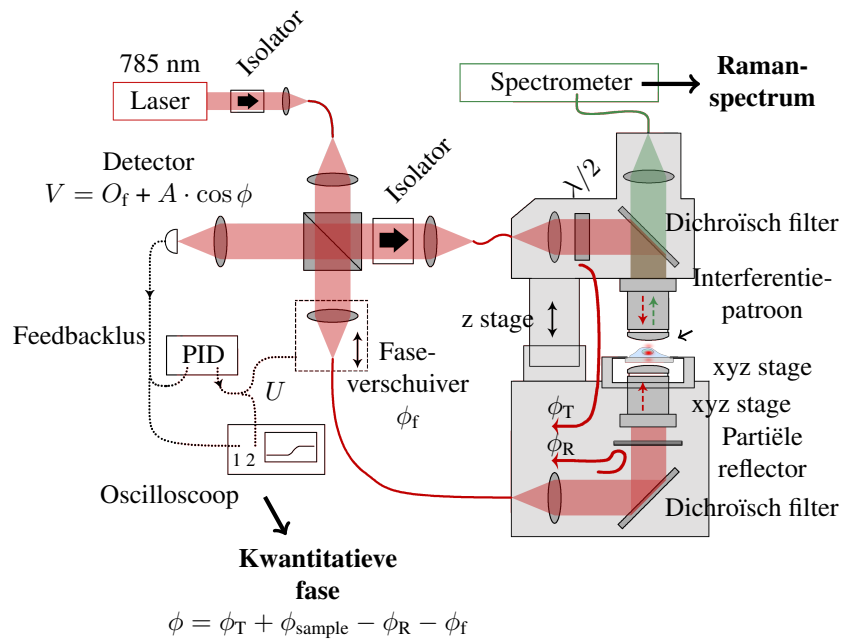
| | |
|------------------|------------------|
| TiO ₂ | Titanium dioxide |
|------------------|------------------|

Samenvatting

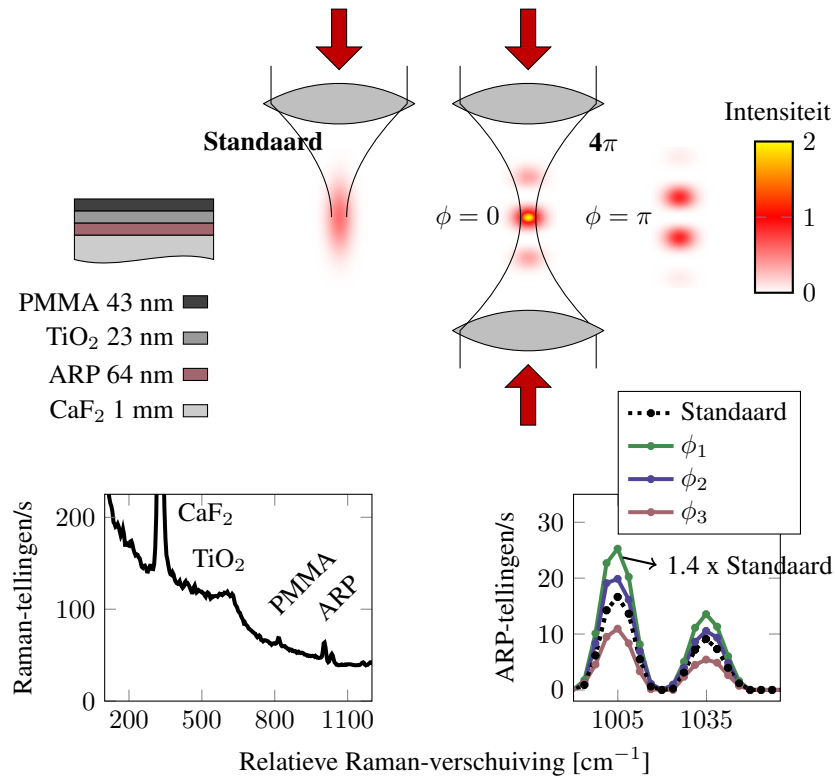
Tot 1992 konden microscopen alleen licht focussen in het transversale vlak, maar niet in de richting van voortplanting. Dat jaar was het experimenteel bewezen dat de spot verder langs de optische as kon worden gereduceerd door niet één, maar twee objectieve objectieven tegelijkertijd te gebruiken [1–4]. Dit resulteert in een resolutie die tot zeven maal beter is dan de conventionele resolutie [5, 6]. Er kan een bijna sferische spotgrootte met een typische diameter van 100-150 nm worden verkregen. Deze techniek wordt 4π -microscopie genoemd omdat deze de theoretische maximale ruimtehoek van de microscoop vergroot, voor zowel lichtexcitatie als -collectie, van 2π tot 4π steradianen.

4π -microscopie wordt reeds lang gebruikt om de optische resolutie in fluorescentiemicroscopie te verbeteren [2, 7, 8]. De benadering is echter niet beperkt tot fluorescentiemicroscopie —we demonstrenen in dit proefschrift dat het vergelijkbare voordelen kan bieden voor Raman-microscopie. We ontwikkelden een 4π Raman-microscoop, afgebeeld in Fig. 5, met betere ruimtelijke resolutie en een verbeterd Raman-signaal in vergelijking met standaard spontane Raman-microscopie. In een experiment met een nanolaagstapeling, geïllustreerd in Fig. 6, tonen we een 1.4-voudig groter Raman-signaal vergeleken met een standaard Raman-microscoop. Bovendien stelt de verschuiving van de relatieve fase ϕ tussen de pompbundels ons ook in staat om de (sub-golflengte) optische weglengte tussen nanolagen in de stapel te bepalen met een nauwkeurigheid van 6 nm. Belangrijk is dat deze techniek het mogelijk maakt om de verschillende nanolagen onafhankelijk en gelijktijdig te bestuderen, iets dat nauwelijks haalbaar is met technieken die normaal worden gebruikt voor dit soort metingen, zoals ellipsometrie.

De meest interessante toepassing van 4π -microscopie is echter de studie van biologische monsters. Het verkrijgen van veel Raman-spectra uit meerdere monsterpunten en over een breed gebied is essentieel voor het begrijpen van de fundamentele mechanismen, om te achterhalen waarom het monster abnormaal zou werken en wat we kunnen doen om het te verhelpen. Met andere woorden, beeldvorming is een essentiële functie van de microscoop en we waren in staat om voor de eerste keer een kleine subcomponent van een HeLa-cel te visualiseren. Dit wordt getoond in Fig. 7. We zouden ook een beeld dat werd verkregen door een standaard confocale Raman-microscoop kunnen vergelijken met onze 4π Raman-afbeelding. Helaas kon de toename van de axiale resolutie van 4π Raman-microscopie niet duidelijk wor-

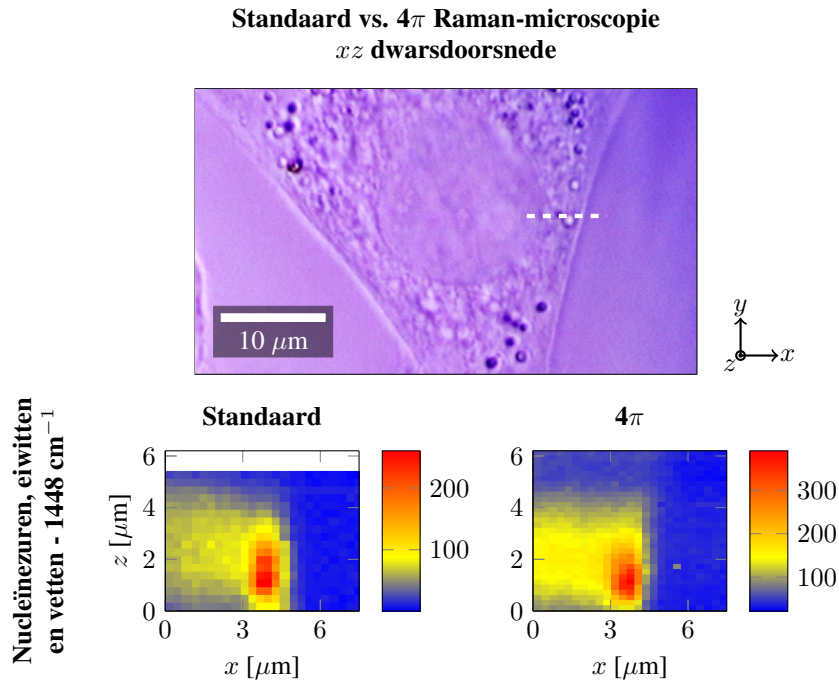


Figuur 1: Schematische weergave van de 4π Raman-microscop. De optische weglengte van de boven- en onderarmen naar de partiële reflector wordt respectievelijk aangegeven als ϕ_T en ϕ_R . De rode pijlen geven de lichtbundels aan die de detector zullen storen om het signaal $V = O_f + A \cdot \cos(\phi_T + \phi_{\text{sample}} - \phi_R - \phi_f)$ die afhankelijk is van de faseverschuiving tussen de bovenste en de onderste pompen, inclusief de invloed van het sample ϕ_{sample} en faseverschuiver ϕ_f . De Raman-spectra worden verkregen door de spectrometer en de fase-informatie door de detector die verbonden is met een feedbacklus.



Figuur 2: Experiment met de nanolaagstapel gemeten met 4π Raman-microscopie. Het voorbeeldschema staat links bovenaan. Een vergelijking tussen de spotgrootte van een standaard confocale en van de 4π -microscopie. De 4π spot wordt getoond wanneer beide pompen in fase $\phi = 0$ en uit fase $\phi = \pi$ zijn. Onderaan toont het volledige Raman-spectrum de verschillende materiële bijdragen. Rechts wordt een vergroting weergegeven van de ARP-top met verwijderde achtergrond. Een gestreepte zwarte lijn geeft het standaard confocale spectrum aan. Spectra bij verschillende faseverschuivingen tussen bundels ϕ_i hebben een kleurcode.

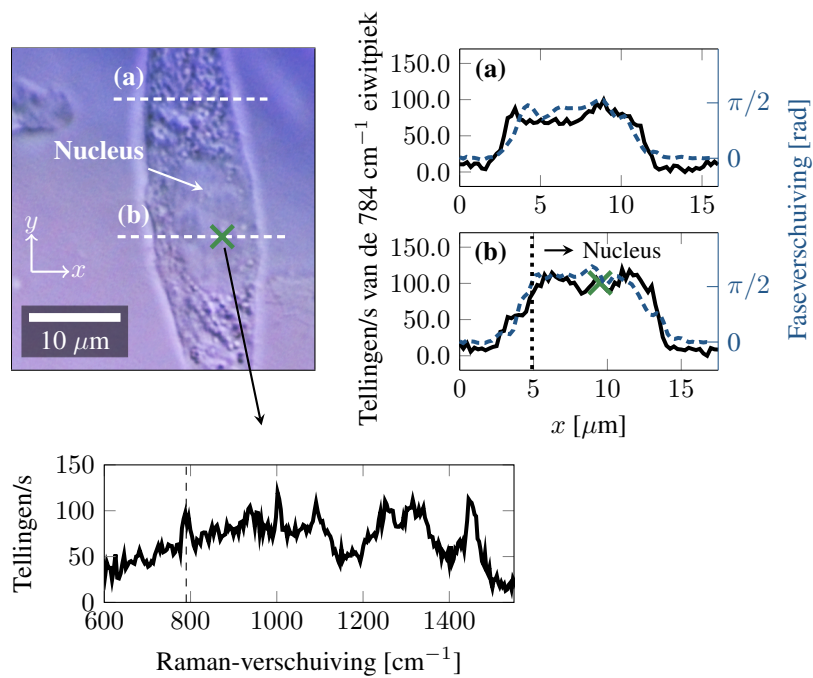
den aangetoond op dit biologische monster. Als bewijs van een principe-experiment heeft het ons echter helpen begrijpen dat het interferentiepatroon dat op het brandpunt is gecreëerd, niet ideaal is. Het bevat secundaire lobes naast de centrale piek die de kwaliteit van het beeld en de bereikbare 4π -resolutie belemmeren.



Figuur 3: Standaard en 4π -afbeelding van het xz dwarsdoorsnedevlak van een HeLa cel. De gegevens werden verkregen van het deel van de cel dat aangeduid is met een gestipte lijn op het zichtbaar beeld. De eenheid van de kleurstrook is Raman-tellingen per seconde.

Raman-spectroscopie analyseert de chemische samenstelling van biologische monsters met een resolutie beter dan $1\ \mu\text{m}$, maar vanwege het zwakke Raman-signaal zijn vaak lange acquisitietijden nodig. Om dynamische processen of grote monsters te bestuderen, zijn kortere acquisitietijden wenselijk. Onze 4π -microscopie kan, naast de Raman-gegevens, ook de fase-informatie van het monster ophalen. De snellere fasemodaliteit van onze microscopie kan aanvullende gegevens opleveren en zelfs de diagnose van bepaalde ziekten versnellen. De resultaten getoond in Fig. 8 tonen aan dat onze 4π microscopie zowel de Raman- als kwantitatieve fase-informatie van dezelfde bemonsterplaats kan opnemen. Het verkrijgen van beide gegevens met dezelfde tool biedt duidelijke voordelen omdat het praktische beperkingen voorkomt, zoals de afstemming tussen modaliteiten.

4π -microscopie biedt de beste axiale resolutie die mogelijk is met louter optische middelen. Binnen het fluorescentiemicroscopie-veld is het al een enabling



Figuur 4: Raman- en kwantitatieve fase-scans van een HeLa-cel. De afbeelding met het heldere veld wordt linksboven weergegeven. Onderaan wordt het Raman-spectrum weergegeven van de cel met belangrijke piek bij 784 cm^{-1} (stippelijijn). Rechts, Raman- en kwantitatieve fase-scans van twee spots van het monster aangegeven met gestreepte witte lijnen op het zichtbare beeld. De evolutie van de 784 cm^{-1} Raman-piek in de x -richting wordt in het zwart weergegeven. De bijbehorende Raman-tellingen per seconde worden aangegeven op de linker verticale as. De kwantitatieve fase van de respectieve scans wordt aangegeven met gestippelde blauwe curves en zijn gekoppeld aan de verticale as aan de rechterkant.

approach voor toepassingen van biologische beeldvorming en superresolutie [9–11]. Een van de belangrijkste nadelen van fluorescentie is dat het monster moet worden gelabeld met extrinsieke kleurstoffen, wat het experiment kan beïnvloeden. Zodra de uitdaging van het verwijderen van de secundaire lobes is aangepakt, zal 4π Raman-microscopie een vergelijkbaar pad volgen, alleen deze keer met het voordeel dat het labelvrij is.

Summary

Until 1992, microscopes could only focus light tightly in the transversal plane but not along the direction of propagation. That year, it was experimentally proven that the focal spot could be shrunk further along the optical axis by using not one, but two opposing objective lenses simultaneously [1–4]. The result is a resolution that is up to seven-fold better than the conventional resolution [5, 6]. Namely, an almost spherical focal spot of typically 100-150 nm in diameter can be achieved. This technique is dubbed 4π microscopy as it enlarges the theoretical maximum solid angle of the microscope, for light excitation and collection, from 2π to 4π steradians.

4π microscopy has long been used to improve the optical resolution in fluorescence microscopy [2, 7, 8]. The approach is, however, not limited to fluorescence microscopy—we demonstrate in this dissertation that it can bring similar benefits to Raman microscopy as well. We developed a 4π Raman microscope, depicted in Fig. 5, with better spatial resolution and enhanced Raman signal compared to standard spontaneous Raman microscopy. In an experiment with a nanolayer stack, illustrated in Fig. 6, we show a 1.4-fold larger Raman signal compared to a standard Raman microscope. Additionally, shifting the relative phase between pump beams, ϕ , also allows us to determine the sub-wavelength optical path length between nanolayers in the stack with a precision of 6 nm. Importantly, this technique allows studying the different nanolayers independently and simultaneously, something hardly feasible with techniques normally employed for this sort of measurements, such as ellipsometry.

The most interesting application of 4π microscopy, however, is the study of biological samples. Obtaining many Raman spectra from multiple sample points and over a broad area is key to understanding its inner mechanisms, why the sample might be acting abnormally and what we can do to remedy it. In other words, imaging is an essential ability of the microscope, and we were able to visualize for the first time a small subcomponent of a HeLa cell, which is shown in Fig. 7. We could compare an image obtained by a standard confocal Raman microscope with our 4π Raman image. Unfortunately, the increase of axial resolution of 4π Raman microscopy could not be clearly demonstrated on this biological sample. However, as a proof of principle experiment, it helped us understand that the interference pattern created at the focal spot is not ideal. It features secondary lobes besides the

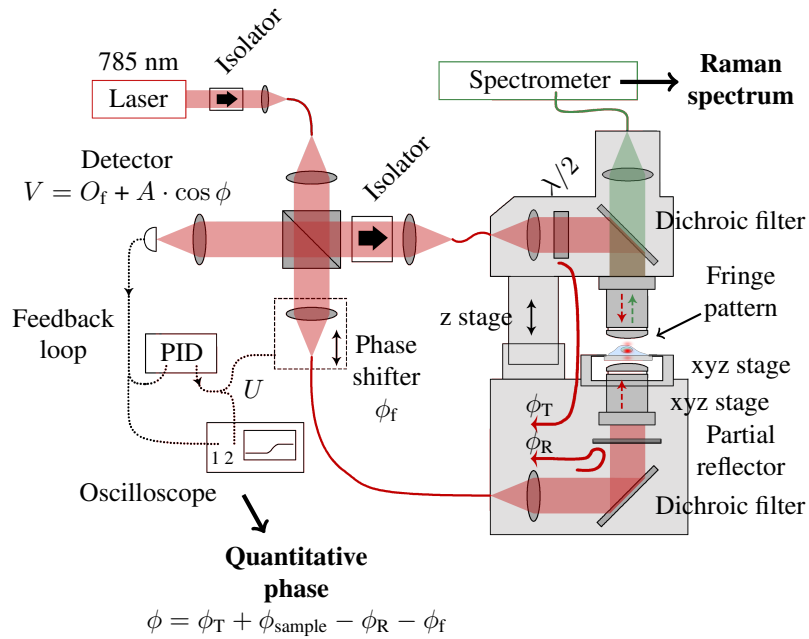


Figure 5: Schematic of the 4π Raman microscope. The optical path length of the top and bottom arms to the partial reflector is indicated as ϕ_T and ϕ_R , respectively. The red solid arrows indicate the beams that will interfere at the detector to produce the signal $V = O_f + A \cdot \cos(\phi_T + \phi_{\text{sample}} - \phi_R - \phi_f)$ that depends on the phase shift between top and bottom pump beams, including the influence of the sample ϕ_{sample} and phase shifter ϕ_f . The Raman spectra are obtained by the spectrometer and the phase information by the detector connected to a feedback loop.

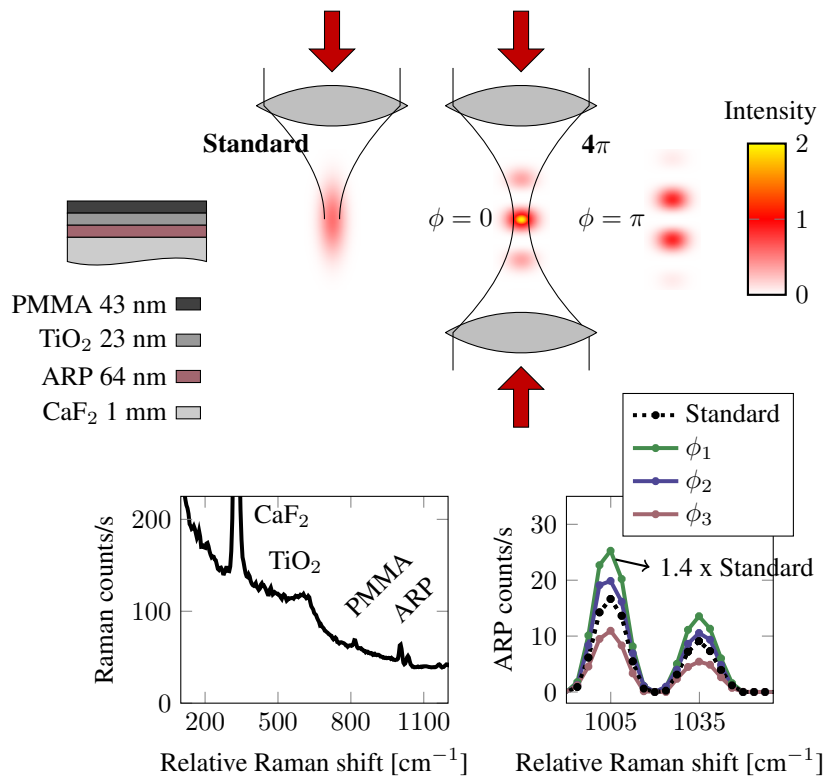


Figure 6: Experiment with the nanolayer stack measured by 4π Raman microscopy. The sample schematic is on the top left. A comparison between the focal spot of a standard confocal and the 4π microscope. The 4π spot is shown when both pump beams are in phase $\phi = 0$ and out of phase $\phi = \pi$. On the bottom the full Raman spectrum shows the different material contributions. To its right, a zoom-in of the ARP peaks with removed background is shown. A dashed black line indicates the standard confocal spectrum. Spectra at different phase shifts between beams ϕ_i are color coded.

central peak that hamper the quality of the image and the attainable 4π resolution.

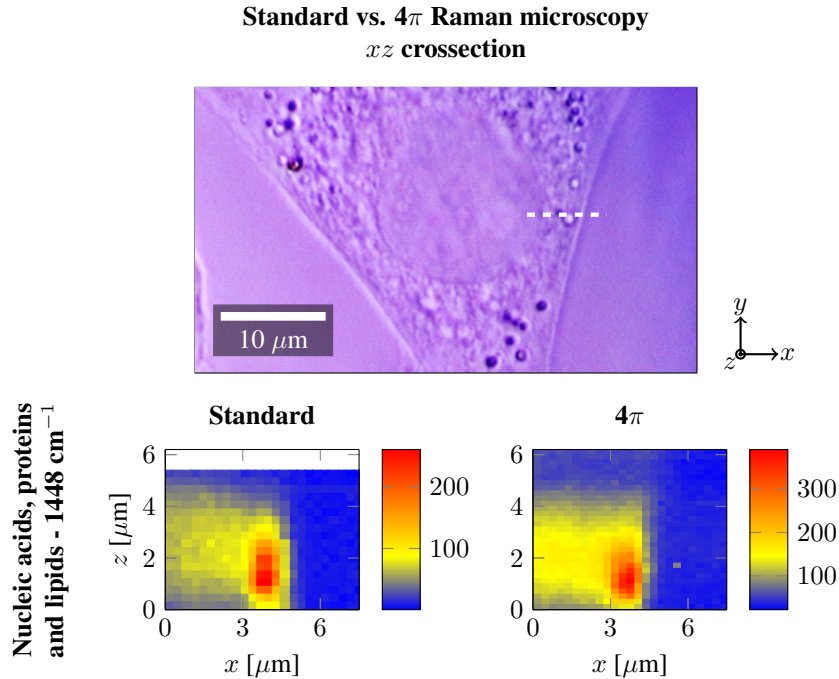


Figure 7: Standard and 4π image of the xz crosssectional plane of a HeLa cell. The data is obtained from the part of the cell indicated with a dashed line on the visible image. The colorbar has units of Raman counts per second.

Raman spectroscopy probes the chemical composition of biological samples with sub-micron resolution, however, due to the weak Raman signal it tends to require long acquisition times. To study dynamical processes or large samples, shorter acquisition times are desirable. Our 4π microscope, besides the Raman data, can also retrieve the phase information of the sample. The faster phase modality of our microscope can provide complementary data and even speed up the diagnosis of certain diseases. The results shown in Fig. 8 demonstrate that our 4π microscope can record both, the Raman and quantitative phase information, from the same sample spot. Obtaining both sets of data with the same tool offers clear benefits as it removes practical constraints, such as the alignment between modalities.

4π microscopy provides the best axial resolution possible by solely optical means. Within the fluorescence microscopy field, it is already an enabling approach for biological imaging and super-resolution applications [9–11]. One of the main drawbacks of fluorescence is that it requires the sample to be labeled with extrinsic dyes, and therefore, the experiment can be compromised. As soon as the challenge of removing the secondary lobes is tackled, 4π Raman microscopy is bound to

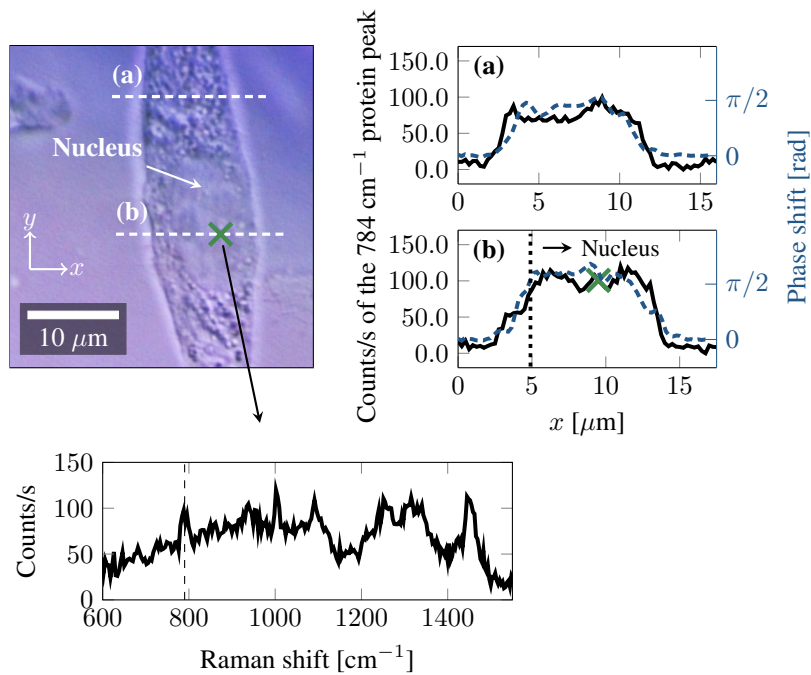


Figure 8: Raman and quantitative phase scans of a HeLa cell. On top left the bright-field image is shown. On the bottom, reference Raman spectrum of the cell where the peak of interest at 784 cm^{-1} is indicated with a dashed line. On the right, Raman and quantitative phase scans of two spots of the sample indicated with dashed white lines on the visible image. The evolution of the 784 cm^{-1} Raman peak in the x direction is plotted in black. The corresponding Raman counts per second are indicated on the left vertical axis. The quantitative phase of the respective scans is indicated with dashed blue curves and are linked to the vertical axis on the right.

follow a similar path, only this time with the advantage of being label-free.

1

Introduction

| | | |
|------------|---|------------|
| 1.1 | Background and rationale | 1-1 |
| 1.2 | Thesis outline | 1-3 |
| 1.3 | Attribution of work | 1-4 |
| 1.4 | Publications | 1-6 |
| 1.4.1 | Publications in international journals | 1-6 |
| 1.4.2 | Publications in international conferences | 1-6 |
| 1.4.3 | Publications in national conferences | 1-7 |

1.1 Background and rationale

The resolution of any optical system describes its ability to distinguish closely spaced features of the object being imaged. The wave nature of light means it is subject to diffraction, a phenomenon that does not allow it to be focused to an infinitely small point. This is the factor limiting the resolution in conventional optical systems, so it is said that they are diffraction-limited. Due to the limited set of angles at which the optical system can excite or collect light, diffraction sets the axial resolution to be around 3 times worse than in the transversal plane, but the advent of 4π microscopy [12] broke the conventional axial optical resolution limit. In order to obtain an isotropic and diffraction-limited resolution in every axis

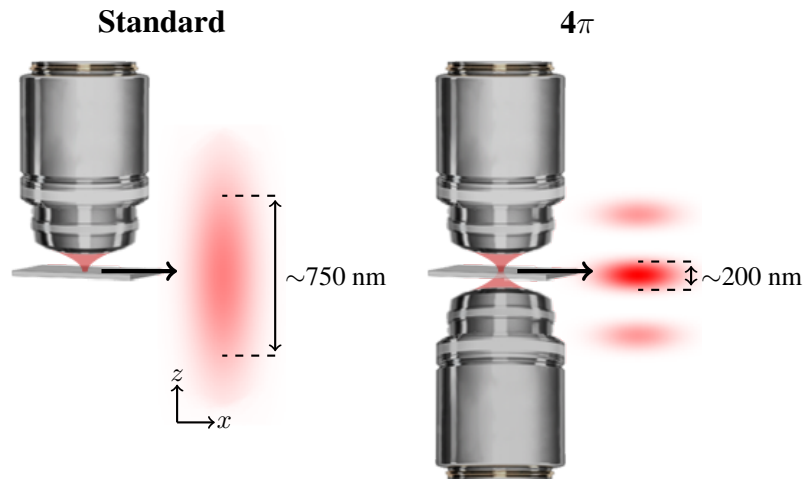


Figure 1.1: Comparison between a standard confocal (left) and a 4π (right) microscopy arrangement. The typical width of the point spread function in the axial direction can be up to 7 times smaller for the 4π microscope.

4π microscopy effectively increases the numerical aperture of the microscope by using two beams to excite the sample from opposite sides as illustrated in Fig. 1.1. Single objective lenses would ideally reach aperture angles of up to 180 degrees, corresponding to a 2π solid angle. Thus, the term 4π is a reference to the maximum solid angle possible, i.e., a solid angle twice as large as a single-lens microscope for excitation and/or detection.

The microscopy field has been steadily growing since the 1980s in terms of resolving power for living cell imaging thanks to the surge of a diverse new set of fluorescence super-resolution techniques, united under the name *fluorescence nanoscopy* [13, 14]. When the resolution of a microscope is smaller than the diffraction limit, approximately half the wavelength, then it is called a super-resolution microscope. Although diffraction is responsible for limiting the ability to distinguish two close objects, the precision at which we can localize those objects is not. Leveraging this idea, super-resolution fluorescence techniques can circumvent the spatial diffraction limit.

Diffraction might appear to be irrelevant for fluorescence nanoscopy techniques, but to the contrary, they greatly benefit from a 4π configuration and its tighter focusing of light. The resolution limit, rather than diffraction, is given by the performance of the fluorophores regarding their quantum efficiency, the number of emission cycles and by photobleaching. The higher collection efficiency of 4π microscopy is

therefore favourable for the resolution. As a result of the synergistic combination of 4π microscopy with fluorescence, nanoscopy techniques are currently the most light-efficient and the highest resolution approaches for three-dimensional live-cell imaging [9–11].

However, most biological samples do not exhibit intrinsic fluorescence, explaining the need for sample labelling with extrinsic fluorophores at the expense of perturbing the system under study [15, 16]. A competing approach is Raman microscopy, which offers intrinsic chemical selectivity as different molecules have specific vibrational frequencies. It allows visualizing the three dimensional chemical composition of biological specimens with high resolution in a noninvasive way, which is of high interest in the fields of biology, medicine and material sciences, among others. Nonetheless, due to the typically small Raman scattering cross-section, its extremely weak signal is the main drawback.

Raman microscopy [17, 18] is certainly following the same route as fluorescence techniques to attain super-resolved Raman images of cells, and new approaches are already being investigated [19–22]. 4π microscopy has long been used to enhance the resolution of fluorescence imaging, but it can be as beneficial to Raman microscopy. A Raman microscope with a 4π configuration has a great potential to help in the quest to achieve super-resolution Raman imaging and this is why we developed a novel configuration in 4π microscopy during this dissertation — 4π Raman microscopy.

Imaging biological samples, such as bacteria and cells, is probably the most attractive application for 4π Raman microscopy. Its finer resolution could help biologist clear some of the many unknowns around cell processes, and it could do so without extrinsic labels. During this work we demonstrated that our 4π microscope, besides Raman images, can also record quantitative phase information of the sample. Raman spectroscopy is a very powerful tool in the diagnosis of several diseases but its weak signal leads to long acquisition times, making it unsuited to study dynamical processes or large samples. The main role of quantitative phase microscopy can be to help obtain a quicker diagnosis as well as to provide complementary data that might be inaccessible through Raman imaging.

1.2 Thesis outline

This dissertation consists of 7 chapters. **Chapter 2** gives a theoretical overview of 4π Raman microscopy. It first describes Raman spectroscopy and then 4π microscopy, paying special attention to the state of the art. The main challenges of both techniques are discussed, highlighting two of them: the 4π phase problem and

the removal of the secondary lobes of the 4π point spread function.

Chapter 3 details the 4π Raman optical setup we designed and built during this dissertation. It tracks in a chronological order the changes and evolution of the microscope, from the first Mach-Zehnder interferometer to the final version of the tailored Sagnac interferometer that we now use as part of the 4π Raman microscope. Two key components of our interferometer are emphasized: an isolator in the interferometer and the use of a partial reflection to stabilize the phase between counter-propagating pump beams.

The ability of 4π Raman microscopy to provide super-resolution is discussed in **Chapter 4**. The study of a nanolayer stack will reveal the impact of the nanolayers' thickness on this ability and how 4π Raman microscopy can resolve sample features with a precision down to 6 nm under certain conditions.

Chapter 5 deals with the imaging capabilities of our 4π Raman microscope. An experiment with polystyrene nanoparticles serves us to characterize the microscope's point spread function and resolution. We then discuss the 4π Raman images obtained from biological samples and the current limitations of the system.

The consequences of optical aberrations and sample-induced phase shifts on the point spread function of the microscope are addressed on **Chapter 6**. We propose a method that compensates for the sample-induced phase shift and quantifies it, leading to a microscope with two modalities, 4π quantitative phase and Raman microscopy.

Finally, concluding remarks and a future outlook are formulated in **Chapter 7**.

1.3 Attribution of work

Under the supervision of Prof. Nicolas Le Thomas, the optical setup presented in this work was conceived and built by the author, as well as the electronic part of the setup used for the stabilization of the phase variations and the modifications done in the commercial Raman microscope. Similarly, the literature review, the automation of the measurements, all the simulations, theoretical calculations, modelling and processing of the 4π data shown in this work are also the result of the author's work.

The multiple biological and nanoparticle samples were prepared by our collaborator, Dmitry Khalenkow, in the biotechnology department of Ghent University, under the supervision of Prof. Andre G. Skirtach. D. Khalenkow was also present and helpful during the 4π measurements.

The ellipsometry measurements and corresponding data fitting were carried out by the author with help from Steven Verstuyft. The preparation of the layered samples was also carried out by the author together with Kumar Saurav. The profilometer measurements were carried out by the author under the guidance of Sören Dhoore.

1.4 Publications

This dissertation has led to the following list of publications in conferences and international peer-reviewed journals.

1.4.1 Publications in international journals

1. **A. Diaz Tormo**, D. Khalenkow, A. G. Skirtach, N. Le Thomas, “Raman and quantitative phase microscope with counter propagating beams demonstrated on HeLa cells”, *Continuum*, vol. 2, no. 3, pp. 797–804, 2019.
2. **A. Diaz Tormo**, D. Khalenkow, K. Saurav, A. G. Skirtach, N. Le Thomas, “Superresolution 4π Raman microscopy”, *Optics Letters*, vol. 42, no. 21, pp. 4410–4413, 2017.
3. Ming Xiao, Ziyang Hu, Zhao Wang, Yiwen Li, **A. Diaz Tormo**, N. Le Thomas, Boxiang Wang, Nathan C. Gianneschi, Matthew D. Shawley, Ali Dhinojwala, “Bioinspired Bright noniridescent photonic melanin supraballs”, *Science Advances*, vol. 3, no. 9, 2017.

1.4.2 Publications in international conferences

1. **A. Diaz Tormo**, D. Khalenkow, A. G. Skirtach, N. Le Thomas, “Multi-beam microscopy free of sample-induced phase distortions”, *Proceedings of the 23rd Annual Symposium of the IEEE Photonics Benelux Chapter*, Belgium, 2018.
2. **A. Diaz Tormo**, D. Khalenkow, A. G. Skirtach, N. Le Thomas, “ 4π Microscopy Immune to Sample-Induced Dephasing”, *IEEE Photonics Conference (IPC)*, United States, pp. 1-2 2018.
3. **A. Diaz Tormo**, D. Khalenkow, A. G. Skirtach, N. Le Thomas, “Study of bacterial inner structures with 4π Raman microscopy”, *Conference on Lasers and Electro-Optics (CLEO)*, United States, 2018.
4. **A. Diaz Tormo**, N. Le Thomas, “On-chip Axicon for Light Sheet Microscopy”, *Proceedings of the 20th Annual Symposium of the IEEE Photonics Benelux Chapter*, Belgium, 2015.

1.4.3 Publications in national conferences

1. **A. Diaz Tormo**, D. Khalenkow, A. G. Skirtach, N. Le Thomas, “Raman Microscopy with Two Counter-Propagating Beams”, *FEA Research Symposium*, Belgium, 2017.

2

Fundamentals of 4π Raman Microscopy

This chapter puts 4π Raman microscopy in context. It describes Raman and 4π microscopy in detail, from their strong points to their downsides, and discusses the state of the art. It mainly focuses on 4π fluorescence microscopy as it will bring a better understanding of the challenges involved in developing a 4π Raman microscope.

| | | |
|------------|--------------------------------------|-------------|
| 2.1 | Introduction | 2-2 |
| 2.2 | Raman microscopy | 2-3 |
| 2.2.1 | Classical theory of Raman scattering | 2-4 |
| 2.3 | 4π Microscopy | 2-10 |
| 2.3.1 | Signal Enhancement | 2-13 |
| 2.3.2 | The phase problem | 2-13 |
| 2.3.3 | Secondary lobes | 2-14 |
| 2.3.4 | Commercial availability | 2-16 |
| 2.3.5 | State of the art | 2-18 |
| 2.4 | Conclusion | 2-19 |

2.1 Introduction

Commercial optical objective lenses have precisely shaped surfaces to focus the light at a certain distance from it. For a given lens diameter, the closer the light is focused to the lens the better resolution it can provide. This is related to the concept of Numerical Aperture (NA), a dimensionless number that defines the range of angles over which the system can accept or emit light.

$$\text{NA} = n \sin \alpha \quad (2.1)$$

where n is the refractive index of the medium surrounding the lens, and α is the maximal angle of the cone of light that can enter or exit the lens with respect to the optical axis. Generally speaking, high NA systems feature a high optical resolution, meaning that light can be focused into a smaller spot compared to low NA systems.

The quality of an image is commonly separated into two factors, contrast and resolution. The resolution can be measured and mathematically described according to the geometry of the optical system. The contrast refers to the noise that limits the use of the available resolution. In fact, these two terms are strongly linked together. In a noisy measurement, the ideal resolution will not be obtained, so the effective resolution depends on the noise present in the measurement. We should then speak in terms of the more important factor defining the quality of an image, the signal-to-noise ratio. Yet, in this manuscript we will speak about the resolution as it is commonly done, without considering the noise influence over it.

The light intensity pattern delivered (or collected) by an optical system is called the Point Spread Function (PSF), and it defines the resolution thereof. Within the commonly employed paraxial approximation (i.e., for a small NA system), the PSF given by an objective lens with a circular pupil can be calculated in the focal plane as

$$\text{PSF}(\alpha) = \text{PSF}_0 \left[\frac{2J_1 \left(a \frac{2\pi}{\lambda} n \sin \alpha \right)}{a \frac{2\pi}{\lambda} n \sin \alpha} \right]^2 \quad (2.2)$$

The PSF_0 is the intensity at the central point, where $\text{PSF}(\alpha)$ has its maximum value. J_1 is the Bessel function of first kind and first order, a is the radius of the objective pupil and λ the wavelength of light. This formula is also known as the Airy pattern. Outside of the paraxial approximation, when the NA becomes large enough, the general form of the function remains the same. The main difference is that the zeros of $\text{PSF}(\alpha)$ do not actually reach a zero value.

A common way to define the resolution of an optical system is given by the Rayleigh criterion. It says that two point objects are just resolved if the centre of the first Airy pattern is superimposed on the first dark ring of the second pattern. Hence, we obtain that the transversal resolution for a given NA follows the equation

$$\Delta r = 0.61\lambda/\text{NA} \quad (2.3)$$

where Δr is also the Airy pattern radius, from the central peak to the first minimum.

There are many ways to define the axial resolution [23], based on different criteria and approximations. At low aperture angles, however, they all exhibit the following behaviour

$$\Delta z = \text{const.} \frac{n\lambda}{\text{NA}^2} \quad (2.4)$$

4π microscopy can be understood as an approach to improve the resolution by extending the numerical aperture. If a normal microscope can excite and collect light from one side of the sample, 4π microscopy can potentially collect and excite the sample from both sides, increasing the effective NA of the system. 4π microscopy has long been used to improve the optical resolution when imaging fluorescent samples. It is, however, not bounded to fluorescence microscopy—it can bring similar benefits to Raman microscopy as well. In this work we support this claim by developing a novel configuration in 4π microscopy: 4π Raman microscopy.

In the following sections we first describe what Raman spectroscopy is and then the 4π configuration that we will be using and discussing in the following chapters. A strong focus on 4π fluorescence microscopy and its state of the art will serve us to understand the challenges involved in 4π Raman microscopy.

2.2 Raman microscopy

Raman [17, 18, 24] spectroscopy is a widely used optical technique that provides chemical information about the sample under study. Molecules vibrate in different fundamental modes, as illustrated in Fig. 2.1, each mode having a corresponding vibrational frequency. The Raman effect thus offers intrinsic chemical selectivity as different molecules have specific vibrational frequencies, which is the main difference with fluorescence techniques. The large majority of biological molecules do not possess intrinsic fluorescence or it is very weak, hence the need to tag specific proteins with extrinsic fluorophores at the risk of perturbing the system under study [15, 16].

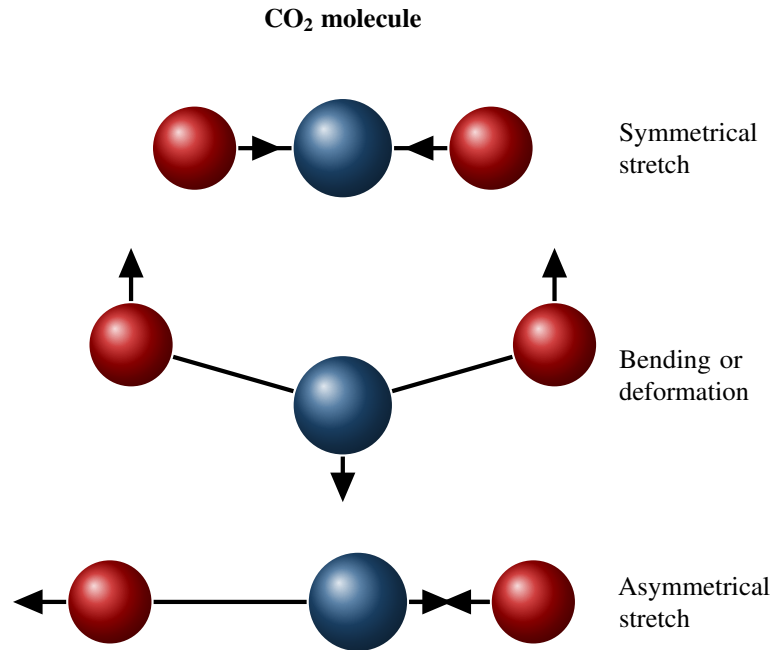


Figure 2.1: Three vibration modes of the CO₂ molecule.

Light can interact with matter in many ways, for instance in the form of scattering or absorption, and this also applies to molecules. When a laser beam impinges upon a molecule a coupling between the optical beam and the vibrational molecular modes occurs [24].

2.2.1 Classical theory of Raman scattering

The classical theory of Rayleigh and Raman scattering is unable to deal with all the aspects of these processes, but it does provide sufficient insights to explain the experiments of this thesis. The classical approach, in particular, will serve us to understand the frequency dependence, i.e., the Stokes and anti-Stokes terms, and some aspects of the selection rules.

2.2.1.1 First-order induced electric dipole

The goal is to obtain an expression for the frequency-dependent linear induced electric dipole P that will give rise to the Stokes and anti-Stokes frequencies

generated in spontaneous Raman scattering. We can start from the relationship

$$P = \boldsymbol{\alpha}E = \boldsymbol{\alpha}E_0 \cos(w_p t) \quad (2.5)$$

where E is the electric field vector of the monochromatic, electromagnetic plane wave with angular frequency w_p incident on a molecule, which we can also call the pump beam. The polarizability tensor $\boldsymbol{\alpha}$ of the molecule will generally be a function of the molecular vibrational frequencies. Here, we will consider a molecule that does not rotate but that is fixed in a certain position, and whose nuclei are free to vibrate about their equilibrium position.

The vibrations will lead to a change of the polarizability that can be expressed by expanding each component $\alpha_{\rho\sigma}$ of the tensor $\boldsymbol{\alpha}$ into a Taylor series with respect to the normal coordinates of vibration Q_k

$$\alpha_{\rho\sigma} = (\alpha_{\rho\sigma})_0 + \sum_k \left(\frac{\partial \alpha_{\rho\sigma}}{\partial Q_k} \right)_0 Q_k + \frac{1}{2} \sum_{k,l} \left(\frac{\partial^2 \alpha_{\rho\sigma}}{\partial Q_k \partial Q_l} \right)_0 Q_k Q_l + \dots \quad (2.6)$$

where $(\alpha_{\rho\sigma})_0$ is the polarizability value at equilibrium of the $\alpha_{\rho\sigma}$ component. The subscript '0' on the derivatives indicates that these are to be taken at the equilibrium configuration. Q_k is the k -th normal coordinate of vibration associated with the molecular vibrational frequency w_k . The first-order correction to the polarizability $\left(\frac{\partial \alpha_{\rho\sigma}}{\partial Q_k} \right)_0$ can thus be interpreted as the coupling between the electronic and nuclear coordinates. We will neglect the terms involving higher orders of Q_k , so for a normal mode of vibration we can write

$$(\alpha_{\rho\sigma})_k = (\alpha_{\rho\sigma})_0 + (\alpha'_{\rho\sigma})_k Q_k \quad (2.7)$$

where

$$(\alpha'_{\rho\sigma})_k = \left(\frac{\partial \alpha_{\rho\sigma}}{\partial Q_k} \right)_0 \quad (2.8)$$

We can define a new tensor $\boldsymbol{\alpha}'_k$, sometimes called the derived polarizability tensor because all of its components are derivatives of the polarizability with respect to the normal coordinate Q_k . Since Eq. 2.7 is satisfied for all tensor components, we can write

$$\boldsymbol{\alpha}_k = \boldsymbol{\alpha}_0 + \boldsymbol{\alpha}'_k Q_k \quad (2.9)$$

Now, let's consider the molecule is vibrating with a frequency w_k . Its nuclear displacement Q_k , assuming simple harmonic motion, will be given by

$$Q_k = Q_{k0} \cos(w_k t + \delta_k) \quad (2.10)$$

where Q_{k0} is the amplitude of the normal coordinate and δ_k a phase shift. Substituting this equation into Eq. 2.9 results in

$$\alpha_k = \alpha_0 + \alpha'_k Q_{k0} \cos(w_k t + \delta_k) \quad (2.11)$$

Combining equations 2.5 and 2.11 we obtain

$$\begin{aligned} P &= \alpha_0 E_0 \cos(w_p t) + \alpha'_k E_0 Q_{k0} \cos(w_p t) \cos(w_k t + \delta_k) \\ &= \alpha_0 E_0 \cos(w_p t) + \frac{1}{2} \alpha'_k E_0 Q_{k0} [\cos((w_p + w_k)t + \delta_k) + \\ &\quad \cos((w_p - w_k)t - \delta_k)] \end{aligned} \quad (2.12)$$

The first term represents Rayleigh scattering, i.e., at a frequency w_p , whereas the second and third terms represent the Raman scattering at the anti-Stokes $w_p + w_k$ and Stokes $w_p - w_k$ frequencies.

Figure 2.2 shows a typical Raman spectrum. The unique and characteristic spectral patterns are also known as Raman fingerprints. Here we employ reciprocal wavelength units (cm^{-1}), commonly used in spectroscopy when dealing with relative wavelengths as they are directly related to energy. In order to convert the normal wavelength values to a shift in the Raman spectrum, the following formula can be used:

$$\Delta\nu = \left(\frac{1}{\lambda_0} - \frac{1}{\lambda_1} \right) \quad (2.13)$$

where $\Delta\nu$ is the relative Raman shift expressed in cm^{-1} , λ_0 is the pump wavelength and λ_1 the Raman spectrum wavelength.

In this case, the whole spectrum is referenced to the laser wavelength. The scattered laser light or Rayleigh scattering will be in general more than a thousand times more intense, so it needs to be rejected with optical filters before the signal is sent to the spectrometer.

Raman microscopy allows visualizing the three dimensional chemical composition of biological specimens with high resolution in a noninvasive way, which is of high interest in the fields of biology, medicine and material sciences, among others. However, compared to the more widely spread fluorescence techniques, the signal involved is extremely weak due to the typically small Raman scattering cross-section.

Fluorescence and Raman scattering processes have associated cross-sections that can be used to compare their typical signal intensities. The Raman or fluorescence cross-section is the effective area that quantifies the likelihood of an

absorption or scattering event when an incident photon strikes the target molecule. A typical fluorescence cross-section is in the order of 10^{-18} cm²/sr, and a typical Raman scattering cross-section is in the order of 10^{-30} cm²/sr. A difference of ~ 12 orders of magnitude is clear evidence of the main drawback of spontaneous Raman microscopy. Moreover, Raman spectroscopy is affected by the presence of fluorophores since the fluorescence and Stokes bands can overlap.

Three main alternatives to the normally spontaneous Raman approach have emerged to enhance the signal power: Stimulated Raman Scattering (SRS) [25], Coherent Anti-Stokes Raman Spectroscopy (CARS) [26–28] and Surface-Enhanced Raman Spectroscopy (SERS) [29]. SRS and CARS boost the signal but require a more complex optical setup with an additional laser source. For a comparison between coherent and spontaneous Raman in terms of efficiency in a realistic measurement of biological samples we can look, for instance, in [30]. In that study, CARS spectroscopy was found to be at least two orders of magnitude more efficient than spectroscopy of spontaneous Raman scattering. Finally, SERS is a different approach where metallic layers or structures featuring plasmonic resonances enhance the Raman emission of molecules standing in their near-field. It has been used, for instance, in highly sensitive detection of very diluted molecules in gases or fluids [31], super-resolution microscopy of surfaces [32] and to study processes at the single-molecule level [33]. Intra-cellular sensing is also possible with nano-patterned metallic structures, as demonstrated in our group [34], but this is an invasive process and not suited for imaging within the cell. Its disadvantage is, therefore, that it can hardly be used for three-dimensional biological imaging, as the metallic structures would have to be scanned throughout the sample to obtain an image.

Infrared spectroscopy is another method sensitive to molecular vibrational modes that has been extensively explored. It provides a greater sensitivity and reliability compared to Raman at a fraction of the cost. The main downsides are the need of a more elaborated sample preparation, a lower resolution due to the longer wavelengths and the strong water absorption of the infrared light, rendering it incompatible with biological samples.

The appeal of Raman microscopy for chemical analysis of biological samples comes from its unique set of advantages. The Raman fingerprint of the sample can be acquired noninvasively with high spectral resolution and without extrinsic labels. Raman is the topic of research in many different areas such as medicine, pharmaceutical component discovery and material characterization. In the biomedical field, for instance, it has been used for glucose [35] and DNA detection [36], tumor diagnosis [37], to diagnose cancer [38,39], monitor blood glucose [40], differentiate cell lines [41] and sub-compartments [18], and many other applications.

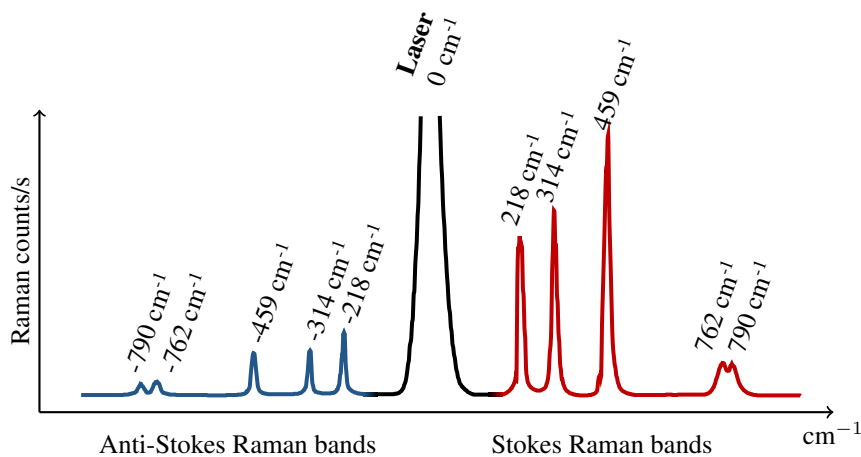


Figure 2.2: Typical Raman spectrum, or fingerprint, of carbon tetrachloride excited by a 488 nm laser [24].

2.2.1.2 Selection rules

From Eq. 2.12 we can now say that the necessary condition that a molecule has to satisfy to exhibit Rayleigh scattering is that α_o be non-zero. Since, to a greater or lesser extent, all the molecules are polarizable, all molecules will exhibit Rayleigh scattering.

In order to exhibit Raman scattering, a molecule vibrating with frequency w_k must have a non-zero value for α'_k . In turn, this requires that, for at least one component of the polarizability tensor, the gradient with respect to the normal coordinate at the equilibrium position cannot be zero. Although the selection rules appear to be straightforward, they become increasingly more complex as the number of nuclei in the molecule increases.

It is instructive to compare the condition that a molecule must satisfy to be Raman active with the condition to be infrared active. It will not be derived here, but the condition for infrared activity is that at least one of the components of the dipole moment vector (as opposed to the polarizability tensor) must have a non-zero gradient at the equilibrium position. Fig. 2.3 compares the polarizability and dipole moment variations in the neighbourhood of the equilibrium position of a three nuclei molecule, such as CO_2 .

The rule of mutual exclusion links the observation of molecular vibrations in the Raman and infrared spectra to molecular symmetries [42]. At this point we need to define what it means for a molecule to have a *center of symmetry*: for any

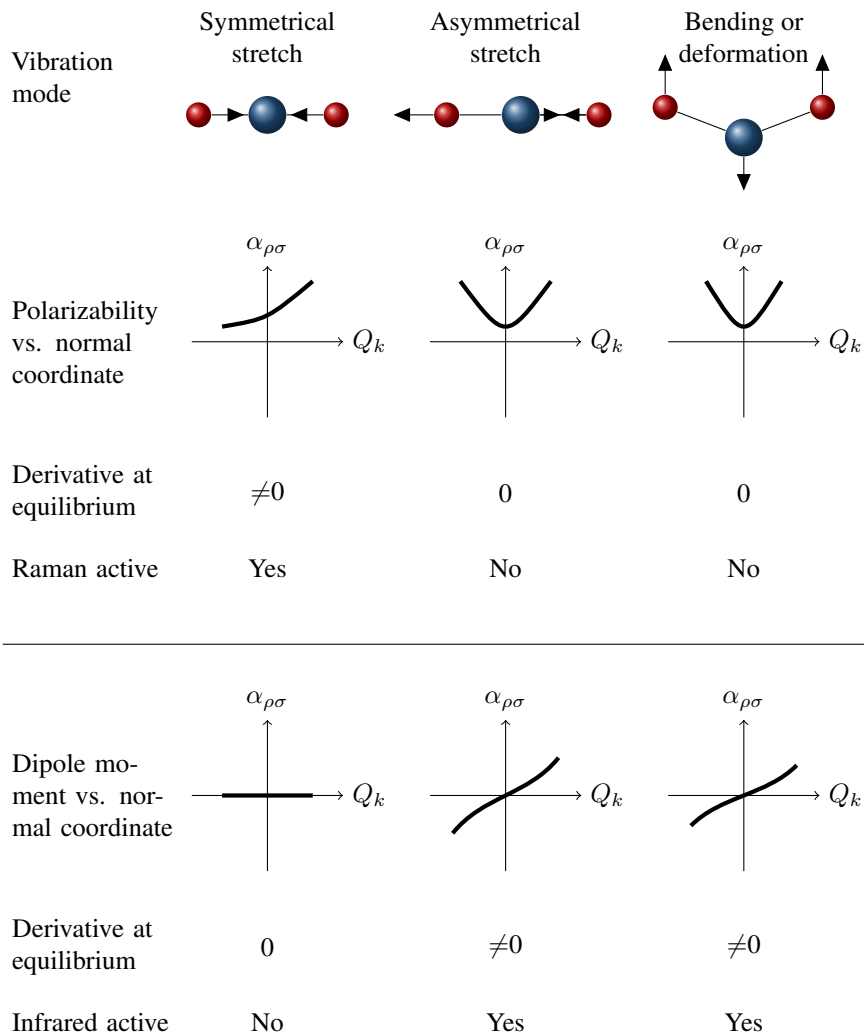


Figure 2.3: Raman and infrared activity of some vibrational modes of a molecule with three nuclei with a center of symmetry, such as CO_2 .

atom in the molecule, an identical atom exists diametrically opposite to this center point, and at an equal distance from it.

This rule states that, if a molecule has a center of symmetry, then a certain molecular vibrational mode can be either Raman active or infrared active, but not both simultaneously. Also, if a molecule has no center of symmetry, then it might have vibrational modes that are both, Raman and infrared active.

The converse of the rule is also true, i.e., if the Raman and infrared spectra of a molecule have no common lines, then the molecule has a center of symmetry. However, a mode of a particular symmetry can have no activity at all, neither Raman nor infrared.

2.3 4π Microscopy

In conventional diffraction-limited microscopy, due to the limited numerical aperture, the axial resolution (along the propagation direction) is around 3 to 7 times worse than in the transversal plane [2, 5, 6]. In order to obtain an isotropic and diffraction-limited resolution in every axis it is possible to effectively increase the number of excitation light beam angles by using more than one beam to excite the sample from opposite sides. In fact, the name 4π is derived from the maximal solid angle feasible for excitation and detection, although this ideal case can hardly be reached in practice. Single objective lenses can only reach aperture angles of up to 160 degrees, corresponding to $\approx 1.8\pi$ instead of 2π .

4π microscopy [43] is commonly used with fluorescent samples but it can also be used with scattering samples [44]. It is generally a scanning technique where two coherent beams interfere to increase the numerical aperture. This configuration results in a joint PSF with a central peak that is up to seven times narrower along in the axial direction than the peak obtained with a single-beam microscope [5, 6].

The working principle of 4π microscopy is depicted in Fig. 2.4 and compared to conventional confocal microscopy. In the latter, a single objective lens normally provides better transversal resolution (in the sample plane) than axial resolution (in the propagation direction). Conventional microscopy features a lateral resolution given by Eq. 2.3, different to the axial resolution in Eq. 2.4. Because the asymmetry of the focal spot is unfavorable for 3D imaging, 4π microscopy offers a solution by making the lateral resolution similar to its axial counterpart.

Depending on how the sample is illuminated and how the signal is collected, from one or both sides, a 4π arrangement can be categorized as one of the following three types:

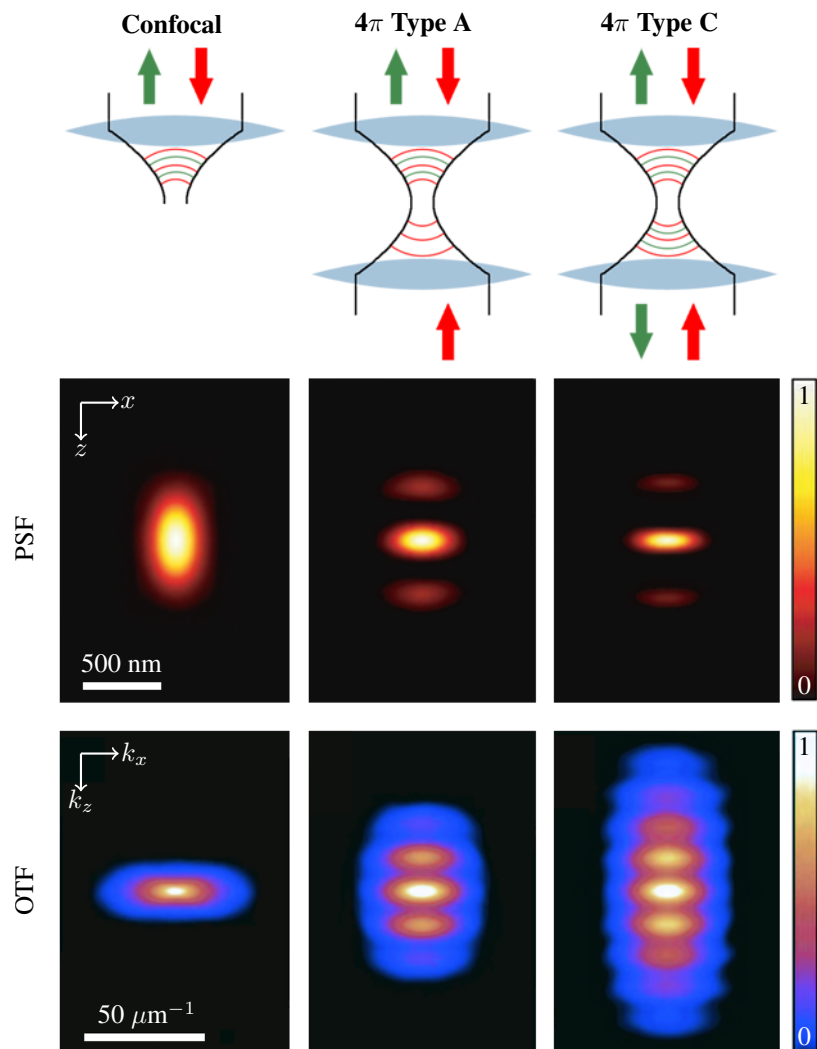


Figure 2.4: Comparison of the PSF and OTF of different two-photon excitation approaches: standard single-lens confocal microscopy, and Type A and C 4π microscopy. Adapted from [45]. Two-photon excitation is, apart from using high aperture lenses and strict confocal conditions, a common way to weaken the secondary lobes of the 4π PSF. The 4π microscope (water-immersion, lens 1.20 NA, λ excitation = 870 nm, λ detection = 510 nm, pinhole diameter of 1 Airy disk) has an improved axial FWHM compared to standard confocal microscopy (λ excitation = 488 nm, λ detection = 510 nm, pinhole diameter of 1 Airy disk). 4π Type C exhibits lower sidelobes and $\sim 30\%$ increased axial resolution compared to Type A. The larger OTF support of 4π is proof of the higher resolution compared to the confocal OTF.

- **Type A:** The illumination is split into two beams that interfere coherently at the sample.
- **Type B:** The signal coming from the sample is collected from both sides and interferes coherently at the detector.
- **Type C:** Both the illuminating and the detecting waves interfere coherently, at the sample and at the detector, respectively. This configuration yields the best resolution as both, illumination and detection, have a 4π point spread function. Type C obtains around 30% better axial resolution than its Type A and B counterparts.

Reference [2] details the PSF differences between different types of arrangements, and the differences with respect to a conventional confocal PSF.

The Optical Transfer Function (OTF) is an important tool to evaluate the performance of optical systems. It describes the optical systems in terms of the spatial frequencies that it can capture, and for a linear system, the OTF is given by the Fourier transform of the intensity PSF. Figure 2.4 compares between the OTF of a standard single-lens confocal microscope with 4π type A and C. The larger OTF support of 4π is proof of the higher resolution as compared to the confocal OTF.

A demonstration of 4π microscopy for live cell imaging [46] and even their subcomponents [47, 48] has already been accomplished. A broader application, however, has been hindered by the need to precisely align both objective lenses, the scattering in the medium and by the aberrations [49]. Imaging small field of views and thin samples helps mitigate these issues. It is possible though to use *optical phase conjugation* for automatically aligning both objective lenses and correcting the aberrations and scattering in the medium, as demonstrated in [50]. The drawback is that it needs a spatial light modulator and additional optics to measure the distortions of the beams going through the sample. Even in a system without environmental phase fluctuations, the distortions have to be re-measured frequently when probing different parts of heterogeneous samples.

To boost the imaging acquisition speed, typically slow due to the need to scan point-by-point the sample in a confocal microscope, it is possible to parallelize the scanning process by using many 4π foci simultaneously in an approach called *multi-focal multi-photon microscope* [48].

Since using two beams has proven to enhance the axial resolution so much with respect to the single-beam case, one might wonder if additional lenses or beams could further improve it. Remarkably, the axial resolution achieved by 4π microscopy is the best among multi-beam techniques. Additional beams can only slightly improve the transversal resolution of high NA objectives, however, they can

have a greater impact on the effective illuminated volume. A realistic setup with three beams already gets very close to the ideal smallest volume, which is about half of the 4π case [51].

There are also many alterations of the 4π arrangement in the literature. In [52], for instance, the authors propose a setup where, by using a mirror, a 4π PSF is obtained with a single microscope objective. In [53] it is shown that even when the interference between counter-propagating beams in 4π microscopy is destructive, as opposed to constructive, a linear deconvolution leads to almost identical images.

In the following sections we will discuss the potential signal enhancement provided by 4π microscopy, the challenge of keeping the PSF invariant even when the surrounding medium is not, and how to remove the secondary lobes of the PSF. Finally, we will discuss the commercial system available in the market and the state of the art.

2.3.1 Signal Enhancement

An advantage of 4π microscopy is that it excites a smaller volume but collects a larger part of the isotropic spontaneous Raman signal. A single-objective microscope, in the best case, can collect half of the Raman signal, whereas two objective lenses can potentially collect the whole signal. Since we can simultaneously excite a smaller volume and collect more light from it we expect to get an improvement factor of roughly 4-fold in the signal-to-noise ratio compared with conventional confocal microscopy.

2.3.2 The phase problem

An often overlooked challenge in multi-beam microscopy is that the phase between beams has to be controlled and stable. However, the presence of the sample itself can modify the phase relationship between beams and consequently perturb the fringe pattern. Therefore, it is important to measure the phase shift between beams at the sample plane directly, so that it can be set and maintained to the desired value within different sample regions and different samples. Further ahead in Chapter 6 we will describe a method to do so by using the sample substrate interface as the phase reference, making the system insensitive to sample-induced phase shifts.

In order to avoid image distortions, the PSF must remain invariant as the sample is translated in any direction. It must be independent of the sample position even though the refractive index variation within the specimen can greatly influence the phase difference between the interfering wavefronts. Then, how are the beams

normally set to constructive interference?

Perhaps the most straightforward way is to use planar or point-like features within the sample [54, 55]. Small structures give an estimate of the spatial variance of the PSF because their intensity depends on the relative phase between wavefronts.

Similarly, in [45] a cell is sandwiched between two fluorescent layers. Since the layers are perpendicular to the z -axis the main and secondary lobes can be probed. The phase induced by the sample can be tracked and set to the maximum using this method. In general, for small displacements in x or y the phase induced by the sample remains constant. The only phase adjustment necessary is the dependence with the axial sample position due to the difference between the sample refractive index and the surrounding immersion medium, which can be assumed to be linear [56].

Typically the phase shift between pump beams has to be set to constructive interference before the measurement, but in [57] the authors came up with an alternative. From only one measurement with an unknown phase between beams, the authors are able to recover the relative phase between opposing beams. They can do so at the expense of applying a quite complex parametric blind deconvolution algorithm. For now, the method only works for relatively homogeneous samples for which the PSF is independent of the sample position.

In the critical frequency method [58] a crosssectional image (in the xz or yz plane) of the sample is taken at a few different nominal phases. For destructive interference, the 4π PSF has two main lobes separated by approximately $\lambda/2n$. Meaning that objects separated by that distance will not be distinguished. In the spatial frequency domain the corresponding spatial frequency, $k_c = 2\pi n/\lambda$, will be attenuated. The critical frequency method exploits this to retrieve the nominal phase and thus allowing setting it to any desired value.

2.3.3 Secondary lobes

In practical systems the sample cannot be illuminated from every angle since each objective lens has a limited angular aperture. This means that the point spread function exhibits strong secondary lobes in the axial direction, as can be seen in Fig. 2.4. Secondary lobes, or sidelobes, produce artifacts on the images, so they have to be mitigated as much as possible from a hardware and/or processing perspective.

A thorough analysis [59] concluded that sidelobes with an intensity up to 50% of the main lobe can be removed by image processing, but in practice weaker sidelobes are desirable due to the finite signal-to-noise ratio.

As we will see in later chapters, especially in Fig. 5.2, one of the main problems of our setup is precisely this, the strong secondary lobes of the PSF. We can get insights from 4π fluorescence studies on how to remove the secondary lobes:

- **Confocal detection:** There are examples of 4π microscopy being used as a wide-field approach, for instance in [60]. However, the fluorescence signal emitted from out-of-focus planes is attenuated more efficiently with a confocal detection scheme [61–63], and therefore, used in the majority of 4π studies. The drawback of confocal microscopy is that it is typically a point-by-point scanning technique, requiring much longer times to obtain images of the same areas as its wide-field counter-part.
- **Type C:** 4π Type C combines the excitation and detection interference patterns. The longer wavelength of the pump produces a PSF with secondary lobes further from the center than the detection PSF. It is this disparity that reduces the final contribution of the secondary lobes after the PSFs are combined.
- **Two-photon excitation:** It is possible to use high pump powers to use a process called two-photon absorption. In this process two photons, with twice the wavelength of single-photon fluorescence, excite the fluorescence of the sample [64–66]. The excitation efficiency of the illumination follows a quadratic dependence, so only the central part of the main lobe would have enough intensity to excite this process. Moreover, the disparity between excitation and detection PSFs is much stronger than in Type C 4π . As a result, the secondary lobes with two-photon excitation can be theoretically as low as 8-14%, but around 40% of the main lobe in practice [65].

The main challenge for an analog process in Raman microscopy, known as hyper-Raman scattering, would be the enormous amount of pump power needed and the lower efficiency of this process [24,67]. It would only worsen the already weak Raman signal problem. Burning the sample, even if they are weakly absorbing, would be another concern at the high pump intensities required to excite this process.

Stimulated Raman Scattering (SRS) and Coherent Anti-Stokes Raman Scattering (CARS) are also multi-photon processes that can reduce the secondary lobes. These are treated more in detail in Chapter 7 as a possible path to improve our optical setup.

- **Deconvolution:** Mathematical deconvolution can decrease the contribution of these secondary lobes. It can do so provided that a high signal-to-noise ratio and that the point spread function of the microscope is well characterized and invariant when the sample is translated in any direction.

There are two main types of deconvolution algorithms, nonlinear and linear. Nonlinear algorithms remove the secondary lobes more effectively and can even reduce the noise in the image. The downside is that they are computationally expensive, susceptible to poor PSF measurements and subject to problems related to stability and convergence. Moreover, the result depends on the sample itself; thinner and more sparse objects converge faster and better. On the other hand, linear algorithms perform slightly worse but tend to be simpler and faster. They have proven to be sufficient for restoring 4π images of biological samples [68].

There is a variation of the 4π technique [69] that deserves a separated mention because the authors use a third objective lens, placed orthogonally to the other two. Since this extra lens is used to collect the fluorescent light from the side, it is theoretically capable of reducing the secondary lobes. At the same time, it could be used to solve the phase problem because the intensity collected from the side depends on the phase between 4π pump beams.

The removal of secondary lobes is challenging in a variety of optical microscopy techniques, not just in 4π microscopy. As an example, in a light-sheet microscopy study [70] the authors use an asymmetric PSF claiming it is the key factor to completely eliminate the secondary lobes after a simple deconvolution.

2.3.4 Commercial availability

The Leica TCS 4PI system in Fig. 2.5 was developed in close cooperation with Stefan W. Hell and was released in 2004 as a limited special edition for institutions with the appropriate technical and environmental conditions to employ it. This first commercial 4π microscope is built from a confocal microscope stand (Leica TCS SP2) that provides the scanning and detection capabilities, and to which a 4π unit is attached.

An intense pump beam from a Ti:sapphire laser provides the sufficient power for two-photon excitation fluorescence in a Type C arrangement. Dispersion compensation and independent optical path matching for both arms is crucial in this configuration. For that, dispersion compensation optical wedges are employed in the bottom arm. The mean optical length of that path is pre-compensated in the top arm with a glass window. A compact symmetrical design and the mechanical enclosure ensure a good isolation against thermal fluctuations.

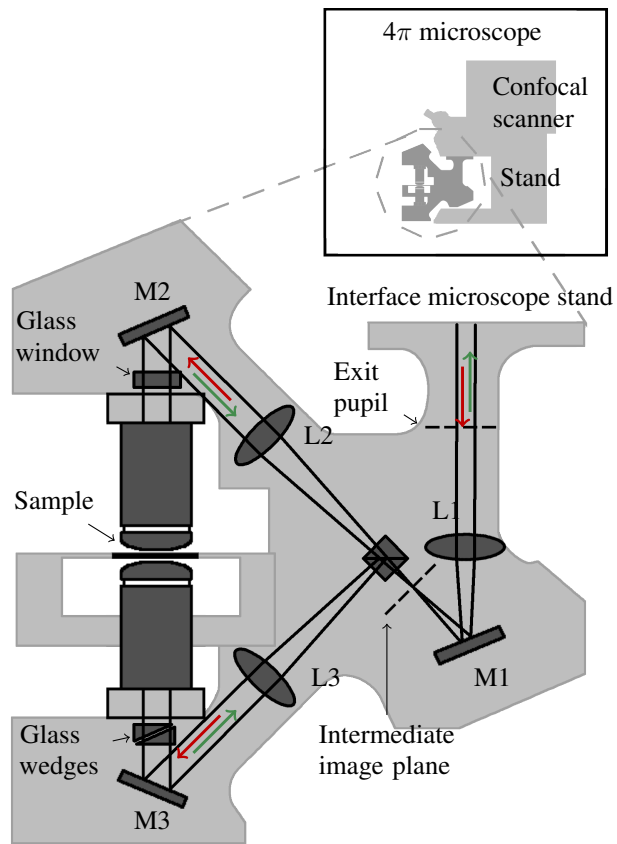


Figure 2.5: Schematic of the commercial 4π microscope Leica TCS 4PI. Adapted from [5].

2.3.5 State of the art

In conventional 4π microscopy, the best resolution with the lowest contribution from the sidelobes are attained with Type C two-photon 4π microscopy with data deconvolution [5], where a combination of the previous mechanisms to reduce the secondary lobes is exploited. Related studies have reported resolutions of ~ 100 nm [7, 8] and even smaller than 80 nm [5, 71], where the axial resolution corresponds to about one fifth of the wavelength and surpasses the lateral resolution by 25%. To achieve such small resolutions, super-resolution techniques have to be employed, and they are one of the main topics of Chapter 4.

However, the most recent, complete and remarkable study at the time of writing this dissertation was published in 2016, led by Joerg Bewersdorf [60], a Professor at Yale University and former student of Stefan W. Hell, and co-authored by Nobel laureate James E. Rothman, among others. The authors built upon more than a decade's work to develop a super-resolution fluorescence 4π Type B microscope that is unconventional in several ways: it is wide-field, the sidelobes do not need to be removed as in any previously described approaches, and they actively correct for optical aberrations and drifts of the stages.

The few secondary lobes present on the PSF introduce ambiguities in the z -position of the fluorescent molecules detected. Similarly to the previously mentioned study [70] where an asymmetric PSF enables the complete removal of the secondary lobes, here the ambiguity is removed by introducing astigmatism in the system [72, 73]. The eccentricity or asymmetry of the PSF caused by astigmatism can be used to axially localize the molecules with enough precision to narrow the position down to individual peaks, thus achieving artifact-free 3D localization.

A known limitation of super-resolution techniques is that they cannot measure deep inside biological samples due to aberrations induced by the sample. In this work, to correct for any sample-induced and system aberrations, they employ two deformable mirrors, one on each arm of the collection path, which allows them to measure quite deep into biological samples. Regarding the drift of the stages, an additional alignment laser in the near-infrared that does not interfere with the fluorescence is used to actively track and correct them.

Four images at different phase shifts were still necessary to achieve all of these features. They split the fluorescence signals of both arms into their two orthogonal polarizations in such a way that four images are taken simultaneously on different parts of the same camera sensor, each for a different phase shift.

Several 3D images with a resolution in the 10 nm range demonstrate the capabilities of the technique —called whole-cell 4Pi single-molecule switching nanoscopy.

These images include different biological samples: networks of endoplasmic reticulum, cellular microtubules, mitochondrial networks and more.

Additionally, as we will further discuss in Chapter 4, the combination of 4π microscopy with other super-resolution fluorescence techniques has yielded the highest resolution in fluorescence microscopy to date.

2.4 Conclusion

Raman circumvents the need for extrinsic labels of fluorescence microscopy, which makes it very appealing for many applications, a major one being the 3D visualization of living biological samples. Additionally, it detects the chemical fingerprint and structure of the sample, something not feasible with fluorescence. The main hurdle is that the signal emitted is intrinsically weak due to the small scattering cross-section of molecules, making the collection of a significant amount of it quite challenging.

We have seen that not every vibrational molecular mode is Raman active. Basically, the selection rules state that Raman scattering arises from a changing molecular polarizability. Thus, a vibrational mode is Raman active if the polarizability in the molecule is changed while it vibrates.

Besides potentially increasing the Raman signal collected, the proposed 4π Raman microscopy technique provides the best axial resolution possible. Historically, the control of the phase between beams or overlap between the PSF fringes and the sample has been challenging. We have seen how using thin sample features can be used to probe the PSF within the sample itself. The axially thin features can therefore be helpful to set the appropriate phase shift between beams and make the PSF independent of the sample position. As an alternative, the critical frequency method links spatial frequencies of the data with the phase shift between beams, so it can also be used to solve the known phase problem in 4π microscopy.

We have discussed how the characteristic secondary lobes can hinder the effective resolution obtained. By looking at 4π fluorescence studies we have seen how the secondary lobes can be reduced as much as possible through optical means as well as by deconvolving the data with the PSF of the microscope.

3

Implementation of the Microscope Setup

This chapter describes the 4π Raman optical setup we designed during this dissertation. Two key elements set it apart from the state of the art: an isolator in the interferometer and the use of a partial reflection from the sample itself to stabilize the phase between counter-propagating pump beams.

| | | |
|------------|---|-------------|
| 3.1 | Introduction | 3-2 |
| 3.2 | Mach-Zehnder vs. Michelson Interferometry | 3-4 |
| 3.3 | Description of the 4π Raman Optical Setup | 3-6 |
| 3.3.1 | Isolator | 3-8 |
| 3.3.2 | Partial reflector | 3-10 |
| 3.4 | Stabilization and phase control | 3-11 |
| 3.4.1 | Phase linearization | 3-11 |
| 3.4.2 | Stabilization in the 4π Raman microscope | 3-17 |
| 3.5 | Conclusion | 3-22 |

3.1 Introduction

Initially, we wanted to build a robust and thermally isolated 4π Raman microscope as the commercial Leica TCS 4PI discussed in Chapter 2 by enclosing the entire setup within the same microscope turret in a compact way. However, we started building the experimental setup from an existing conventional Raman microscope from WITec shown in Fig. 3.1, and it was unfeasible to modify it to resemble the Leica system. Instead, we had to upgrade it to a 4π Raman microscope by externally adding new functionalities.

In order to connect the Raman pump, the WITec system has an optical fiber access on the top and bottom parts that we could readily use. In that regard, the component that we needed to upgrade the microscope was clear: an external interferometer that would split the laser beam into two and cope with their relative phase. These two beams would be connected to the fiber ports of the WITec system. It is well known that fibers are very sensitive to thermal fluctuations, however, in a 4π microscope it is of utmost importance to have a stable and controllable interference between pump beams at the sample plane. But, how can we stabilize the phase shift between counter-propagating beams when it is not directly accessible at the sample plane?

We came up with an innovative interferometer configuration that offers a solution to the known challenge in 4π microscopy regarding the control of the phase between pump beams at the sample plane. The phase between beams, or nominal phase, is not automatically matched, a concern that does not apply to conventional microscopes with a single objective lens. In a 4π scheme, depending on the sample thickness, refractive index and the substrate, the optical path length recovered by the beams can differ greatly when different parts of the sample are measured.

We realized that stabilizing the phase at the sample plane in a noisy environment requires to measure the phase exactly there. No interferometer is able to decouple the phase variations from the phase shift induced by the sample, so we have to measure the phase where we want to stabilize it. Although there is no simple way to place a detector at the sample plane directly, we came up with an alternative solution: a partial reflection from the sample itself can give us indirect access to the phase shift between beams at the sample plane.

Being sensitive to the phase shift at the sample plane enables us to set and keep it constant, regardless of the sample position. This precise control, absent in conventional non-stabilized 4π microscopes, widens the sample area that can be measured with a translationally invariant PSF and allows us to obtain the phase shift induced by the sample. The procedure to obtain the quantitative phase shift induced by the sample will be explained later in Chapter 6.

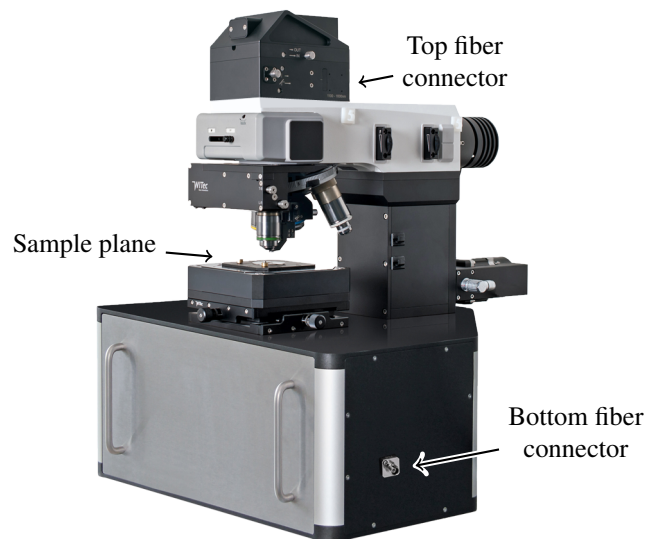


Figure 3.1: Witec Alpha 300 Raman microscope modified to add bottom access to the sample. This was the optical setup available at the start of this dissertation. To build a complete 4π microscope, we later added a tailored interferometer connected to this microscope stand through the top and bottom fiber connectors.

This chapter discusses different kinds of interferometers that we could use to control the phase shift between beams and the interferometer that we actually built. Then, it discusses the solutions given in the literature to first, measure the phase in an unambiguous manner, and second, to compensate for all the temporal fluctuations in order to keep it stable during the measurements.

3.2 Mach-Zehnder vs. Michelson Interferometry

The noisy nature of our optical setup forced us to develop an interferometer that would give us access to the phase shift between pump beams at the sample plane and stabilize it. Due to its straightforward and simple implementation we first considered a Mach-Zehnder type interferometer, as shown in Fig. 3.2. This is a broadly used configuration in microscopy where the laser light is split into two paths: the sample and the reference arms. The sample beam is perturbed by the sample and then recombined with the reference beam. The resulting interference pattern measured by the photodetector depends upon the phase shift between arms. So if the reference arm introduces a known phase shift, then the phase shift introduced by the sample arm can be extracted and quantified.

However, here we are not interested in the phase shift introduced by the sample. We are now interested in the phase variations induced by the fibers, but this interferometer is blind to which part of the sample arm introduces the variations. Looking at Fig. 3.2, this interferometer is sensitive to the phase difference between entire arms $\phi_r - (\phi_{s1} + \phi_{s2})$, while we are interested in the signal $\phi_{s2} - \phi_{s1}$. We soon realized that a Mach-Zehnder interferometer is therefore inappropriate for our needs.

A different kind of interferometer —so called Michelson interferometer— is based on reflections from two mirrors. Figure 3.3 shows a version of a Michelson interferometer that gets a step closer to the actual interferometer in our laboratory. As it uses the reflections from the sample, the detector in this case is sensitive to twice the phase difference between both sample inputs, $2(\phi_b - \phi_t)$.

Michelson interferometry is specially suited for non-transmissive samples. Should both beams be transmitted, nothing would be detected in the Michelson interferometer since they would both suffer the same phase delay $\phi_t + \phi_b$. They would have an arbitrary phase shift at the sample plane but they would always interfere destructively at the detector, regardless of the phase variations. If we, however, consider only the reflections, as indicated in the drawing, we would have exactly what we need. The issue is that to generate the 4π fringes inside the sample it obviously needs to be quite transparent.

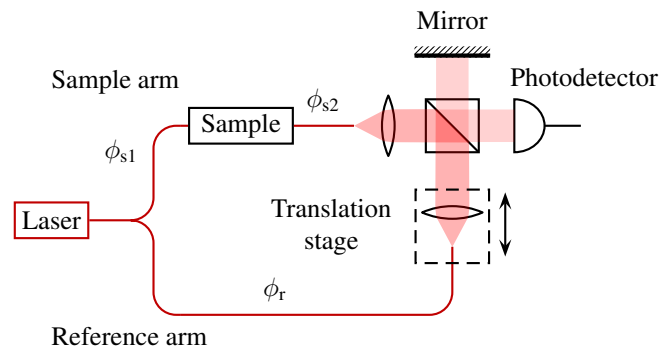


Figure 3.2: Mach-Zehnder interferometer sensitive to $\phi_r - \phi_s$, where $\phi_s = (\phi_{s1} + \phi_{s2})$. The beamsplitter would normally be rotated 90 degrees with respect to the drawing, but we need this configuration to excite the sample from both sides in a 4π illumination.

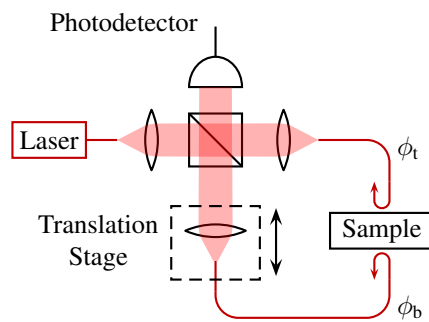


Figure 3.3: Michelson interferometer that uses sample reflections and thus is sensitive to $2\phi_b - 2\phi_t$

We are interested in the phase between beams at the sample plane, which we can only read and control if we have information from that plane. Only the reflections from the sample itself can provide such information. Therefore, as we will see in the following sections, we actually work with yet a different version of a Michelson interferometer. We work with one transmission and one reflection, which allows us to probe the phase shift at the sample plane and at the same time to work with transmissive biological samples.

3.3 Description of the 4π Raman Optical Setup

Commercial 4π microscope systems are based on enclosed free space optics, rendering them inherently robust against environmental factors such as temperature changes or air currents. In contrast, we employ a system with a fiber access to the top and bottom objective lenses. Fibers are known to be sensitive to environmental fluctuations [74], leading to phase variations in the system. A fluctuating phase shift between pump beams is detrimental for 4π Raman microscopy and therefore we need to reduce it as much as possible. An interferometer not only allows us to decrease the phase variations in the system, but also to control the phase shift between beams.

Based on the Michelson interferometer discussed above, we developed the interferometer sketched in Fig. 3.4. It was tailored to measure and control the relative phase between both pump beams at the sample plane. Additionally, it can compensate for the phase fluctuations in the system introduced by the fibers, which needs to be compensated as the associated fluctuations are faster than the measurement acquisition time.

Figure 3.4 shows the optical scheme of the quantitative phase and Raman microscope. The phase signal is collected by a photodetector (Thorlabs SM1PD1A) in one of the arms of the interferometer. The beam from a single-mode 785 nm laser diode (Toptica XTRA II) is split into two paths. One path is connected to the top part of a Raman microscope (WITec alpha300 upgraded to add inverted access), and the other to the bottom thereof. The total laser power measured after the coupling into a monomode polarization maintaining fiber is 260 mW.

The polarization of both arms of the interferometer must be the same to achieve coherent interference at the sample plane. The laser output is linearly polarized, and it is kept so by using polarization maintaining fibers. If necessary, a half wave plate present in the top part of the WITec system rotates the linear polarization of the top beam in order to match the polarization of the bottom beam.

Different objective lenses were used in the top side of the microscope, depending on whether a dry (Zeiss, EC "Epiplan-Neofluar" DIC M27 100x/ 0.9NA) or a water immersed sample (Zeiss, Water immersion Plan-Apochromat M27 63x/ 1.0NA) is being measured. The objective at the bottom (Nikon, Plan Fluor DIC 20x/ 0.5NA) side of the microscope is kept always the same. Ideally the same high NA objectives would be used on both sides to get the smallest PSF possible. Here we use a lower NA on the bottom side for two main practical reasons. First, a lower NA yields a larger focal volume and therefore it maintains a better alignment with the top objective when subjected to thermal drifts of the stages. Second, its long working distance of 2.1 mm is needed to go through relatively thick substrates. The substrates that we will be using in the experiments are up to 1 mm thick. The optical powers reaching the back-aperture of the top and bottom objectives are 35 and 58 mW, respectively. The asymmetry between arms is due to the 2.2 dB losses of the isolator in the interferometer, and it is partially compensated by the different confocal volumes of the objectives.

The fill factor of the objective's back-aperture or exit pupil is important as it determines the effective NA and will define the point spread function of the instrument. However, to be able to give an estimation of the fill factor for the three objective lenses used during this thesis we first need to determine the diameter of the laser beam hitting the pupil of the objectives and the different pupil diameters. The full width at half maximum of the laser beam was measured to be 3 mm. We can calculate the exit pupil diameter of each objective lens P with the following formula:

$$P = 2 \cdot \text{NA} \cdot f_{obj} \quad (3.1)$$

where NA and f_{obj} are the numerical aperture and the focal distance of the objective, respectively. The focal distance of the objective lenses are not normally given in their specifications, but it can be calculated from their magnification M and the focal distance of the standard tube lens f_{tl} used by the objective manufacturer with the formula:

$$M = \frac{f_{tl}}{f_{obj}} \quad (3.2)$$

Zeiss employs a tube lens of $f_{tl} = 160$ mm, and Nikon $f_{tl} = 200$ mm. With these data we can finally give an estimation of the pupil filling factor for the three objectives. The objective lenses used in the top part of the microscope, the Zeiss 100x/0.9NA and the Zeiss 63x/1.0NA, have an exit pupil filling factor of 100% and 59%, respectively. The Nikon 20x/0.5NA used in the bottom part has a filling factor

of 30%. As previously explained, the low filling factor of this low NA objective is not considered relevant since we rather prioritize robustness against drifts and the long working distance.

The Raman signal, collected by a 100 μm core-diameter multimode fiber, is measured by a spectrometer (UHTS 300 with a -70 $^{\circ}\text{C}$ cooled CCD camera, ANDOR iDus 401 BR-DD and a grating with 300 grooves/mm). This fiber acts as the pinhole in the collection part of the confocal microscope. The diameter of this fiber core is too large for an optimal axial and transversal resolution. It was selected to sacrifice resolution in favor of a larger Raman signal. Considering the 0.9NA objective with a 100x magnification and an transversal resolution of 0.5 μm , the optimal pinhole diameter would be 50 μm . The fiber core is, thus, twice as big as the optimal pinhole diameter. For the 63x/1.0NA objective, the diameter of the fiber core is around four times larger than the optimal size.

3.3.1 Isolator

There are four beams travelling throughout the interferometer, two transmitted and two reflected beams from the partial reflector. The isolator (Thorlabs IOT-5-780-VLP, 55 dB isolation) in the top arm blocks two of them resulting in a two-beam interferogram. The photodetector is sensitive to the $\cos \phi$ term generated by the interference between the remaining two beams (red solid arrows). The transmitted beam through the sample and a partial reflection from the bottom beam, both indicated by red arrows, undergo a phase shift ϕ_T and ϕ_R , respectively. Considering the complete optical path travelled by these two beams we obtain ϕ :

$$\begin{aligned}\phi &= \phi_{\text{Reflected}} - \phi_{\text{Transmitted}} \\ &= (2\phi_R) - (\phi_T + \phi_R) \\ &= \phi_R - \phi_T\end{aligned}\tag{3.3}$$

The transmitted and reflected beams co-propagate along the bottom fiber and therefore they will suffer the same phase shift in the last part of their path towards the detector. This way the phase difference at the sample plane can be retrieved with the detector being at a completely different plane.

The sample introduces an additional optical length ϕ_{sample} and the phase shifter introduces ϕ_f , both contributing to the photodetector signal V :

$$V = O_f + A \cos(\phi_T + \phi_{\text{sample}} - \phi_R - \phi_f)\tag{3.4}$$

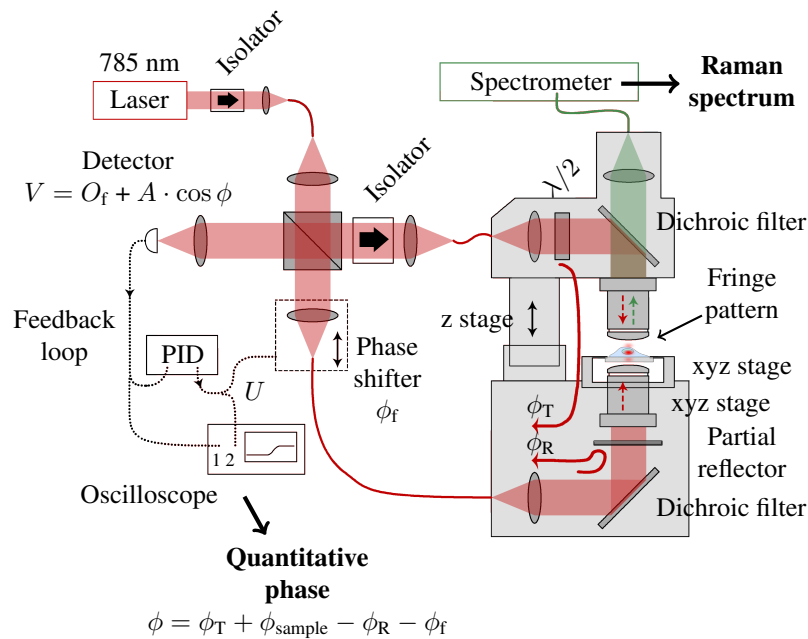


Figure 3.4: Schematic of the Raman and quantitative phase microscope. The optical path length of the top and bottom arms to the partial reflector is indicated as ϕ_T and ϕ_R , respectively. The red solid arrows indicate the beams that will interfere at the detector to produce the signal $V = O_f + A \cos \phi$, where $\phi = \phi_T + \phi_{\text{sample}} - \phi_R - \phi_f$. This signal depends on the phase shift between top ϕ_T and bottom ϕ_B pump beams, including the influence of the sample ϕ_{sample} and phase shifter ϕ_f . The Raman spectra are obtained by the spectrometer and the quantitative phase by the detector connected to a feedback loop. The partial reflector is a key component for the stabilization of the phase shift between beams at the sample plane.

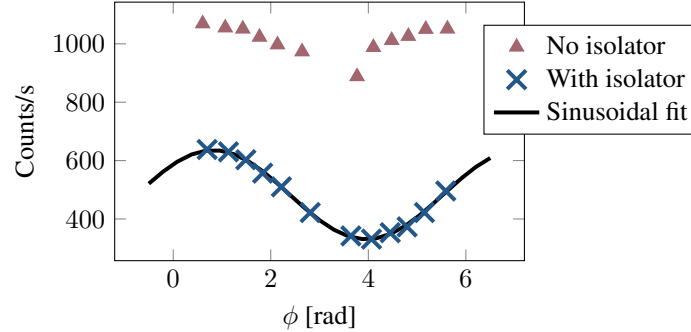


Figure 3.5: Measurement of the the TiO_2 peak at 154 cm^{-1} , with and without isolator. Only when the isolator blocks unwanted contributions in the interferogram can we model it with a simple sinusoidal model. By fitting the curve with the model we obtain the phase shift between pump beams.

where the constant O_f is what we call the offset of the interferogram, and A the amplitude of the cosine.

Figure 3.5 shows the recorded interferogram with and without the isolator when measuring a 50 nm layer of TiO_2 on top of a CaF_2 substrate. The phase between pump beams ϕ was stabilized at different values by following the procedure explained later in Section 3.4.2.

As the sample did not have to be immersed in water, we could use the Zeiss 100x/0.9NA objective lens on the top part of the microscope. More than two interfering beams make the interferogram more difficult to interpret. Depending on the relative amplitudes of the beams the interferogram can be more complex than a sinusoidal curve and thus difficult to fit. On the other hand, two beams always generate a sinusoidal curve with a known periodicity, with the only parameters being the amplitude and, more importantly, the phase.

3.3.2 Partial reflector

Typically, samples consisting of nanolayers on top of a substrate exhibit a strong reflection, so we will not need the partial reflector. The partial reflector is only necessary when the sample's reflection is weak as in the case of biological experiments. The reflection of this kind of samples happens at the interface between the substrate and the biological medium, and it can be reduced for several reasons. When the sample is immersed in water the index contrast between substrate and sample is reduced so much that the reflection cannot be processed. Also, when measuring far above or below the substrate-sample interface, the confocal nature

of the microscope will block most of the reflection. The partial reflector used is a glass microscopy slide of 1 mm thick, with a measured reflection coefficient of 8%.

It is important to note that any phase fluctuation happening between the partial reflector and the sample cannot be compensated. The assumption is that the partial reflector is so close to the sample that any phase fluctuation between them is negligible.

3.4 Stabilization and phase control

Stabilization of optical setups encompasses many different topics. Phase or frequency stabilization are terms often used interchangeably in diverse applications such as laser linewidth stabilization, hologram recording in crystals or digital holography. Here we do not intend to provide a comprehensive review of this broad topic, we focus on the studies that motivated our own implementation of a stabilized setup or that could be used in a similar one. From now on, we will call *nominal phase* the desired phase setting at which the interferometer is to be locked by the PID. It defines the relative position or overlap between the fringes and the sample.

3.4.1 Phase linearization

A detector placed at the output of a conventional interferometer like in Fig. 3.2 measures the following intensity:

$$I = O_f + A \cos \phi \quad (3.5)$$

where O_f and A are called offset and amplitude, respectively.

The intensity measurement does not provide direct access to the phase ϕ due to the nonlinear $\cos \phi$ function. Therefore, more than a single ϕ value can satisfy the equation. Linearizing the phase measurement means to get direct access to the phase variable, at least up to a constant coefficient, and not just to the cosine of the phase. The main consequence of the linearization process is the removal of ambiguities, which will be of importance to compare our stabilization with other techniques. More specifically, to reflect the ambiguities the equation should be written as:

$$I \propto \cos(\phi - N\pi) \quad (3.6)$$

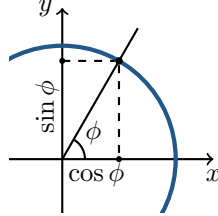


Figure 3.6: Origin of the unambiguous phase obtained from a single interferometric measurement. The interference is sensitive to $\cos \phi$, so the orthogonal component $\sin \phi$ is missing.

where N is any integer number.

Here we will not concern ourselves with the case where N is an even number $\dots - 4, -2, 0, 2, 4\dots$ as this ambiguity is typically only removed by dedicated algorithms, better known as unwrapping algorithms [75]. However, it is possible to remove the ambiguity where N is an odd number $\dots - 3, -1, 1, 3\dots$ by taking another measurement with an additional phase shift in one of the arms. In Fig. 3.2 the additional phase shift can be introduced by the phase shifter. In order to obtain the unambiguous phase value it is clear from Fig. 3.6 that the orthogonal component $\sin \phi$ is needed, or equivalently $\cos(\phi + 3\pi/2)$. More generally, a second measurement with an additional and known phase shift allows determining the orthogonal component needed. The additional phase shift does not need to be $3\pi/2$, it can be any value with the exception of π multiples since that would not provide any information about the orthogonal component, $\cos(\phi + N\pi) = \pm \cos \phi$.

Therefore, in the most general case we need four equations to completely resolve the interference pattern, two for the offset O_f and amplitude A , and two more for the unambiguous angle ϕ . Typically, the measurements are taken in $\pi/2$ regular phase steps:

$$\begin{aligned}
 I_1 &= O_f + A \cos(\phi) \\
 I_2 &= O_f + A \cos(\phi + \pi/2) \\
 I_3 &= O_f + A \cos(\phi + \pi) \\
 I_4 &= O_f + A \cos(\phi + 3\pi/2)
 \end{aligned}
 \tag{3.7}$$

From these four measurements the phase can be directly obtained by calculating

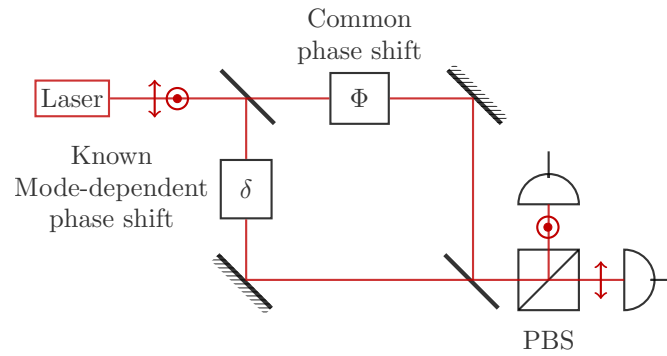


Figure 3.7: Linearizing the phase with two optical modes. Two orthogonal linear polarizations are shown here, but the general principle applies for any kind of optical modes: two different frequencies, transverse-spatial modes in fibers, temporal modes... Adapted from [77].

the following arctangent:

$$\phi = \arctan\left(\frac{I_2 - I_4}{I_3 - I_1}\right) \quad (3.8)$$

It is also possible to work with only two phase shifted measurements, typically shifted by $\pi/2$ radians, but that would involve a pre-calibration step to determine the offset O_f and amplitude A , as explained for instance in [76]. The disadvantage is that relatively unstable systems might require frequent calibrations to adapt to the changing conditions.

A variety of interferometer schemes have emerged to linearize the phase measurements and stabilize the system exploiting these concepts, mostly in the field of phase microscopy due to its large number of applications. In the following sections we describe how the phase is linearized in many of them. As we will see, our stabilization scheme reliably keeps the nominal phase fixed at virtually any desired value for minutes or longer. It will be demonstrated in Chapter 6 that an advantageous feature compared to other methods lies on the fact that, as long as the phase changes in the system are not too steep, it can even measure the phase shift induced by the sample in an intrinsically linear way.

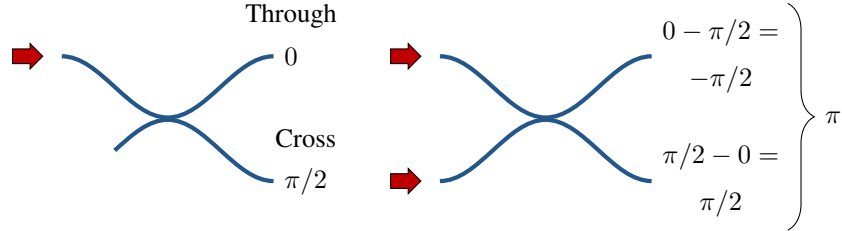


Figure 3.8: Phase relationship between output ports of a lossless 50:50 2x2 beamsplitter. The input beam undergoes an additional $\pi/2$ phase delay for the crossing state. If both input ports are excited, the phase difference between output ports is therefore π radians.

3.4.1.1 Different optical modes

The authors of [77] introduce a quite general approach to control the phase. It yields a linear error signal and is able to fix it at an arbitrary value, which is exactly what we need in our stabilization. Two different optical modes (polarization, frequency, transverse-spatial, temporal...) go through both arms of an interferometer. One of the arms introduces a common and unknown phase shift to both, but the second arm introduces a known mode-dependent phase shift. Once the modes are separated and the beams interfere, two interferograms give enough information to recover the unknown phase shift.

As a variation of the general theory with two optical modes, in [78] two circularly polarized beams are interfered and passed through an analyzer (polarizer). Two circularly polarized beams add up to form a linearly polarized beam oriented according to the relative phase between both beams. Therefore, by detecting the intensity going through the analyzer the authors can stabilize the system. The technique needs a system very robust in terms of polarization, but the advantage of this technique is that the phase scanning range is very wide.

A consideration to take into account in our particular 4π setup is the need to match the same optical mode at least at the sample plane. For instance, regarding light polarization, it needs to be the same there, otherwise they would not interfere coherently to produce a 4π PSF.

3.4.1.2 3x3 splitter

Combiners or splitters can also be employed to linearize the phase. In a lossless 2x2 coupler or splitter the complex transmission coefficients for the through and cross output ports are phase shifted by $\pi/2$ radians, as illustrated by Fig. 3.8. As a consequence, when both input ports are excited, the phase relationship between

beams at the output ports is $-\pi/2$ and $\pi/2$. The resulting phase difference between output ports of π radians is insufficient to remove the phase ambiguities as explained in the previous phase linearization section.

To obtain the phase without ambiguities, we would ideally get a $\pi/2$ phase shift between output ports of the coupler, or at least any other value that is not a multiple of π . For a 2×2 splitter the outputs will be π phase shifted regardless of the splitting ratio, so a minimum of three ports are needed to get an arbitrary phase between them [79]. In a 3×3 splitter the phase shift at the output ports does depend on the splitting ratio, and for an homogeneous splitting ratio 1:3 the phase shift between ports will be $2\pi/3$ degrees.

A laser frequency was stabilized with this method in [80] employing a 3×3 coupler, and we could also use the same principle to stabilize our system.

3.4.1.3 Off-axis interferogram

Figure 3.9 illustrates the different intensity patterns generated by the interference between two co-propagating plane waves and two plane waves propagating with an angle with respect to each other. Two tilted beams produce an intensity pattern that is known as off-axis interference. The phase shift between beams is now position dependent, so an array of detectors or a CCD can probe many phase shift values simultaneously, allowing the linearization of the phase.

The authors of [76] stabilized the fluctuations in a Mach-Zehnder interferometer by using off-axis interference. They got a linear phase signal by placing two photodetectors at different positions of the interferogram, namely $\pi/2$ radians away. These two signals were then fed to a computer that performed an arctangent calculation leading to a signal linearly proportional to the phase, which is later re-introduced into the system.

There are many variations of this type of stabilization, to mention another one, in [81] they use four photodetectors placed at $\pi/2$ intervals in an off-axis interferogram. As previously mentioned, taking four measurements instead of two circumvents the need of a system pre-calibration.

3.4.1.4 Phase modulation

A common approach [82, 83], originally developed in the field of electronics and usually unknown to people in the field of optics and photonics, involves modulating the phase shift in the system with a frequency ω . If the modulation amplitude is small enough the influence over the nominal phase is minuscule. The detector

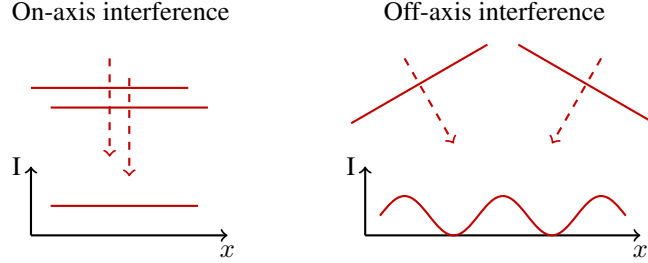


Figure 3.9: Intensity patterns generated by the interference between two plane waves that are co-propagating and when they propagate with an angle with respect to each other. These two configurations are called 'On-axis' and 'Off-axis', respectively.

measures a signal of the form:

$$I_d = I_1 + I_2 + 2\sqrt{I_1 I_2} \cos(\phi) \quad (3.9)$$

where the phase shift ϕ is

$$\phi = \alpha + \alpha_d \sin(\omega t) \quad (3.10)$$

and α and α_d are the interference phase shift of interest and the modulation amplitude, respectively.

Because of the nonlinear relation between I_d and ϕ , the ω -frequency modulation results in a number of harmonics in ω , where the first I^ω and the second $I^{2\omega}$ terms are described by

$$\begin{aligned} I_d^\omega &= 4J_1(\alpha_d)\sqrt{I_1 I_2} \sin \alpha \sin(\omega t) \\ I_d^{2\omega} &= 4J_2(\alpha_d)\sqrt{I_1 I_2} \cos \alpha \cos(2\omega t) \end{aligned} \quad (3.11)$$

where $J_1(\alpha_d)$ and $J_2(\alpha_d)$ are the Bessel functions of the first kind or order 1 and 2, respectively. The terms in ω and 2ω are $\pi/2$ shifted, i.e. one is a sine and the other a cosine of α . These orthogonal components allow us to get all the information about this phase shift without ambiguities.

A much weaker signal to noise ratio characterizes the second harmonic compared to the fundamental harmonic. Yet, the modulation amplitude can be low if we use a lock-in amplifier to detect it. This comes at a price though, lock-in amplifiers use narrow-band filters, limiting the stabilization bandwidth.

The active stabilization can operate at any nominal phase value, and in a first approximation, the response of the stabilization is linear independently of the chosen value. This method in different contexts is sometimes also referred to as sinusoidal phase modulation or as Fourier analysis method because it decomposes the phase signal into its different harmonics.

3.4.1.5 Dedicated wavelength

Numerous methods stabilize the phase with an independent system, namely by using an additional and dedicated laser working at a different wavelength with respect to the pump. Strictly speaking this is not a method to linearize and stabilize the system in itself, but this approach is so ubiquitous that it deserves a separated treatment. To linearize the phase and stabilize the system, this approach is often combined with some of the previous ideas.

A specific implementation with a dedicated laser is for instance discussed in [84]. It describes the stabilization of an interferometer consisting of kilometer-long fibers, so the phase variations are much stronger than in our interferometer. The stabilization results in a phase variation of 0.06 radians, or equivalently 3.43 degrees.

Similarly, reference [85] employs a dedicated laser. The image of a single fringe pattern of an off-axis interferogram is processed in a computer in order to get a phase error signal that is fed back into the system to correct it. The technique has the limitation that it cannot function for any nominal phase value, but only for an angular range of around 310 degrees.

We decided to use the Raman pump laser as well for the stabilization, reducing the number of dedicated optical components in the setup and removing the need for the additional laser source.

3.4.2 Stabilization in the 4π Raman microscope

There is a fundamental difference preventing us from using the conventional stabilization techniques described above: we must access the phase at the sample plane without direct access to it. The interferometer in our setup was tailored to compensate for the phase fluctuations in the system introduced by the fibers, but also to control the relative phase between both pump beams at the sample plane. As we describe in the following paragraphs, the interferometer permits us to manipulate the position of the fringe pattern by changing the stabilization parameters.

The stabilization consists of an active feedback that converts phase variations into a compensation signal that is reintroduced into the system through the phase

shifter. The feedback loop is depicted in Fig. 3.4, representing the electrical connection between the photodetector and the translation stage. Depending upon whether the Proportional-Integral-Derivative controller (PID) (Stanford Research Systems, SIM960 Analog PID Controller, 100 kHz bandwidth) is turned on or off we can have two functional regimes. When the PID is turned off the system is not stabilized, i.e., the setup is on free-running mode. We use input channel 1 of the oscilloscope to directly observe the signal from the photodetector. Following the model for the detector signal $V = O_f + A \cdot \cos\phi$ we can now calculate the voltage corresponding to any desired phase shift between pump beams at the partial reflector plane. As the thermal phase fluctuations evolve and change ϕ over a range bigger than π , the amplitude value A of the cosine and the offset O_f can be obtained. We can speed up this process by forcing some phase variations into the system through the phase shifter.

For the stable regime, the PID is turned on. We then set the appropriate PID parameters (proportional, integral and derivative gains, and internal setpoint) to stabilize the system at the chosen voltage. The role of the PID is to drive the translation stage, which we call *phase shifter*, in such a way that its input, the detector signal, is kept fixed at the voltage corresponding to the desired nominal phase.

The phase shifter consists of a piezoelectric actuator (Thorlabs DRV517) that moves one of the collimating lenses with its corresponding attached fiber in order to modify the optical path length of the bottom arm of the interferometer. Despite having a cut-off frequency of 300 Hz, relatively low compared to similar studies [84], it significantly reduced the environmental phase fluctuations present in our setup as shown in Fig. 3.10. As this is the component with the lowest cut-off frequency, it is the element limiting the stabilization bandwidth. The parameters of the PID controller were adjusted to set the desired nominal phase. The feedback loop was turned on after 20 seconds and in the stabilized regime we set the nominal phase to a different value every 10 seconds. The standard deviation of the different steps was approximately $\sigma = 0.06$ rad, or equivalently 0.01λ , where $\lambda = 785$ nm is the pump wavelength.

The measurement and sample employed for the results shown in Fig. 3.10 were part of the super-resolution experiments discussed later in Chapter 4. The sample consisted of a stack of three nanolayers on top of a 1 mm thick CaF_2 substrate with refractive index 1.43. The nanolayers from top to bottom are: polymethyl methacrylate (43 nm thick PMMA), amorphous titanium oxide (23 nm thick TiO_2), and e-beam resist (64 nm thick ARP). The PMMA and ARP layers were spin-coated, whereas the TiO_2 was deposited via sputtering. The main components of ARP, according to the manufacturer (ALLRESIST), are poly(α -methylstyrene-co-methyl

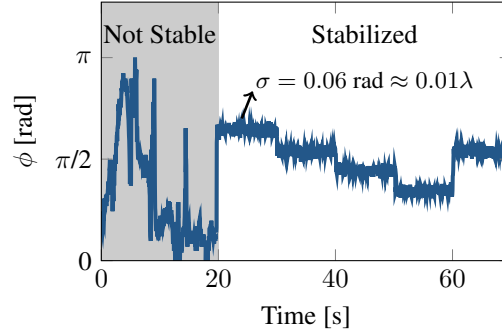


Figure 3.10: Stabilization of the phase shift between pump beams in the 4π Raman microscope. The phase control is demonstrated by changing the nominal phase of the system every ten seconds. Shaded area indicates a free-running regime showing the environmental phase noise. From that part, we obtained the values $O_f = 52$ mV and $A = 35$ mV, that were used to convert the initial voltage measurement into the phase ϕ plotted here.

chloroacrylate), an acid generator and the solvent anisole. As it is a sample that can be measured in air, we used the Zeiss 100x/0.9NA objective lens on the top part of the microscope.

The maximum time that the system can be stabilized is in the order of tens of minutes, which is much longer than the acquisition time of a single Raman spectrum, typically around 10 seconds. The main factor limiting the stabilization time is given by the thermal drift of the different stages (piezo stage of the sample, piezo stages of the objective lenses, reflector stage...). The drift misaligns the optical components, which alters the intensity of the beams reaching the detector and, in turn, the O_f and A of the measured interference pattern. For long imaging experiments we therefore re-set the stabilization parameters before every Raman measurement, but for other shorter experiments we keep the nominal phase fixed and stable during the entire scan of the sample.

Figure 3.11 shows the combined consequences of thermal fluctuations and the drifts of the stages under realistic measurement conditions. To have an idea of the evolution of the bottom reflection intensity after a long measurement, we can simply block the top arm. After 125 seconds the reflection decreased by 10%, and that explains why the interferogram offset and amplitude slowly change with time. The fast oscillations at the beginning and end of the measurement are introduced manually to better visualize how these changes. The O_f is given by the mean value of the fast oscillations, while the A is given by half the difference between their maximum and minimum values. The particular values of O_f and A at the beginning of this experiment are 75 mV and 5 mV, respectively, but these will vary for other experiments.

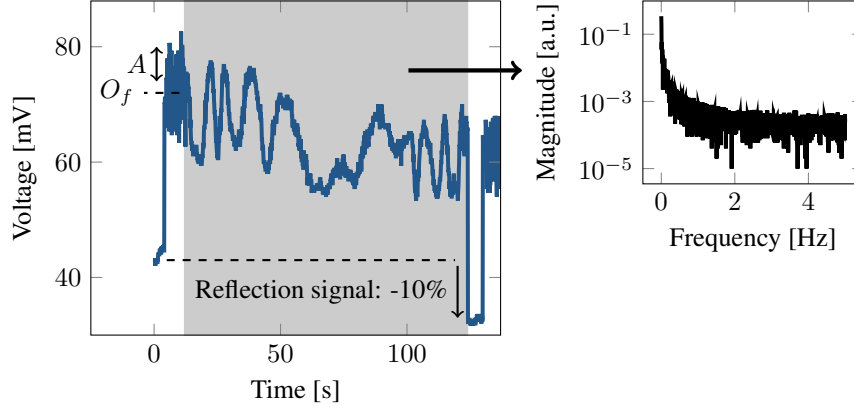


Figure 3.11: The bottom reflection signal was also measured twice, at time 0 and 125 seconds, by manually blocking the top arm of the interferometer. The reflection decreased 10% after that time due to drifting stages. Shaded areas indicate the evolution of the interferogram mainly due to thermal fluctuations and its spectrum is shown on the right plot.

Depending on whether the proportional gain parameter of the PID controller is set to a positive or a negative value, the feedback can be positive or negative. In terms of the nominal phase values, the sign of the gain changes the range that can be accessed. For a positive gain the range goes from 0 to π radians, as in Fig. 3.10, or from π to 2π for a negative gain. As this is based on the slope of the cosine of the interference pattern, the zero slope close to the range limits 0, π or 2π values and the presence of noise in the stabilization signal renders the stabilization unstable. In practice, this means that there is a small set of nominal phases around those limits that we cannot access during the measurements.

3.4.2.1 Axial scans

In the experiments that we will discuss in the following chapters, we will measure different parts of the samples. It is important to make a distinction between transversal and axial scans of the samples because the phase stabilization can change the 4π PSF depending on the scan direction.

For transversal scans no special considerations have to be taken into account. As with single-beam microscopy, we do not expect any change of the PSF for different sample positions, at least for weakly phase-inducing samples. The stabilization and the PSF overlap with the sample are expected to remain unchanged.

On the other hand, axial scans do require special considerations. The phase reference is always anchored to the plane at which the reflection occurs, either the

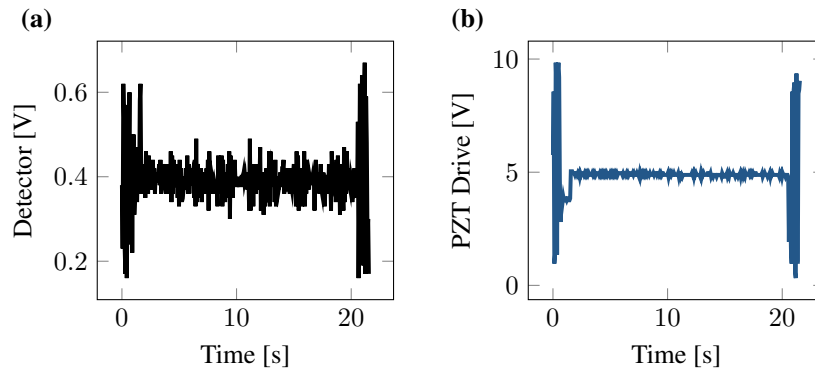


Figure 3.12: Axial scan using a water immersed sample and the partial reflector. (a) Channel 1 of the oscilloscope connected to the detector. (b) Channel 2 of the oscilloscope driving the phase shifter. The temporal sequence is as follows: 0 s - unstable regime, 2 s - stabilize at $z = 20.4 \mu\text{m}$ and gradually move until $z = 17.4 \mu\text{m}$, 21 s - unstable regime.

sample substrate interface or the partial reflector, so we identify two cases: 1 - the PSF is unaltered by the sample axial position because the phase is anchored to the partial reflector that does not move; 2 - the PSF is anchored to the sample, so it follows it when scanning axially.

To study these two cases we axially scan a CaF_2 slide (1 mm thick) while focusing close to its top air-slide interface. First we do not place the partial reflector in the system. If the sample moves down, we expect the fringe pattern should also move down, and we can see that through the voltage driving the phase shifter (corresponding to the phase shift) measured. As demonstrated in Fig. 3.12, a linear dependence of the phase shift corresponds to the physical distance the sample is moved. The Zeiss Water immersion 63x/1.0 objective lens was used to obtain these results.

Placing the partial reflector in the system we can now study the case when the phase is anchored to the sample. When the samples moves axially, the fringes should not move, they should remain fixed. A constant value of the voltage driving the phase shifter is therefore expected and demonstrated in Fig. 3.13. The Zeiss 100x/0.9NA objective lens was used to obtain these results. Note that we can only use the partial reflector with water immersed samples, for which the sample reflection is negligible or when measuring far from the slide interface. This avoids interference effects between the reflections from the sample and the partial reflector.

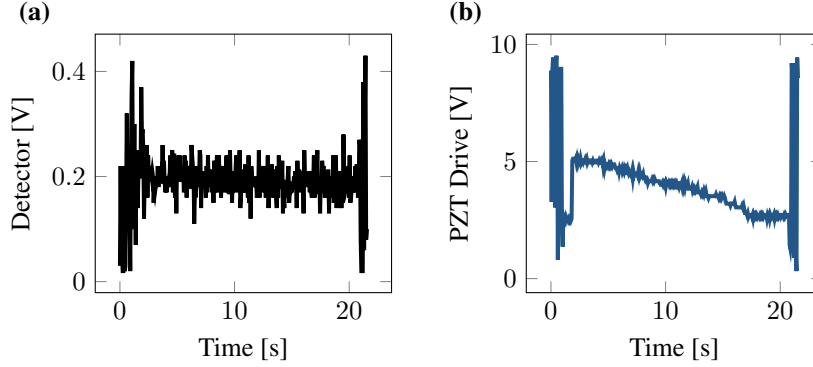


Figure 3.13: Axial scan using the sample reflection. (a) Channel 1 of the oscilloscope connected to the detector. (b) Channel 2 of the oscilloscope driving the phase shifter. The temporal sequence is as follows: 0 s - unstable regime, 2 s - stabilize at $z = 28.47 \mu\text{m}$ and gradually move until $z = 25.47 \mu\text{m}$, 21 s - unstable regime.

3.5 Conclusion

We have seen how to convert a commercial microscope, with fiber-based access to its top and bottom sides, into a 4π microscope by connecting it to a tailored Michelson interferometer. An isolator in one of the arms of the interferometer and the reflection from the sample plane are key components to be able to monitor and control the phase shift between pump beams at the sample plane. If the reflection from the substrate interface is too weak, we can alternatively use a partial reflector placed as close as possible to the sample.

Thanks to the optical setup arrangement we are able to stabilize the phase shift between beams for as long as the Raman measurements take. A dedicated laser source is not required, as in many of the past similar studies. Compared to the technique based on the modulation of the optical path length of one arm of the interferometer, our setup involves a simpler electronic scheme with just a proportional-integral-derivative controller. This simpler scheme, however, is still sensitive to drift of the stages if the measurements are longer than few seconds.

4

Nanolayers & Super-resolution

In this chapter, we study the ability of 4π Raman microscopy to provide super-resolution. We start by discussing how the thickness of a nanolayer can affect this ability. Once the ground rules are established, we study a nanolayer stack. We identified each of the nanolayer's Raman spectral features and retrieved their relative optical separation with deep subwavelength precision.

| | | |
|------------|--|-------------|
| 4.1 | Introduction | 4-1 |
| 4.2 | Interaction between a standing wave pattern and a nanolayer | 4-3 |
| 4.2.1 | Raman contrast and detection visibility | 4-4 |
| 4.2.2 | Silicon membrane | 4-7 |
| 4.3 | Super-resolution 4π Raman microscopy | 4-10 |
| 4.3.1 | Phase shifting super-resolution principle in three steps | 4-11 |
| 4.3.2 | Experimentally super-resolving a stack of nanolayers | 4-11 |
| 4.4 | Conclusion | 4-18 |

4.1 Introduction

During this project we explored the potential of 4π Raman microscopy to resolve sample features beyond the diffraction limit, i.e., its potential for super-resolution measurements.

The wave nature of light means it is subject to diffraction, a phenomenon that does not allow it to be focused to an infinitely small point. When the resolution of a microscope is smaller than the diffraction limit, roughly half the wavelength, then it is said to be a super-resolution microscope.

Since the 1980s the microscopy field has boomed in terms of resolving power for living cell imaging thanks to the surge of a diverse new set of fluorescence super-resolution techniques that can be grouped under the name '*fluorescence nanoscopy*' [13, 14].

The ability to distinguish two close objects is limited by diffraction, but the precision at which we can localize those objects is not. Super-resolution fluorescence techniques bypass the spatial diffraction limit exploiting this idea and dimensions other than space, whether it is frequency, time, or any other. For instance, well established techniques such as STORM [86–88] or PALM [89–92] rely on separating the response of two neighbouring particles in the time domain by switching on or off their fluorescence. When only one of the particles is fluorescing it can be localized with very high precision. Then, the particle is switched off, and the second particle switched on. The second particle can then be precisely localized as well. The final image is formed, somehow artificially, by drawing two points in the coordinates obtained. These two points now substitute the wider diffraction limited and overlapping blobs that initially could not be separated. If the process is repeated for many of the points composing the sample the result is a super-resolved and faithful image of the sample.

Stimulated Emission Depletion (STED) microscopy [93, 94] is another super-resolution imaging technique based on a different principle: the selective deactivation of fluorophores. It uses two laser pulses of different wavelengths. The first pulse excites the fluorophores within the focal volume to its fluorescent state. The second pulse is a doughnut-shaped beam that de-excites any fluorophores surrounding the excitation focal spot. The result is that only the fluorophores that lie within the central dark spot of the doughnut will be detected. Since the de-excitation process is non-linear, the remaining volume of excited fluorophores can be, in theory, infinitesimally small.

Raman microscopy [17, 18], having the fundamental advantage of being label-free, is certainly following the same pathway to obtain super-resolved Raman images of cells and new research avenues are already being explored [19–22]. Through the study of a nanolayer stack, we will show here that using a 4π configuration with Raman microscopy has a great potential to help in this quest.

In order to achieve super-resolution we rely on different spectral responses (frequency domain) of the nanolayers composing the stack and some a priori

knowledge about the kind of sample used for these experiments —we know the sample is a stack of different nanolayers. It would be much more complicated to get super-resolved information following the method explained here from complex biological samples, from which we do not know anything a priori.

Nanolayers are of high interest in a variety of fields, such as in the fabrication of battery anodes [95], optical coatings [96], pharmacology [97] and biological membranes [98, 99]. In areas such as the arts and archaeology, the non-invasive nature and the ability to probe the chemical composition of Raman spectroscopy is essential. It allows selecting the suitable conservation approach and understanding the artist's technique and the artwork history [100]. The study of a nanolayer stack is thus a good starting point in the road towards super-resolution Raman 4π microscopy.

Exploring the ability of this microscope to measure certain features of the nanolayers with better resolution than permitted by the diffraction limit is the topic of the second part of the chapter. We will obtain the relative distance between nanolayers in a nanolayer stack, much in the same way that super-resolution fluorescence techniques do. However, we first need to discuss in the following section how the thickness of a single nanolayer can influence the way it interacts with the 4π PSF and the Raman signal intensity.

4.2 Interaction between a standing wave pattern and a nanolayer

A smaller PSF is a requirement to obtain a better resolution, where its smallest features allow for its increased resolving power. A 4π PSF, however, is special in the sense that it has a much smaller central lobe, but it also has secondary lobes. Thus, if a nanolayer is thin enough to overlap only with the main lobe, then the smallest features of the PSF will lead to a better ability to resolve, for instance, the sample thickness. Conversely, if it is so thick that it also overlaps with the secondary lobes, then trying to use the smallest 4π PSF features to better resolve the sample will be futile. It would effectively be as though it were illuminated by a conventional PSF with bigger features. An indication of the smallest PSF features being leveraged as expected is to axially scan the nanolayer and see if the signal changes as fast as the 4π features or as slow as a conventional PSF. This is where the concept of *contrast* or *visibility* comes into play.

As we will see, the refractive index of the nanolayer also plays a big role, not just because it changes the optical length of the nanolayer, but because it can lead to prominent interference effects if it is high enough. The insights obtained in this

section will help better understand the limitations of 4π microscopy in general, but more specifically, they will expose the challenges involved on going beyond the diffraction limit.

4.2.1 Raman contrast and detection visibility

The contrast or visibility of an interference pattern generated by two beams quantifies its intensity change when one of them is phase shifted. Contrast and visibility are synonymous terms in this text, but to help the reader avoid confusions, from this point forward we will refer to the changes of the Raman signal as *Raman contrast* and to the changes of the detector signal as *detection visibility*.

A high Raman contrast is a sign that the 4π microscope can provide improved resolution when compared to a conventional microscope. The detection visibility is important as an indication of how sensitive we are to the nominal phase of the system and, therefore, of how good the phase stabilization can be.

The Raman contrast can be defined in two equivalent ways—from the excitation or from the collection standpoint. In the former, we look at the pump energy that overlaps with the sample and, in the latter, we consider the collected Raman signal. We focus on the collection perspective as it will help us better understand the following experiments. The contrast is then the difference between the maximum and minimum Raman intensity that can be excited with the counter-propagating beams. We will typically normalize it to be in the range from 0 to 1.

In order to obtain the contrast provided by a nanolayer we need to measure its overlap with the sinusoidal pattern generated by the interference between two counter-propagating plane waves. In Fig. 4.1, two extreme cases are depicted, where the sinusoidal curve has the maximum and minimum overlap possible with a layer of thickness d . Mathematically, the contrast is calculated as the difference between the two overlap integrals normalized with respect to the thickness of the layer, which results in a sinc function. More specifically, the minimum integral overlap I_{\min} depicted in Fig. 4.1(b) is subtracted from the maximum integral overlap I_{\max} represented in Fig. 4.1(a), and then divided by the sum of both.

$$I_{\max} = \frac{1}{2} + \frac{1}{2d} \int_{-d/2}^{d/2} \cos\left(\frac{4\pi z}{\lambda}\right) dz \quad (4.1)$$

$$I_{\min} = \frac{1}{2} + \frac{1}{2d} \int_{-d/2}^{d/2} \cos\left(\frac{4\pi z}{\lambda} - \pi\right) dz \quad (4.2)$$

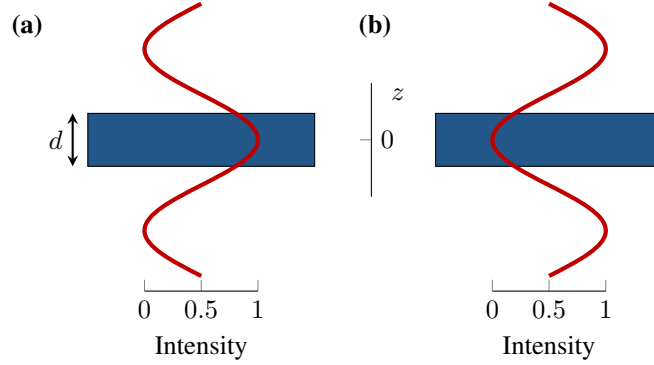


Figure 4.1: Contrast exhibited by a nanolayer. **(a)** Maximum and **(b)** minimum overlap between a sinusoidal curve, representing the intensity pattern generated by two counter-propagating plane waves, and a nanolayer of thickness d . The contrast is defined as the normalized integral overlap of (a) minus the normalized integral overlap of (b), and all of that divided by the sum of these same two integrals. The contrast dependence with the layer thickness results in the sinc function shown.

$$\text{Contrast} = \left| \frac{I_{\max} - I_{\min}}{I_{\max} + I_{\min}} \right| = \left| \text{sinc}\left(\frac{2\pi d}{\lambda}\right) \right| \quad (4.3)$$

From these illustrations it becomes clear that only the Raman signal from an infinitesimally thin layer could yield an ideal contrast and, in turn, twice as many counts as a Raman spectrum collected by a uniform intensity pattern. Conversely, if the infinitesimally thin sample's position corresponds with the minimum value of the intensity pattern it could reduce the Raman counts to zero. The contrast is thus dependent on the thickness of the sample under study. The intuitive explanation for this dependence is that features much bigger than the wavelength completely fill the confocal volume of the microscope. Therefore, the Raman signal remains unchanged for different fringe positions.

The detection visibility is similarly defined as:

$$\text{Visibility} = \frac{I_{\max} - I_{\min}}{I_{\max} + I_{\min}} \quad (4.4)$$

The difference is that now I_{\max} and I_{\min} are directly measured by the detector in the interferometer. In this particular case of a non-reflective layer, it would not depend of the thickness. However, as we will see in the following sections, it will generally depend on the thickness and refractive index of the sample and, if the external reflector is used, on its reflection coefficient.

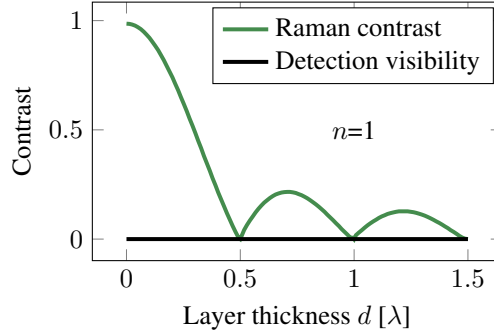


Figure 4.2: Raman contrast and detection visibility vs. thickness of a nanolayer with unitary index n , the same as the air around it. No reflections happen at the two air-layer interfaces so the detector visibility is zero. The general trend of the Raman contrast is that it decreases for wider layers, but it is zero when the thickness matches multiples of half the wavelength.

Figure 4.2 reveals the influence of the thickness on the Raman contrast and the detection visibility. The calculation was based on a transfer matrix approach detailed in Appendix A, where the refractive index of the layer was unitary, the same as the surrounding air. The Raman contrast shows a periodic null at multiples of half the wavelength λ , meaning that its intensity does not change when the sinusoid is moved. The result matches perfectly with the *sinc* function predicted above. The same refractive index as the surroundings means that the presence of the sample does not modify in any way the intensity pattern or point spread function of the microscope. Another consequence of the layer's unitary index is that there are no reflections, which is why the detection visibility observed is constant regardless of the layer thickness. Only the transmitted beam reaches the detector, and its intensity does not change. It is important to have a non-zero visibility, as it is needed to be able to stabilize the system. The external reflector must be used to increase the contrast at the detector when necessary.

In the following section we will see that when the refractive index of the layer is higher than the refractive index of the surroundings, the Raman contrast and detection visibility curves becomes more intricate. Additionally, the conclusions drawn here assume a perfect sinusoidal illumination pattern produced by plane waves, but they still apply to the interference pattern generated by the focused beams in 4π microscopy.

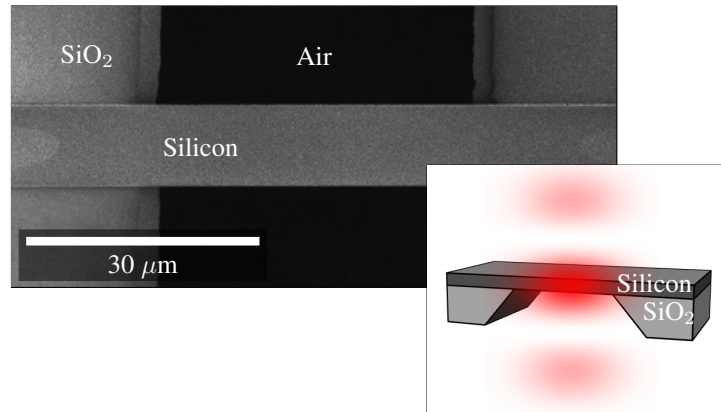


Figure 4.3: Scanning electron microscope picture of a 215 nm thick free-standing silicon membrane. The fabrication details are described in [101] and the inset shows a 3D schematic view of the membrane being measured by a 4π microscope.

4.2.2 Silicon membrane

The study of a free-standing membrane of silicon serves us to delve deeper into the concepts explained in the previous section about the Raman contrast dependence on the layer thickness. We use here the 215 nm thick silicon free-standing membrane shown in Fig. 4.3. It originally had a silicon oxide (SiO_2) substrate below the silicon layer but the bottom beam would suffer strong aberrations travelling through it. It was therefore removed by following the recipe described in [101].

When the membrane is excited with a single beam coming from one side we get a typical Fabry-Perot cavity transmission response, shown in Fig. 4.4. The silicon refractive index at the pump wavelength of $\lambda = 785$ nm is 3.7, and its optical length is $215 \cdot 3.7 = 795.5$ nm, or in terms of wavelength 1.01λ . Since the optical length of the membrane almost perfectly matches the wavelength it acts as a Fabry-Perot cavity almost at resonance.

A similar calculation when two counter-propagating beams reach the cavity is shown in Fig. 4.5. Due to the close resonance, the detection visibility was low but still enough to stabilize the phase during this experiment.

In Fig. 4.6(a) the main Raman peak of the silicon layer at 520 cm^{-1} is shown. We scanned the optical phase of one of the pump beams. Scanning the phase within a small range of 2π radians is virtually equivalent to axially moving the sample, as in both cases the fringe pattern moves axially with respect to the sample. The Raman counts, normalized with respect to the standard or single-pump Raman

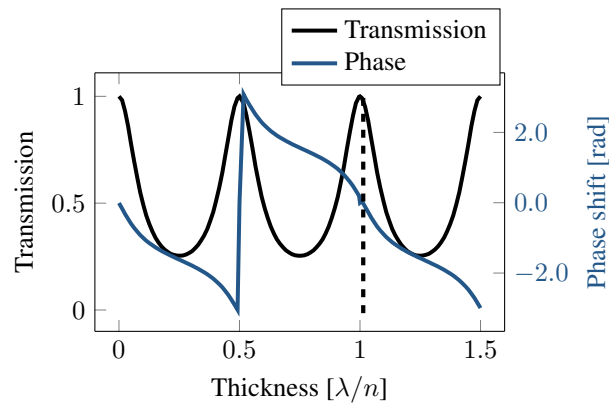


Figure 4.4: Transmission intensity and phase of a layer of refractive index 3.7, surrounded by air and for different thicknesses. The dashed line indicates the value corresponding to the 215 nm thick silicon membrane used in the experiments, which lies very close to a Fabry-Perot resonance.

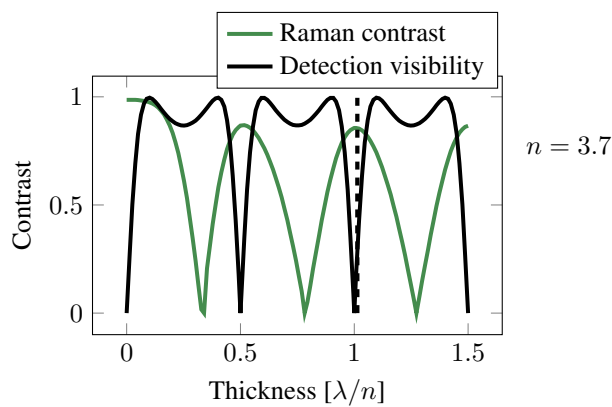


Figure 4.5: Raman contrast and detection visibility for a layer of different thicknesses and refractive index 3.7 excited with two counter-propagating plane waves. The 215 nm width of the silicon membrane is indicated with a dashed line, which lies very close to a Fabry-Perot resonance. Even though the detector contrast is quite small, it was still possible to stabilize the system.

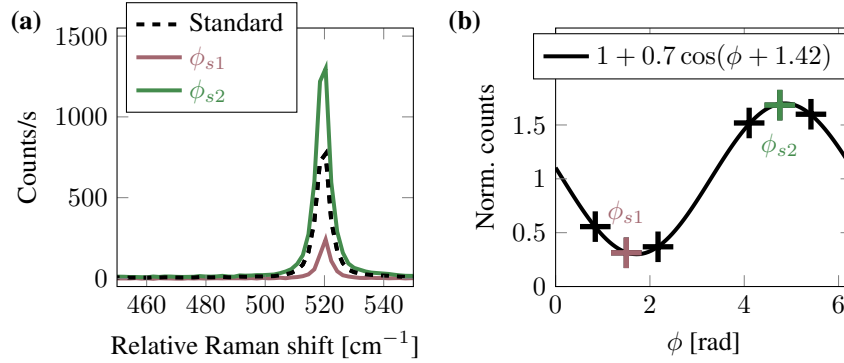


Figure 4.6: (a) 4π Raman spectra of the 215 nm silicon layer. (b) Response of the 520.4 cm^{-1} peak versus nominal phase and normalized with respect to the standard response. Crosses indicate experimental data points. Red and green colors link data from both figures. The sinusoidal fitting follows the curve $1 + 0.7 \cos(\phi + 1.42)$.

spectrum, are plotted and fitted to a sinusoidal curve in Fig. 4.6(b). The sinusoidal curve should ideally reach a maximum value of 0.85 as seen in Fig. 4.5, but instead, we obtain 0.7. The different volumes of the sample being excited by the top and bottom objectives, as well as a slight intensity mismatch between pump beams, can explain the difference.

The objectives employed for this experiment were a Zeiss 100x0.9NA inf/0 and a Nikon 20x0.5NA, for the top and bottom parts, respectively. The measurements took 5 seconds per spectra, which is relatively quick because of the strong Raman peak. The fast measurements helped keep the drift of the piezo stages to a minimum. We initially wanted to use the thinnest layer possible to obtain an almost ideal Raman contrast, but that would also decrease the Raman signal strength. Despite of being optically thick, the silicon membrane exhibited a strong contrast because we worked close to a resonant thickness.

A strong absorption at the pump wavelength could influence the Raman contrast and the detection visibility, but we can show that it was negligible in such a thin layer. The absorption coefficient of silicon at 785 nm is $\alpha = 1186.8 \text{ cm}^{-1}$ [102], and the intensity of the transmitted beam through the layer with respect to the incident beam is determined by Beer-Lambert law:

$$\frac{I}{I_0} = e^{-\alpha \cdot \text{thickness}} = e^{-0.0255} = 0.975 \approx 1 \quad (4.5)$$

In summary, the silicon membrane was an adequate sample to test the behaviour of our microscope. It provided a good compromise between Raman signal, Raman

contrast and detection visibility, while having a negligible absorption.

4.3 Super-resolution 4π Raman microscopy

During the last decades many super-resolution microscopy techniques have been developed, most of them involving fluorescent dyes that are introduced into the samples. One of the main disincentives is that external dyes might affect the sample's internal processes. It is possible to use intrinsic fluorescent molecules already present in the sample, but not all the samples have them. If they do have them, the fluorescence is most likely very weak.

Super-resolution fluorescence techniques have no conventional resolution limit. The ability to switch on and off the fluorescence molecules is the enabling factor for super-resolution imaging. It might seem then that diffraction does not play a role, and yet these techniques greatly benefit from tightly focusing the light with high NA objectives, as well as from using a 4π arrangement. Their limited resolution is rather given by the performance of the fluorophores regarding the number of emission cycles, their quantum efficiency, and photobleaching. The higher collection efficiency of 4π microscopy is hence directly translated into an improved resolution. Namely, doubling the number of fluorescence photons detected with a Type B or Type C configuration enhances the localization precision by $\sqrt{2}$ -fold [103]. The synergistic combination of 4π with super-resolution techniques is currently the most light-efficient and the highest resolution approach for three-dimensional live-cell imaging [9–11].

Raman microscopy has the fundamental advantage of being label-free and many studies are certainly following the same trend that fluorescence techniques have been following for years —the trend towards super-resolution Raman imaging [19–22]. A higher illumination and collection efficiency is certainly beneficial for Raman imaging. So our hope is that the 4π strategy will once again push the resolution limits, only this time in Raman microscopy.

In the previous sections, we have studied a 4π Raman measurement of a single nanolayer. In this section we discuss the measurement of a stack of nanolayers. We explain how the sub-wavelength optical path between nanolayers can be recovered, which is, after all, a way to achieve super-resolution. We localize the barycenter of each nanolayer independently relying on their distinct Raman fingerprints to bypass diffraction.

4.3.1 Phase shifting super-resolution principle in three steps

Here we describe the process to go beyond the diffraction limit in terms of the axial resolution. In order to resolve the distance between two thin layers with very high resolution, we follow the three-step recipe illustrated in Fig. 4.7:

- First, we isolate the different Raman fingerprints. We can do this by measuring the isolated materials from which the different nanolayers are made from. We actually fabricated three samples apart from the main stack of nanolayers, each with a single nanolayer of the corresponding material on top of a CaF_2 substrate. We can measure the Raman fingerprint of each of them so that we can clearly identify the corresponding spectral features when the more complex stack is measured.
- Then, we take a few measurements while changing the phase shift between the beams ϕ , i.e., while moving the fringe pattern. We recover a sinusoidal curve for each layer, with a certain phase shift and Raman contrast.
- Lastly, we quantify the shift between the sinusoidal curves $\Delta\phi$, which is related to the optical distance between layers by $\Delta z = \frac{\lambda}{2\pi n_{\text{eff}}} \Delta\phi$. The effective refractive index n_{eff} is the weighted refractive index average, and could be estimated if the layers' refractive indices and thicknesses were known. The thickness of the individual layers could actually be estimated by their Raman contrast as we have seen previously, but in general the indices will be unknown. The key aspect is that we can obtain $\Delta\phi$ very precisely.

The 3-step recipe is rooted on the idea that the layers' thickness is encoded in the Raman intensity changes at different depths. In the following section we will discuss a concrete implementation.

4.3.2 Experimentally super-resolving a stack of nanolayers

Determining the thickness of layers and their chemical make-up in a non-invasive way is important, for instance, in the study of artworks. The idea that the layers' thickness is encoded in the Raman intensity changes at different depths has already been employed in [100] for these application, but it only attains a limited resolution of a few microns. In 4π fluorescence microscopy the same underlying idea yielded below 20 nm resolution in the determination of the axial position of fluorescent molecules, but only when the molecules are temporally and spatially isolated [10]. The next experiment demonstrates how 4π Raman microscopy can similarly determine the thickness and position of multiple layers within a layer stack with a nanometer accuracy by following the aforementioned 3 steps.

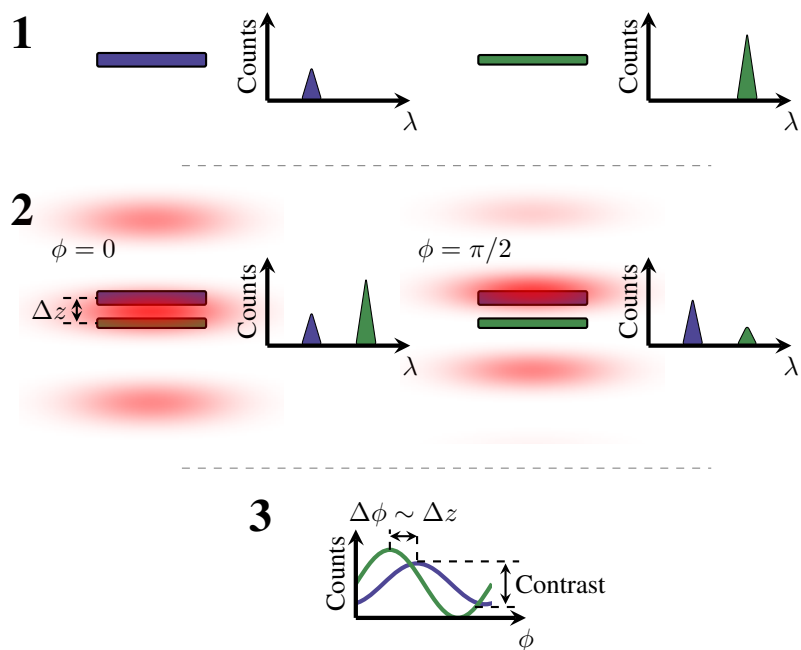


Figure 4.7: 3 steps to super-resolve the distance between layers. First, isolate the different Raman fingerprints of the different layers. Then, take a few measurements while changing the phase shift between beams ϕ . Finally, quantify the phase shift between the sinusoidal curves $\Delta\phi$, which is related to the distance between layers Δz and can be more precise than the diffraction limit.

Single-layer samples are normally characterized with ellipsometry [104] a well established tool to characterize thin layers in terms of its optical and physical parameters, such as refractive index and thickness. It requires measurements at different polarizations and its accuracy strongly depends on the sample substrate and on the fitting model employed. Refractive index and thickness are routinely extracted from reflections at different interfaces. However, more complex stacks are hardly studied with ellipsometry due to the growing complexity of the models required to fit the data. We propose 4π Raman microscopy as an alternative technique that is non-invasive, probes smaller areas of the sample and does not require any multi-parameter fitting with a complex model. More importantly, it can determine the macro- and micro-structure, optical properties and chemical composition of the nanolayers —independently and simultaneously— something hardly feasible with non-spectroscopic ellipsometry.

The working principle of the experiment is depicted in Fig. 4.8 and compared to conventional microscopy. Figure 4.8(a) illustrates the sample under study, consisting of three stacked nanolayers on top of a 1 mm thick CaF_2 substrate with refractive index 1.43. The layers, from top to bottom are: polymethyl methacrylate (PMMA), amorphous titanium oxide (TiO_2) and e-beam resist (ARP). The PMMA and ARP layers were spin-coated, whereas the TiO_2 was deposited via sputtering. The main components of ARP, according to the manufacturer (ALLRESIST), are poly(α -methylstyrene-co-methyl chloroacrylate), an acid generator and the solvent anisole.

In a standard confocal microscope, the sample in Fig. 4.8(a) would normally be probed with the typical intensity point spread function represented in Fig. 4.8(b). Conversely, the counter-propagating pump beams in 4π microscopy produce an interference pattern in the common focal spot, as shown in Fig. 4.8(c) and (d). The pump intensity at the nanolayers follows a sinusoidal curve when the relative phase between exciting beams ϕ is varied, see Fig. 4.8(e). Importantly, depending on the layers' position, their sinusoidal responses are shifted along the phase axis with respect to each other. Since these responses are obtained from independent fingerprints, we can measure their positions with much higher accuracy than the diffraction limit allows.

As a reference, the Raman spectra from the different materials is plotted in Fig. 4.9(a). They were obtained from test samples where a layer (unknown exact thicknesses) of the individual materials was spin-coated over a CaF_2 substrate. The laser was directly connected to the top part of the microscope in order to obtain standard Raman measurements.

The molecular fingerprint of the complete multilayer stack using the 4π Raman microscope is indicated in Fig. 4.9(b). The molecules from each layer can be identi-

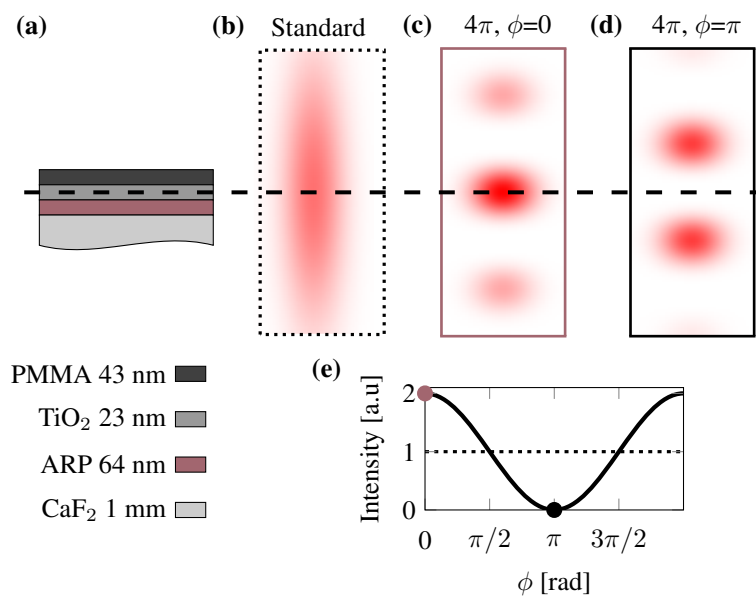


Figure 4.8: Measuring principle of the nanolayer stack with 4π Raman microscopy. Drawings not to scale. Only the pump beam is shown. (a) Sample schematic. (b) Standard confocal intensity point spread function. Note that it is independent of the phase since it is produced by just one beam. (c) and (d) 4π point spread function showing the fringe pattern when both beams are in phase and out of phase, respectively. (e) Intensity at the dashed line versus relative phase between counter-propagating beams ϕ .

fied by their unique signature. In particular, TiO_2 presents a broader fingerprint than the other components, from 0 to 630 cm^{-1} . Overall, their main spectral features are separated, allowing us to study them independently. Figure 4.9(c) focuses on the ARP Raman peaks obtained from the standard measurement and from different nominal phases. The standard measurement is done under the same conditions as the 4π measurements, except that it is incoherent. By incoherent here we mean that the interference pattern is averaged out in such a way that the point spread function would be very similar to a single-lens microscope point spread function. This is achieved by introducing high frequency phase fluctuations (much higher than the acquisition time) in the system and time averaging. We might as well block one of the excitation beams to obtain a conventional confocal measurement. However, the way we do it now keeps exactly the same excitation power, sample position, polarization, etc., which would be unfeasible otherwise.

The phase shift $\Delta\phi = 2.3 \pm 0.1$ rad between the ARP and PMMA interferograms in Fig. 4.10 is related to the optical length between these layers. If both Raman signals came exactly from the same plane, the cosine fits would overlap. For such sub-wavelength layer thicknesses the strongest Raman peaks are collected when a fringe maximum sits at their barycenters, consequently, the phase shift stems from the different optical lengths the pump has to travel to reach the layer barycenters. Based on the phase shift $\Delta\phi$ we determined an optical length between ARP and PMMA layers of 141 ± 6 nm. The measurements were repeated 5 times in order to estimate their precision, yielding the 6 nm value.

Note that the period used for the sinusoidal fittings is assumed to be $\lambda/2$. For such a low NA of the bottom objective, this should be a reasonable assumption, but it remains to be verified as the top objective has a much higher NA.

For comparison purposes we also characterized the sample by ellipsometry, which uses fitting models to extract the sample information. However, due to the high number of fitting parameters, i.e. refractive indices and thicknesses of all the layers, the result was inconsistent. For that reason, we fabricated a dedicated single-layer sample for each material of the stack and determined their thicknesses. The fabrication process of these single-layer samples was the same as in the multilayer stack. The thicknesses measured with a profilometer (Dektak) were: 43 nm, 23 nm and 64 nm for PMMA, TiO_2 and ARP, respectively. The refractive indices were: $n_{\text{PMMA}}=1.48$, $n_{\text{TiO}_2}=2.2$ and $n_{\text{ARP}}=1.56$. From these values we could calculate the total optical path separation between the centers of the PMMA and ARP layers. We obtained a value $\frac{43}{2} \cdot n_{\text{PMMA}} + 2.2 \cdot n_{\text{TiO}_2} + \frac{64}{2} \cdot n_{\text{ARP}} = 132 \pm 8$ nm, in line with the 4π Raman microscopy result.

We could enhance the Raman signal by a factor of 1.41 compared to standard confocal microscopy and obtain a 6 nm super-resolution with regard to the optical

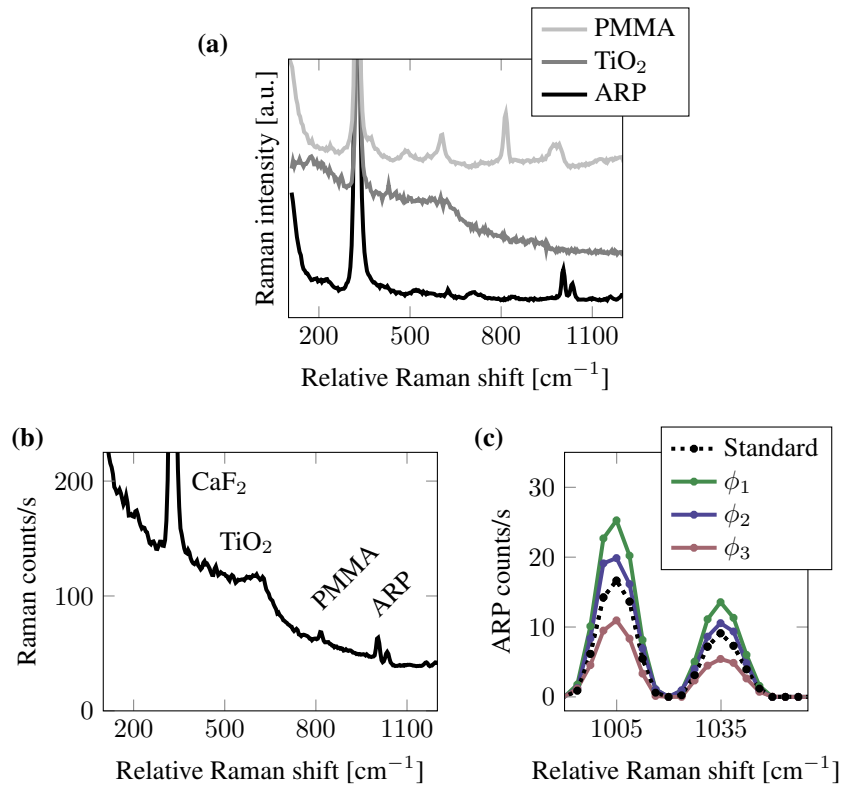


Figure 4.9: 4π Raman spectra of the nanolayer stack. (a) Spectra of individual layers obtained from reference single-layer samples. The spectra are cascaded to avoid overlaps. (b) Full Raman spectrum showing the different material contributions. (c) Zoom-in of the ARP peaks with removed background. Dashed black indicates the standard confocal spectrum. Spectra at different nominal phases are color coded.

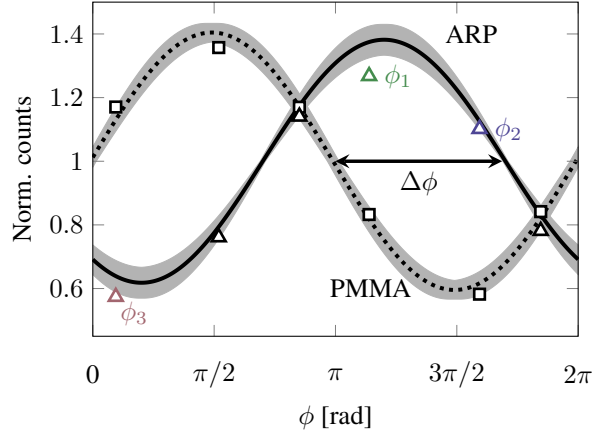


Figure 4.10: Response of the ARP and PMMA layers versus nominal phase. The Raman counts are normalized with respect to the standard response and fitted to a cosine curve. Colors indicate the same data as in Fig. 4.9. Triangles and straight line relate to the ARP experimental data points and their fit, respectively. The measurements are repeated 5 times for error analysis. Shaded areas indicate the standard deviation. The process is replicated for PMMA yielding the squares and dashed curve. $\Delta\phi$ is the phase shift between both interferograms.

length. The contrast is smaller than the theoretical 2 value due to the thickness of the layers, as explained before. Aberrations due to the 1 mm thick CaF_2 substrate are the main cause. As a reference, the particular case of a 64 nm ARP layer with refractive index $n_{\text{ARP}}=1.56$ should yield a theoretical contrast of 1.89 using the matrix transfer method in Appendix A.

Besides the experiments with the stack of nanolayers shown here, we tried to super-resolve features of biological samples. In particular, we were aiming at super-resolving parts of the sample that we knew resemble the stack of nanolayers studied in this experiment. The experiments were especially challenging though. Cell membranes are composed of different few-nanometers layers [105, 106], so in theory it should be possible to super-resolve the distance between them. However, to do so, we should be able to detect and distinguish their Raman signatures, and that is something that proved to be quite evasive. As discussed in [107], coherent Raman techniques are clearly advantageous, especially to study cell membranes, due to the stronger Raman signal collected. The review also discusses the recent developments in Raman chemical tags for cell membranes to separate its signal from the rest of the cell components, which could also increase the signal to noise ratio up to measurable levels.

In summary, this technique allows us to study the different nanolayers inde-

pendently and simultaneously, which is hardly feasible with ellipsometry. It can also provide as much as twice the Raman signal intensity with respect to standard spontaneous Raman microscopy.

4.4 Conclusion

To summarize, we have investigated how the thickness of a nanolayer affects the Raman contrast and the detection visibility of our 4π microscope. In general, thicker layers yield a smaller Raman contrast, which is linked to a lower resolution. However, nanolayers of high refractive index materials, such as the silicon membrane studied in this chapter, behave differently. The Raman contrast in high index layers exhibit periodic cavity-like resonances and anti-resonances for different layer thicknesses, which means that a relatively thick layer can still produce a high Raman contrast.

Additionally, we have demonstrated 4π Raman microscopy for the characterization of nanolayer stacks. We could enhance the Raman signal of the stack by a factor of 1.41 compared to standard confocal microscopy and at the same time obtained 6 nm super-resolution in terms of optical length. Compared to other methods to study nanolayers, such as non-spectroscopic ellipsometry, ours has the fundamental advantage of being suited to simultaneously characterize several layers. This stems from the independent and isolated Raman fingerprint of the nanolayers.

The super-resolution technique described is a tool to measure the optical thickness and position of multiple layers within a layer stack with deep sub-wavelength accuracy. To convert the optical thickness to a physical thickness we would need to know, at least, the refractive index between the nanolayers of interest. To be more precise, we would need the refractive index of all the layers and consider the reflections between them. As in similar studies [108], we could obtain the needed refractive indices, as well as the thicknesses, from our optical length data by measuring the sample under various angles of incidence or different pump wavelengths. Once we know the refractive indices, we could consider the effect of multiple reflections using the transfer matrix method in Appendix A.

Additionally, local sub-micrometer changes in the material structure can also be detected from diffraction limited areas since they are reflected on the Raman fingerprint. We therefore expect 4π Raman microscopy to be advantageous—in terms of signal collection and resolution—for thin-film characterization, biochemical imaging studies, material sciences and artwork conservation efforts, among others.

Our efforts to study biological nanolayers, namely cell membranes, were in-

conclusive due to their weak Raman signal. We have discussed how Raman tags and coherent Raman techniques, as opposed to the spontaneous Raman used in our experiments, could help increase the signal strength.

5

Imaging of Biological Samples

This chapter focuses on the imaging capabilities of our 4π Raman microscope. First, nanoparticles serve to characterize the microscope's point spread function and resolution. We then discuss the 4π Raman images obtained from biological samples and the current limitations of the system.

| | |
|--|-------------|
| 5.1 Introduction | 5-1 |
| 5.2 Point spread function characterization | 5-2 |
| 5.3 4π Raman Imaging of HeLa cells | 5-6 |
| 5.4 Conclusion | 5-12 |

5.1 Introduction

The most interesting application of 4π microscopy is most certainly the study of biological samples, such as bacteria and cells. The hope is that the enhanced resolution of this technique could help biologist unravel some of the many questions around cell processes. With that goal in mind, Raman spectra from different parts of the sample are needed—the context is everything. Obtaining many Raman spectra from multiple cell components and possibly from the whole cell is key to answering questions like: how do inner cell components change shape, distribution

and composition during sickness? why? The power of imaging over single-point spectroscopy lies on its potential to answering these questions.

Before studying biological samples, it is of utmost importance to characterize the microscope itself. The point spread function (PSF), resolution, maximum Raman contrast, as well as the limitations of the microscope, are all indicators of its performance. They can be used to compare the microscope to others and give an idea of what we can expect from it. However, the complex shapes, composition and inner structures of biological samples make them unsuited to characterize any features of the system itself. The sample morphology is unknown, so it would be very difficult to give any measure of quality from the resulting images if we don't know how they should look like. For this reason, it is common practice to employ simple samples with known sizes and compositions that can better showcase specific features of the system.

In this chapter we first characterize the system's point spread function in terms of contrast and resolution using polystyrene nanoparticles. Only then can we discuss the 4π Raman images obtained from HeLa cells, and the current limitations of the microscope for imaging applications.

5.2 Point spread function characterization

In practice, to experimentally obtain the point spread function of an optical system, an object much smaller than the wavelength is scanned through the focal spot. Here we first show some experiments with polystyrene nanobeads. We pay special attention to the axial cross-section of the point spread function because that is where we expect a significant resolution improvement compared to a standard confocal microscope.

Nanoparticles with a diameter in the order of few tens of nanometers are often employed for the characterization of the point spread function. Ideally, the particles should be as small as possible to probe the point spread function without altering it. Fluorescent nanoparticles are ordinarily employed to characterize fluorescence microscopy modalities and we follow the same idea to characterize the Raman point spread function but using Raman active nanoparticles instead. However, the weakness of the Raman signal, many orders of magnitude smaller than fluorescence, poses extra challenges. The fluorescent signal from these small nanoparticles can be strong enough to be seen with bare eyes in a wide-field microscope. In the Raman case, point-by-point scanning and integration times in the order of tens of seconds or longer are necessary.

The factor limiting the feasibility of this experiment is the strength of the nanoparticles' Raman signal, which is ultimately given by the particle size. Obviously, the smaller the particles the more practical challenges we encounter doing the measurements. A routine alignment to find the proper confocal plane using the bright field visible image becomes challenging due to the weak scattering of the small particles. We tried particles as small as 100 nm, but we could only obtain the Raman signal from what we believe were conglomerates, not from single particles. It is challenging to distinguish single particles from conglomerations of few particles when they are that small. An indication of conglomerates is an unusually large Raman signal. The Raman fingerprint looks the same in both cases, except for the higher Raman counts.

Figure 5.1(a) shows a reflection bright field image of 250 nm diameter polystyrene particles employed for this experiment under a Zeiss EC Epipla-Neofluar 100x 0.9NA inf/0 objective lens in air. The corresponding spectrum is shown in Fig. 5.1(b), where the CaF₂ substrate (1 mm thick) and the polystyrene Raman fingerprints are labeled.

The nominal phase is anchored to the slide surface, meaning that we cannot characterize the PSF just by scanning the nanoparticle through the confocal volume. In order to plot the 4π PSF we need to simulate the case where the PSF remains unaltered. It should be as though the nominal phase would not be anchored to the surface of the slide. For this reason we need to purposely introduce a phase shift ξ that depends on the axial position of the nanoparticle z . Namely, for an axial position z , we must add the following phase shift:

$$\xi(z) = -\frac{2\pi}{\lambda/2}z \quad (5.1)$$

where $\lambda/2$ is the assumed period or distance between the intensity fringes.

We obtained four Raman spectra at each axial position of the sample, each for a different nominal phase. We then recover a sinusoidal curve for the main Raman polystyrene peak at 1008 cm^{-1} , which will have a certain phase ψ , amplitude A , and offset O_f . This fitting allows us to determine the Raman signal at any desired nominal phase, meaning that we can apply the phase compensation in Eq. 5.1 in a post-processing step by calculating the compensated Raman intensity R_c :

$$R_c = O_f + A \cos(\psi + \xi) \quad (5.2)$$

The standard confocal PSF for top and bottom excitations, and the 4π point spread functions in the axial direction are plotted in Fig. 5.2(a). The 4π data is the result of the aforementioned compensation R_c , done in post-processing. The

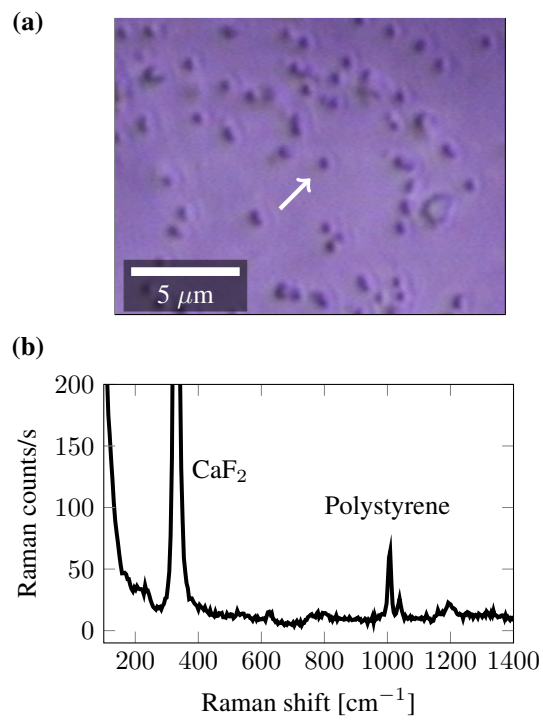


Figure 5.1: Polystyrene nanoparticles with a diameter of 250 nm employed to characterize the 4π PSF. (a) Bright field visible image of the nanoparticles in reflection. (b) Single nanoparticle spectrum obtained with a Zeiss 100x0.9NA objective and 7 seconds integration time.

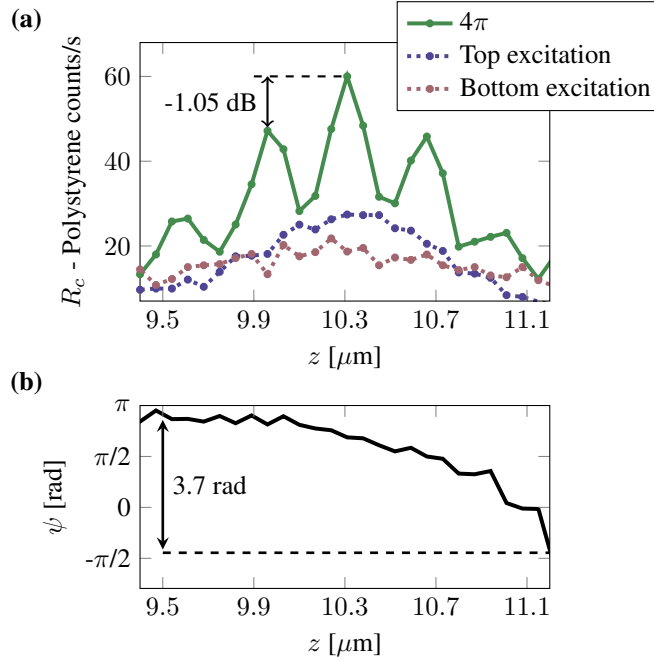


Figure 5.2: (a) Axial point spread function of the standard confocal and the 4π microscopes obtained from a 250 diameter polystyrene nanoparticle. The side lobe suppression is 1.05 dB, i.e., the secondary lobes are 78.6% as intense as the main lobe. (b) Phase ψ obtained from the sinusoidal fitting explained in the text.

intensity of the top and bottom excitation was kept the same for the standard and 4π curves. Note that the Raman signal is always collected from the top side. The characteristic secondary lobes of 4π microscopy can be seen, accounting for 78.6% of the main lobe counts, which is too high to attempt any deconvolution of the data. The top and bottom intensities are not the same across the axial direction z because objectives with different NAs were employed, which can partially explain the non-ideal Raman contrast. The objectives employed for this experiment were a Zeiss EC Epiplan-Neofluar 100x0.9NA inf/0 and a Nikon Plan Fluor DIC 20x0.5NA, for the top and bottom sides of the microscope, respectively.

Using the same high NA objectives on both sides of the sample would be a relatively simple way to decrease the secondary lobes contribution, but only if a thinner substrate is used. We could not implement this idea, however, because the alignment between objectives becomes very sensitive to the thermal drift of the sample and objective piezo stages.

Figure 5.2(b) illustrates the phase shift obtained from the sinusoidal fitting

ψ at each axial position z . It can be seen that it remains relatively constant as expected since it is anchored to the substrate interface, except that there is a certain dependence with the sample position above $z = 10 \mu\text{m}$. This change of 3.7 radians could be due to drifts of the stages, or due to different aberrations in the system when the beam is focused right above the substrate interface or some distance above it. The defocusing of the reflected light on the collection fiber, as well as the Gouy phase (an increase in the apparent wavelength near the waist of a focused beam) could explain the unexpected phase shift, but further work is necessary to clarify the origin of this mismatch.

In order to have the same conditions as the following biological experiments, we tried to measure the beads in water. The main issue, however, is that we could not find them due to the much lower contrast between water and polystyrene.

5.3 4π Raman Imaging of HeLa cells

In this section, the 4π Raman images of HeLa cells are discussed. The cells were fixed for 10 min with 4% formaldehyde (4078-9001, Klinipath) and washed 3 times with Hanks' Balanced Salt Solution (HBSS, 14025050, ThermoFisher). In-plane as well as cross-section 4π Raman images of the cells are compared to standard spontaneous Raman microscopy images. The aim is to demonstrate the axial resolution enhancement of 4π Raman microscopy in a realistic biological experiment. We image small features within the cells to try to mimic the results obtained previously with the polystyrene nanoparticles bearing in mind that biological samples pose additional practical challenges.

Figure 5.3 shows a comparison between standard and 4π Raman images of the same part of a HeLa cell in the xy transversal plane. The objectives used for these experiments were the Zeiss, Water immersion Plan-Apochromat M27 63x/1.0NA on the top part; and the Nikon, Plan Fluor DIC 20x/0.5NA on the bottom part. As the sample is immersed in water, the partial reflector was used.

The images were obtained in a subsequent manner. First the 4π data were recorded, and then the standard confocal image. Drifts of the piezo stages between scans hinder an exact one-to-one comparison between data sets since the images seem to be taken from slightly different confocal planes. The sample could have also changed slightly during the measurements. Simultaneous imaging with the standard and 4π modalities is currently not possible with our setup but, we could find a way to automatically block and unblock the bottom excitation to obtain both data sets before moving the stages to the next pixel position. This would attain a pixel-to-pixel comparison instead of taking a whole 4π image and subsequently the

standard image. The 4π and standard images currently take almost 17 hours, and 2 hours 40 minutes, respectively.

As we did before in Chapter 4, a different approach to be able to compare both images without stage drifts would be to extract the conventional image from the 4π data by averaging the phase shifted measurements for every pixel. The alternative approach would keep exactly the same excitation power, sample position, polarization, etc., but here we focus on the most compelling comparison possible by not obtaining the standard image from the 4π data.

To obtain the standard images we simply block the bottom beam, so the higher intensity of the 4π images is due to the higher pump power hitting the sample. Regarding the Raman peaks, we focus on a peak representative of proteins (1008 cm^{-1}) and another one typically indicative of nucleic acids, proteins and lipids (1458 cm^{-1}).

Figure 5.4 shows a similar comparison between standard and 4π images of a small organelle within a HeLa cell but this time for the xz crosssectional plane, which is where the strongest resolution enhancement is expected. We implemented the linear phase compensation that accounts for the sample axial position and yet the images do not seem to reveal any resolution improvement.

The pixel indicated with an arrow in the last image of Fig. 5.4 and in Fig. 5.5(a) is treated separately in Fig. 5.5(b) and (c) to understand why no resolution improvement can be seen. Figure 5.5(a) shows the Raman contrast of the 1448 cm^{-1} peak. As previously explained, the Raman contrast should ideally be close to 1, but we get a weak Raman contrast smaller than 0.03. In Fig. 5.5(b) the spectra of the pixel corresponding to the small cell organelle for different nominal phases is plotted, and in (c) we fit the experimental data to a sinusoidal curve. These results clearly show the lack of Raman contrast leading to an unreliable phase of the sinusoidal fitting. In fact, the contrast obtained from the organelle is the same as the surrounding medium and similar to the part without cell. We attribute this lack of contrast to the spherical aberrations induced by the substrate and to the different beam intensities hitting the sample from the top and bottom. However, the most important factor is probably the presence of the secondary lobes. In 4π fluorescence microscopy two-photon excitation is typically employed to remove the secondary lobes of the 4π PSF that might conceal the resolution enhancement. On top of that, deconvolution of the image with the PSF helps to further remove the resulting artifacts. Therefore, the need of a similar approach to remove the secondary lobes in our 4π microscope becomes clear.

In [2], the authors show that axially scanning a steep edge of a fluorescent material must show specific signs when measured under a 4π microscope different

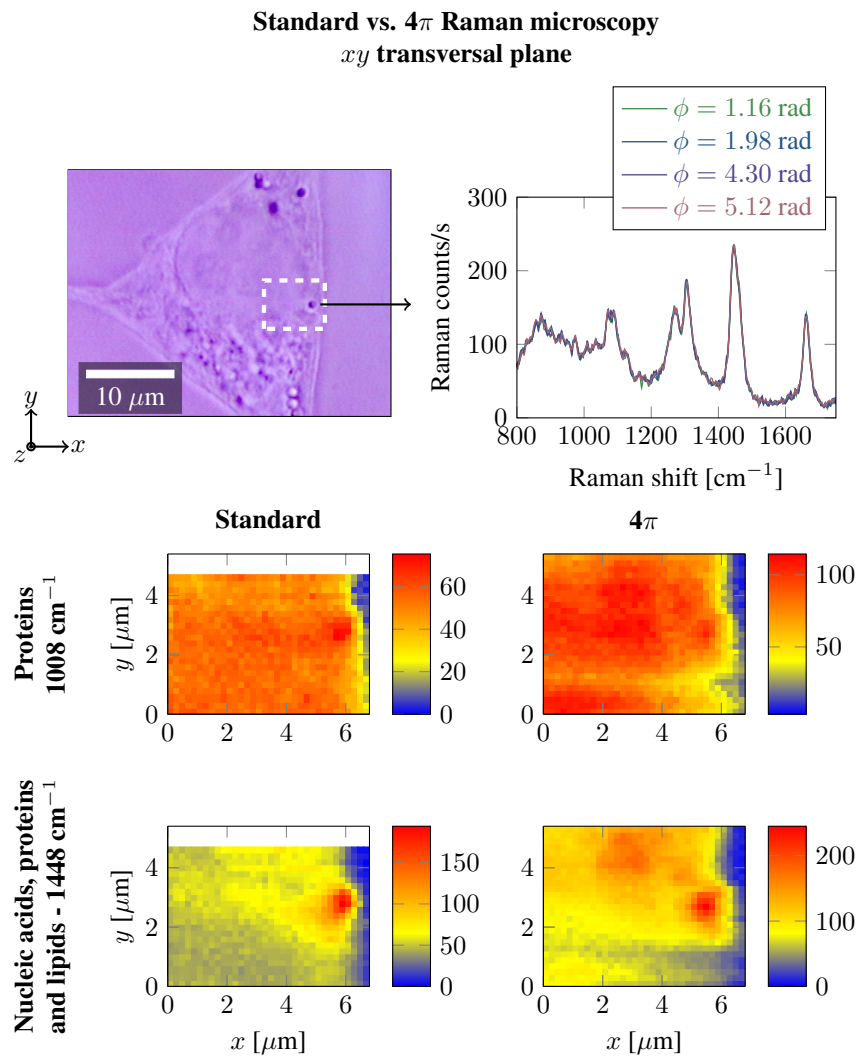


Figure 5.3: On the top left, a bright field image of the sample is shown, where the scan area has been marked. On the top right, spectra for different nominal phases from the rounded small shape are shown. The four spectra overlap, which show no Raman contrast. Below, standard and 4π image of the xy transversal plane of a HeLa cell are shown, taken at approximately $3 \mu\text{m}$ above the substrate interface. The data is obtained from the part of the cell indicated with a dashed rectangle. The colorbar has units of Raman counts per second.

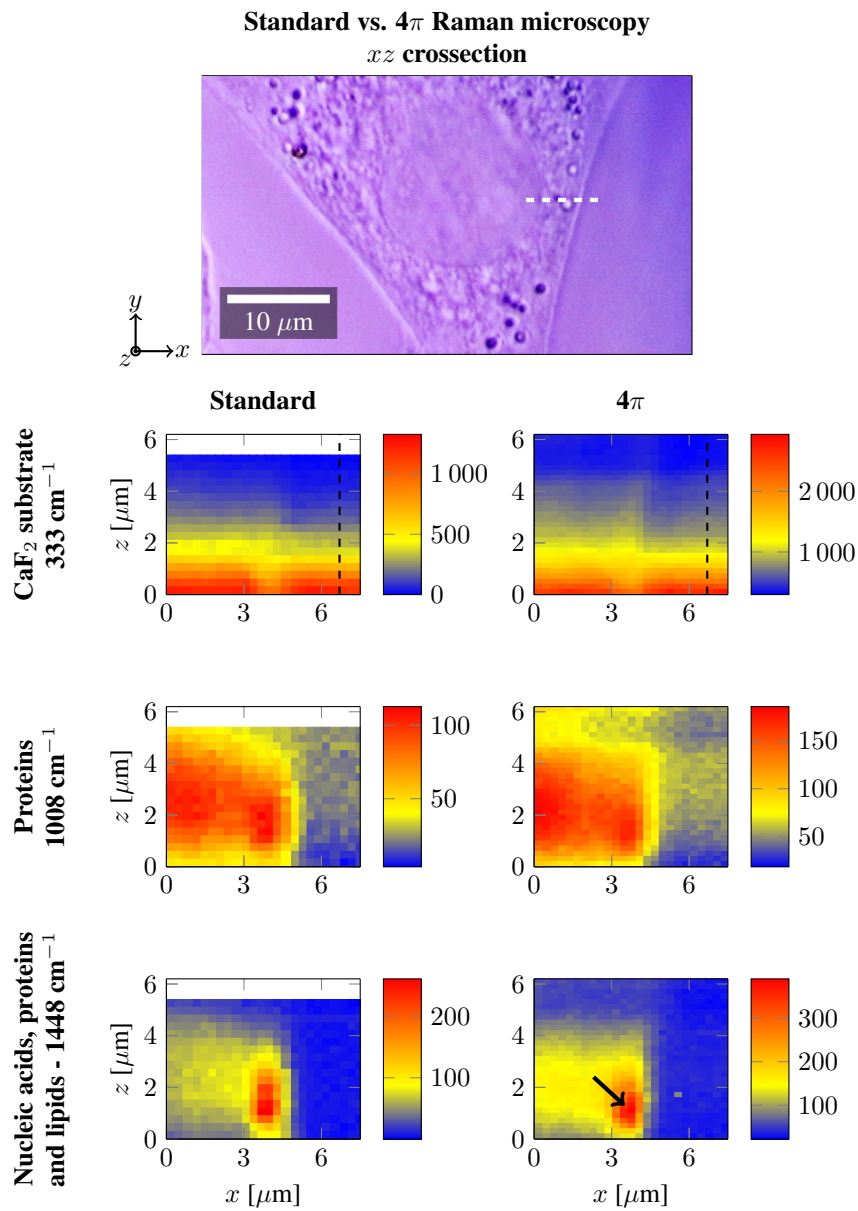


Figure 5.4: On the top, a bright field image of the sample is shown, where the scan area has been marked. Standard and 4π image of the *xz* crosssectional plane of a HeLa cell. The data is obtained from the part of the cell indicated with a dashed white line. The colorbar has units of Raman counts per second.

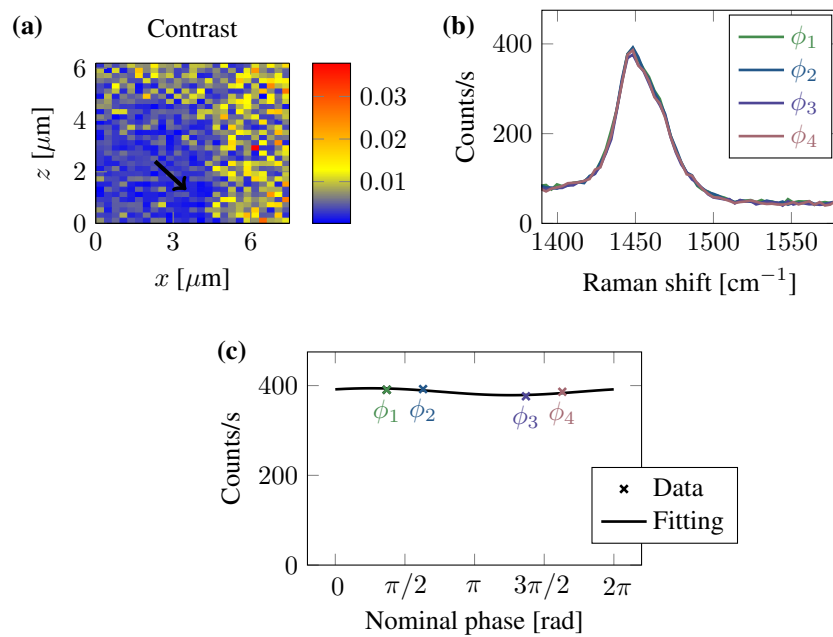


Figure 5.5: A weak Raman contrast is obtained in the measured area of the HeLa cell. (a) Raman contrast of the cell at the 1448 cm^{-1} peak in the xz plane. (b) Spectra of the pixel indicated with an arrow for different nominal phases ϕ_i . (c) Sinusoidal fitting of the data.

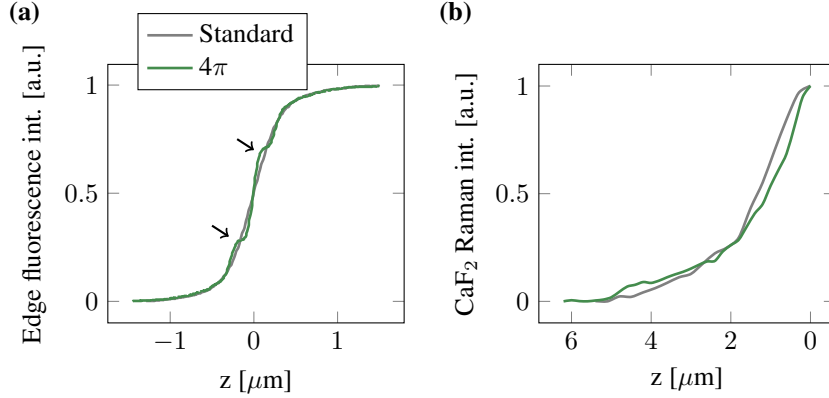


Figure 5.6: Standard and 4π type-A microscopy axial scan of an edge. (a) Theoretical standard and 4π type-A fluorescence response adapted from [2]. Oil immersion 1.4NA objective lenses were used. The excitation wavelength used was 633 nm and the emission wavelength was 725 nm. Two bumps corresponding to the different lobes of the PSF can be seen. (b) Standard and 4π Raman microscopy of the CaF_2 peak at 333 cm^{-1} . No clear bumps corresponding to the secondary lobes can be distinguished compared to the standard response.

to a standard confocal microscope. Theoretically, the fluorescent signal obtained with a 4π type A microscope shows a stepped increase of the fluorescence signal compared to the smooth standard response, as shown in Fig. 5.6(a). The steps correspond to the different lobes of the PSF starting to overlap with the fluorescent material. We can plot the experimental axial scans marked in Fig. 5.4 with vertical dashed lines in the Raman images of the CaF_2 substrate at 333 cm^{-1} . The results plotted in Fig. 5.6(b) have no clear bumps in the 4π response with respect to the standard response. Again, this is probably because our 4π Raman microscope presents stronger secondary lobes and a higher number of them than the ideal theoretical PSF used in Fig. 5.6(a). Yet, we could expect to see a higher number of smaller bumps in our response, but the signal-to-noise ratio would need to be much higher than in this results.

Additional limitations derived from the long times required to obtain this kind of images were also present. Drifting of the stages is a particularly relevant issue. Figure 5.7 shows the time variation of the Raman signal obtained from a thick non-transparent silicon substrate, revealing a 10% intensity drop in 3 minutes due to thermal variations. In this experiment, we directly connected the laser output to the top part of the microscope to remove the drift contribution of most of the stages. We only excited the sample from the top side of the microscope with the Zeiss EC Epipla-Neofluar 100x0.9NA objective. The only stages whose drift can contribute to the plot in the figure are the top z-stage of the microscope and the sample stage.

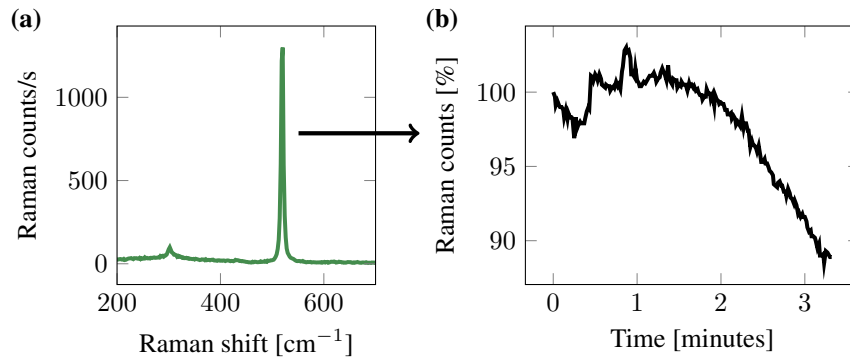


Figure 5.7: (a) Raman scattering spectrum of Silicon and (b) evolution of its Raman peak at 521.08 cm^{-1} due to the drift of the Z stage of the microscope and the sample stage.

Note that during the biological experiments the thermal drift is probably worse during the first minutes as the sample is excited from both sides, so the stage of the bottom objective and the partial reflector can also drift. However, after approximately the first half an hour, the system is expected to be more thermally stable, as we left the room and the experiment continued thanks to the automated setup. A better thermal isolation and building a more compact setup by enclosing the interferometer within the microscope stand could be feasible solutions.

We also tried to image other biological samples, namely *Caenorhabditis elegans* worms, spores, plant seeds and HeLa cells in dry state. The aim was to measure thin layered features resembling the nanolayer stack studied in Chapter 4, from which we could obtain a stronger Raman contrast in spite of the secondary lobes. Depending on the kind of sample employed, different challenges arose. For instance, the worms were being dragged by optical forces exerted by the pump beams. With the spores and seeds the challenge was that, like many other plant samples, they strongly absorb the pump energy, making it difficult to access the same spot from both sides of the sample and also prone to burning effects. As a general remark for all these samples, we could not clearly distinguish the characteristic Raman fingerprint of any thin features from the rest of the Raman spectrum. The images of the HeLa cells shown here were the most relevant and clear results obtained at the time of writing this dissertation.

5.4 Conclusion

We have characterized the point spread function of the 4π Raman microscope in the axial direction using a polystyrene nanoparticle. The diameter of the particle

employed was 250 nm, which is slightly big for this experiment. Experiments with smaller particles could not be carried out due to their extremely weak Raman signal.

Regarding the imaging experiments of biological samples, the Raman contrast obtained so far was insufficient, and we think that it can be explained mainly by the presence of the secondary lobes and the complexity of the sample itself. This meant that a direct proof of axial resolution enhancement in a biological setting could not be obtained yet. We tried imaging thin layered biological samples hoping to obtain a stronger Raman contrast, just like we did before with a nanolayer stack, but distinguishing their Raman fingerprint proved to be quite challenging.

We have also discussed other limitations and challenges involved in the imaging experiments, mainly related to the long acquisition times necessary. Thermally isolating the setup could mitigate some of them, such as the thermal drift of the piezo stages that can reduce the Raman signal detected from the spot of interest and misalign the optical components and the sample.

6

A New Modality for the 4π Raman Microscope: Quantitative Phase

Biological samples that induce a certain phase shift on the excitation beams can aberrate the 4π point spread function. We propose a method that compensates for the sample-induced phase shift and, at the same time, allows us to quantify such a shift, giving rise to 4π Raman and quantitative phase microscopy.

| | | |
|------------|---|-------------|
| 6.1 | Introduction | 6-2 |
| 6.2 | Combining 4π Raman with quantitative phase microscopy | 6-3 |
| 6.2.1 | Solving the 4π phase problem | 6-4 |
| 6.2.2 | Principle of sample-induced quantitative phase retrieval | 6-6 |
| 6.2.3 | State of the art of quantitative phase microscopy | 6-8 |
| 6.2.4 | Phase calibration for quantitative measurements | 6-9 |
| 6.2.5 | 4π Raman and quantitative phase microscopy on HeLa cells | 6-11 |
| 6.3 | Conclusions | 6-14 |

6.1 Introduction

In 4π fluorescence microscopy, once the sample is in place and the beams are properly phase shifted to obtain constructive interference, it is typically assumed that the sample position has no influence over the phase shift [48]. The field of view has to be kept small enough to comply with that assumption.

The point spread function of any microscope can be affected by the sample itself in three main ways: through scattering, absorption and optically delaying the excitation beams. Biological samples such as cells and bacteria are commonly referred to as weak scattering objects, as though scattering were the only relevant factor to obtain high quality images. However, the stability of the phase between beams in 4π microscopy over the entire field of view can be easily overestimated. Even a relatively small phase shift of a quarter of the wavelength can completely change the point spread function of a multi-beam microscope. In 4π microscopy, whether it is based on fluorescence or Raman processes, setting the phase shift between counter-propagating beams to interfere constructively across the imaging plane is not a trivial task. Yet, it is vital, for instance, for an accurate image deconvolution.

Our 4π microscope can solve the phase problem because it is sensitive to the phase shift between the pump beams at the sample plane. Not only can it remove the environmental phase fluctuations, but it can also isolate the phase shift originated by the sample from the phase variations, giving rise to Quantitative Phase Microscopy (QPM).

Retrieving the sample phase information, in addition to the Raman signal, offers clear benefits. Raman spectroscopy probes the chemical composition of biological samples with sub-micron resolution, rendering it a powerful tool in the diagnosis of several diseases and to study unstained biological samples. However, the weak Raman signal leads to long acquisition times, unsuited to study dynamical processes or large samples. Quantitative phase microscopy can speed up the diagnosis, provide complementary data and potentially link the Raman fingerprint of the sample with corresponding refractive indices. Here we demonstrate a 4π microscope that records both, the Raman and quantitative phase information, from the same sample spot.

6.2 Combining 4π Raman with quantitative phase microscopy

Illnesses can present themselves in many different forms. Changes in the morphology, chemical composition and biophysical parameters, such as matter density and cell dry mass, provide different windows through which the illnesses can be understood and diagnosed [38–41, 109].

The chemical composition of the sample can be probed by Raman spectroscopy in a noninvasive way and without the need of extrinsic labels. In the biomedical field, Raman spectroscopy has already been employed to diagnose cancer [38, 39], monitor blood glucose [40], differentiate cell lines [41] and sub-compartments [18], and many other applications.

To monitor morphology and biophysical parameters, such as matter density and cell dry mass, QPM can be employed. It has been used in the diagnosis of cancer [109] and in cell pathology studies [110–113].

These two techniques, Raman and QPM, have been used before to complement other microscopy techniques, for instance, Raman spectroscopy has been combined with fluorescence microscopy [114] and optical coherence tomography [115]. They have also been combined together. In [116, 117] QPM preselects red blood cells potentially infected by malaria to be carefully examined with Raman spectroscopy. A typical diagnosis would be based on a slow Raman scan across the whole sample, but using full-field QPM makes the diagnosis orders of magnitude faster while maintaining the necessary specificity to diagnose malaria. In [118] the authors make an extended study of the relationship between ultraviolet exposure and skin cancer using both modalities, QPM and Raman spectroscopy.

In the aforementioned works, a completely different setup for each modality was used [118], a different optical path [116, 117] or even a different wavelength [119, 120]. This explains the need for algorithms to match the different magnifications, field of views, translations, rotations and dispersion effects of both images. Moreover, different aberrations and resolutions are completely disregarded.

In this work we propose a microscope with two complementary modalities— 4π Raman and Quantitative Phase Microscopy—to study cell processes from two different points of view simultaneously. It uses a common-path point-scanning approach for both modalities where the same laser beam serves two purposes: Raman pump and probe for the quantitative phase measurement. Consequently, we obtain an inherent match between data sets. The data are taken from the same sample spot without the need of any post-processing to match both images. Note that the aberrations and resolutions, however, are not exactly the same for both

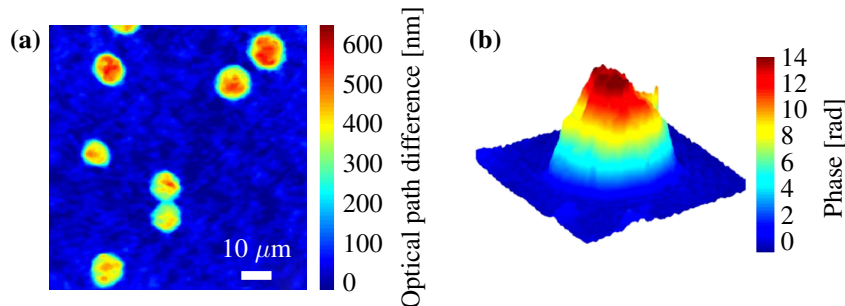


Figure 6.1: Biological samples can induce strong phase shifts. (a) Breast cancer cells inducing a phase shift of 600 nm at a wavelength of 632 nm. Adapted from [121]. (b) HeLa cell inducing up to 14 radians during osmolarity experiments with a 809 nm source. Adapted from [122].

modalities, as their PSFs are different.

Importantly, the quantitative phase obtained is free of any phase wrapping constraints in a dynamic range of more than 130 radians while being compatible with the Raman modality of the microscope. This microscope allows correlating the Raman and quantitative phase information [119] from the same spot of a HeLa cell, which has the potential to become a new tool in the diagnosis of disease.

The quantitative phase method proposed here is tied to the 4π phase problem introduced in Chapter 2, i.e., the precise control of the position of the multibeam fringe pattern. Being able to measure the phase shift between beams is what allows us to solve it. We can keep the nominal phase fixed while scanning the sample and, as the source of the phase shift is actually the sample, the same scheme gives us quantitative access to the phase shift induced by the sample. We further discuss the proposed method to address the 4π phase problem in the following section, then we proceed to explain the QPM technique and to show the experimental results obtained with it.

6.2.1 Solving the 4π phase problem

Several of studies in the literature show that biological samples can induce strong phase shifts. For instance, in [121] breast cancer cells induce an optical path difference of 600 nm at a wavelength of 632 nm, and in [122] HeLa cells induce a phase shift of up to 14 radians in experiments with an 809 nm source. Both cases are shown in Fig. 6.1. These are indications that the phase shift in commonly studied cells cannot be neglected, and considering it in the measurements is still an

open challenge in the field of microscopy.

Figure 6.2(a) illustrates the optimum point spread function of the microscope, where the counter-propagating beams are focused constructively. In a horizontal scan, as soon as the focus hits the cell, the point spread function will be significantly changed as shown in Fig. 6.2(b). Therefore, instead of constructive interference at the plane to be imaged we might get destructive interference, and this is only for a $\pi/2$ phase shift. We have seen that phase shifts can be larger in typical biological samples. In order to avoid image distortions, as well as to be able to apply an image deconvolution for secondary lobes removal, the PSF must be translationally invariant and independent of the sample position.

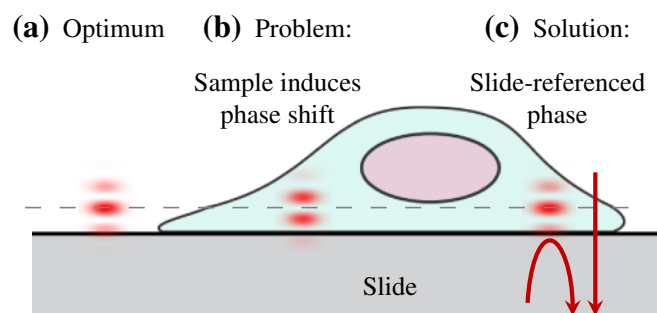


Figure 6.2: (a) Optimum PSF with constructive interference at the center. (b) The presence of a cell affects the 4π point spread function. (c) This can be solved when the slide interface is used as the phase reference. The interference between a transmitted beam and a reflected beam, indicated by arrows, allows measuring the phase state at that interface. The dashed line indicates where the main peak should be for constructive interference at the center. Drawings are approximately to scale, where the cell width is $\sim 20 \mu\text{m}$ and the main peak of the point spread function is $\sim 0.4 \mu\text{m}$.

In this context, we wanted to explore the possibility to actively compensate for the phase shift induced by the sample. We discussed in Chapter 2 the different approaches that other authors have taken to approach this issue, such as using planar or point-like features within the sample as nominal phase probes [54, 55], but we propose a different approach here. We use the reflection from the interface between slide and sample as a reference for the phase shift between beams, as depicted in Fig. 6.2(c). This technique requires the reflection from the slide interface, so it will only perform properly when the reflecting interface lies within the focal spot where it can be collected. This means it can only measure parts of the sample closest to the interface. If we want to measure elsewhere or the reflection is too weak, we can also employ an external reflector as the phase reference.

The goal is to keep the PSF stable by anchoring the nominal phase to the slide surface. To do so, the system compensates for the phase fluctuations due to

environmental changes, but also for the phase shift induced by the sample. These two sources of phase variations are indistinguishable from each other from the point of view of phase shift compensation, but as we are about to discuss, we can remove the environmental phase fluctuations by time averaging.

6.2.2 Principle of sample-induced quantitative phase retrieval

A close up of the Raman and quantitative phase microscope is shown in Fig. 6.3. The Raman signal spectrum is measured by the spectrometer, and the phase signal by the photodetector. The beam from a 785 nm laser is split into two paths, one connected to the top part of a Raman microscope, and the other to the bottom thereof. These beams are travelling in opposite directions to interfere at the sample plane, forming the 4π point spread function which acts as the Raman pump. The top beam and a partial reflection from the bottom beam, both indicated by red arrows, undergo a phase shift ϕ_T and ϕ_R , respectively. The sample introduces an additional optical length ϕ_{sample} also present in the photodetector signal $\cos(\phi_T + \phi_{\text{sample}} - \phi_R - \phi_f)$.

For the stable regime, the feedback loop is turned on to stabilize the system at the chosen nominal phase. For the following calibration experiments, the specific phase value is not relevant, but it will be for the experiments with cells shown later. The role of the feedback loop is to drive the phase shifter in such a way that its input, the detector signal, is kept fixed at the desired nominal phase. It does so by driving the translation stage, referenced to as *phase shifter*, that moves one of the collimating lenses to change the optical length in one of the interferometer arms.

It is noteworthy that we do not access the phase shift induced by the sample in a conventional way, relying on the cosine term of an interferogram. Any change of the phase shift at the sample plane can be traced back in the form of the voltage U driving the phase shifter,

$$U = \frac{1}{C} (\phi_T + \phi_{\text{sample}} - \phi_R - \phi_f) \quad (6.1)$$

where ϕ_f is the phase shift induced by the phase shifter necessary to keep the system stable and C is the calibration coefficient that we will determine experimentally with units of radians per volt. We can set the value $\phi_T - \phi_R$ as our zero phase reference. Once the environmental phase fluctuations are averaged out by taking N number of measurements, the driving voltage U is directly proportional to ϕ_{sample} as the loop ensures that any change on ϕ_{sample} will be compensated by changing ϕ_f . There is no sinusoidal term involved in the measurement and, hence, the phase values obtained in this manner are unaffected by phase wrapping. As a linear measurement, averaging N samples reduces the standard deviation of the noise by a factor \sqrt{N} .

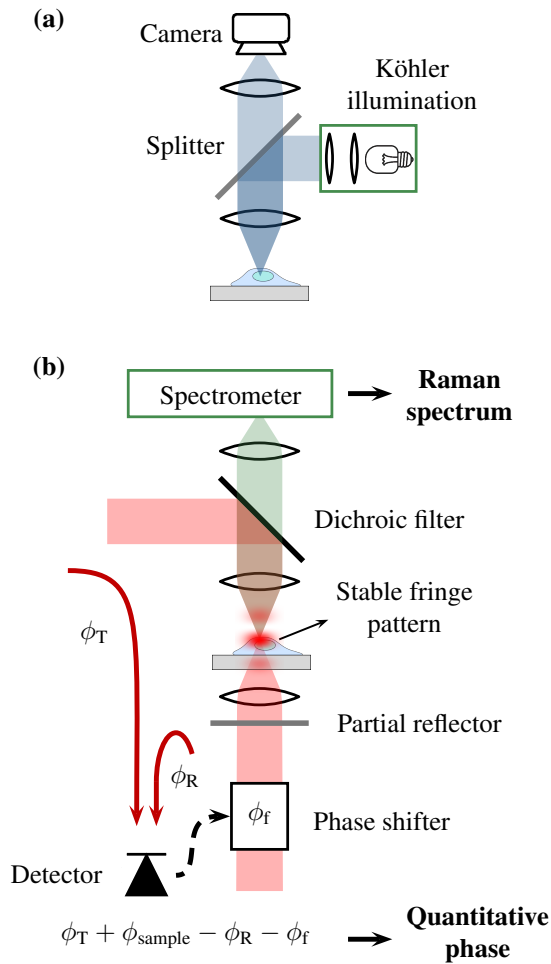


Figure 6.3: (a) Reflection bright field mode of the microscope. (b) Schematic of the quantitative phase and Raman modes of the 4π microscope. The optical path length from the beamsplitter of the interferometer to the partial reflector is indicated as ϕ_T and ϕ_R , for the transmitted and reflected beams respectively. The red arrows indicate the beams that will interfere at the detector to produce a term $\cos(\phi_T + \phi_{\text{sample}} - \phi_R - \phi_f)$ that also depends on the phase shift induced by the sample ϕ_{sample} and by the phase shifter ϕ_f . The Raman spectra are obtained with the spectrometer and the quantitative phase by the detector and a feedback loop represented by the dashed arrow.

To isolate ϕ_{sample} from the detector signal, in the experiments of the following sections we will remove the environmental low-frequency phase fluctuations in the system. We will do so by taking 25 measurements and averaging them, which sets the phase scanning time.

6.2.3 State of the art of quantitative phase microscopy

Note that our QPM is not exactly a 4π approach, as only of the measured beams goes through the sample. Yet, to our knowledge, this is the first time that a 4π microscope has been used for quantitative phase measurements. However, it is not so straightforward to search for non- 4π quantitative phase methods in the vast scientific literature on this topic. The diversity of phase imaging techniques has boomed since the surge of *phase contrast microscopy* in the 1930s, although quantitative phase imaging methods only became widespread after digital holography and inexpensive detector arrays were developed. Most of the QPM techniques differ to ours in the sense that they are full-field approaches, i.e., they acquire the entire image in one shot, whereas our approach is a single-point scanning technique.

The most similar scanning technique we could find was published in 2008, where the authors claim it is a novel technique to remove the 2π phase ambiguities [123]. The method described, illustrated in Fig. 6.4, shares many similarities with our scanning method. Besides the removal of the 2π ambiguities and phase wrapping issues, it does not require a dedicated laser or optics. It operates with reflections (top R_t and bottom R_b) to stabilize the phase between beams as it also suffers from thermal fluctuations originated in the optical fibers indicated by continuous red lines. Free-space propagating beams are indicated by dashed lines.

A fundamental difference is that it is a near-field microscope, while ours functions in the far-field. But most of the differences with our approach are derived from the stabilization approach employed, where the phase of one of the beams is modulated and the detected signal expanded as an infinite Bessel function series, which we described in section 3.4.1.4 of Chapter 3. The reflections R_t and R_b , together with a feedback loop involving phase modulator 1 and detector 1, serve to stabilize the thermal phase variations.

The optical setup needs two feedback circuits, the one just described to compensate the thermal fluctuations, and another one to measure the phase induced by the sample without ambiguities. The latter involving phase modulator 2 and detector 2 in Fig. 6.4. A half-wave plate and a quarter-wave plate serve to match the polarization at the output of both arms of the interferometer. To detect the phase induced by the sample, the underpinning idea closely resembles ours—the signal of interest is provided by the compensation signal of a feedback loop.

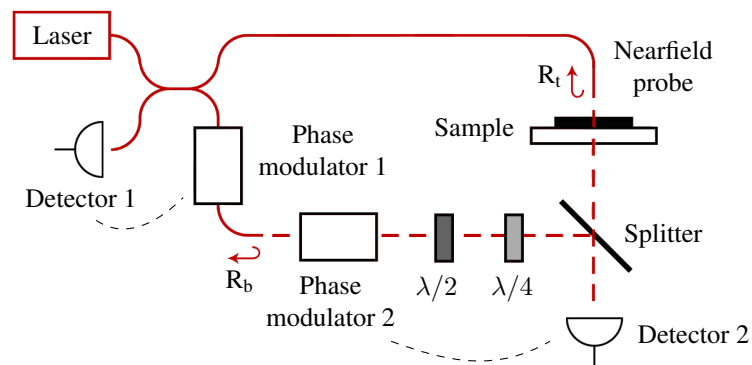


Figure 6.4: Optical schematic adapted from [123], which shares many similarities with ours in terms of phase stabilization. Besides removing the 2π ambiguities and phase wrapping issues, it does not require a dedicated laser or optics to stabilize the phase shift between interferometer arms. It operates with reflections (top R_t and bottom R_b) as it also suffers from thermal fluctuations originated in the optical fibers indicated by continuous red lines. Free-space propagating beams are indicated by dashed red lines. Electric feedback loops are indicated with black dashed lines.

Each of the feedback loops is more complex than ours as they require to modulate the phase, lock-in detection and additional electronic filters. Our approach is then original in terms of simplicity.

For quantitative phase measurements of biological samples the system described here, similarly to ours, requires a calibration step. We describe and implement this process in the following.

6.2.4 Phase calibration for quantitative measurements

The phase shifts measured by the phase modality are quantitative only after a pre-calibration step. The results of this calibration step are depicted in Fig. 6.5. Figure 6.5(a) shows a visible top-view image of the calibration sample, consisting of an ARP (electron beam resist) nanolayer on top of a $120\ \mu\text{m}$ CaF_2 substrate. We selected a Raman grade CaF_2 because of its low fluorescence background. The ARP was etched away after a lithographic process to open a window through which the CaF_2 substrate can be seen. In Fig. 6.5(b) the height of the ARP nanolayer was measured with a profilometer (Dektak), yielding $200 \pm 1\ \text{nm}$.

While scanning the sample with our microscope, we monitor the output voltage of the feedback loop that drives the phase-shifter. In Fig. 6.5(b) we see that $0.18\ \text{V}$

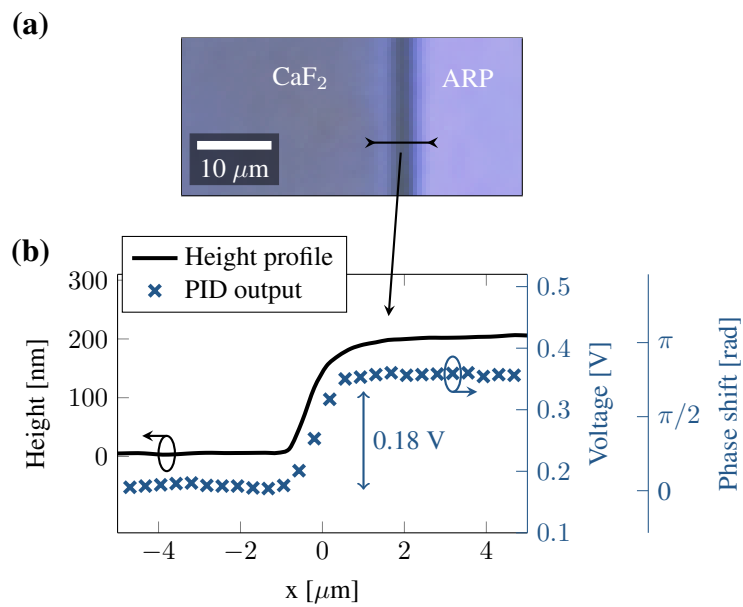


Figure 6.5: Experiment using an ARP nanolayer with an open square window of $150\ \mu\text{m}$ on top of a CaF_2 substrate. (a) Visible image. (b) Nanolayer height obtained with a profilometer and PID output voltage, which is proportional to the phase shift induced by the sample. These data are obtained from the part of the sample indicated in (a) with a black line.

on the phase-shifter compensate the phase shift induced by the ARP layer. The refractive index of the ARP given by the manufacturer is 1.56 at the laser wavelength. For the open window, the reflection happens at the CaF_2 interface. However, the part covered with ARP has two interfaces, air-ARP and ARP- CaF_2 , leading to interference effects that need to be considered. A transfer matrix calculation including these effects yields an extra phase shift of 0.37λ , or equivalently 2.35 radians, compared to the bare substrate. It should be noted that this calculation neglects the entire range of angles given by the objective lenses as it assumes normal incidence.

We conclude that a phase shift of 2.35 radians corresponds to a driving voltage of 0.18 V, leading to the calibration coefficient $C=13.06$ rad/V that we will use to obtain the quantitative phase. Regarding the phase shift dynamic range, the limiting factor is given by the 10 V range of the feedback electronics output, so using the previous coefficient it results in more than 130 rad as long as the phase gradient of the sample are smooth and no sharp steps bigger than 2π are present.

6.2.5 4π Raman and quantitative phase microscopy on HeLa cells

The quantitative phase, as well as the Raman molecular fingerprints, are measured in a confocal manner. This confocality in the QPM modality, although key to obtaining the advantages described above, comes at the price of losing its conventional full-field capability.

We currently obtain the Raman signal and the quantitative phase in subsequent scans. A completely simultaneous scan of both modalities is hindered by the phase fluctuations in the fibers due to environmental factors. The optical fibers play the role of the pinhole, as part of the confocal microscope, but they are not strictly necessary. They connect the interferometer with the commercial microscope stand, but it could be possible to substitute them by actual pinholes. Thus, an approach to speed up the measurements would be to remove the source of phase variations, namely we could remove the fibers, leading to truly simultaneous Raman and QPM of the same spot of the sample.

The results of the Raman and quantitative phase line scans of a fixed HeLa cell are shown in Fig. 6.6(b). The cells were fixed for 10 min with 4% formaldehyde (4078-9001, Klinipath) and washed 3 times with Hanks' Balanced Salt Solution (HBSS, 14025050, ThermoFisher). The commercial microscope stand allows us to easily remove the top dichroic filter and to choose a different optical path to work as a bright-field microscope (white light source and camera shown on the schematic of Fig. 6.3(a)). In order to have a visual aid, a reflection bright-field image of the cell was taken right before the scans on the bottom of the figure. A Raman spectrum

from the nucleus of the cell is shown below the visible image. This spectrum is selected from all the full Raman spectra taken for the scans. The exact spot from which it was obtained is indicated with a green cross in the bright field image and in the corresponding scan. For scan (a), the scan was taken at $0.5 \mu\text{m}$ above the substrate interface. The axial position for scans (b) and (c) was selected at the beginning of the scans such that the Raman signal was highest in the middle thereof, which should be in the order of few microns above the substrate. The 784 cm^{-1} peak corresponds to a DNA band and is chosen for the Raman scans shown on the bottom the figure.

In this proof of principle experiment the speed of a single phase line-scan is limited by the speed at which the software is able to communicate with the piezo stage used to scan the sample. It currently takes 40 seconds to acquire the 70-point scans of biological samples. Connecting a ramp generator directly to the piezo stage would spare the communication with the controller and, therefore, it would increase the measurement speed. A ramp generator is an electronic device that generates a linearly rising or falling voltage with respect to time.

For both modalities, Raman and quantitative phase, we took 70 measurements while scanning the sample in the x direction, where each Raman spectrum took 6 seconds to be acquired. Using the calibration factor obtained with the ARP sample, we additionally obtained the quantitative phase shift induced by different parts of the HeLa cell. The maximum value of $\sim \pi/2$ radians is in agreement with the literature [121, 124], which is reported to be in the order of a few radians for this kind of cells.

The first scan in Fig. 6.6 labeled (a) focuses on a site where there are no cells, only a barely visible particle probably composed of cell debris (indicated with an arrow) of $1.3 \mu\text{m}$ diameter, giving an idea of the microscope sensitivity. Although the particle is masked by the noise in the entire Raman spectrum, a significant bump is detected by the quantitative phase modality.

Two more line scans, (b) and (c), are shown, one of them going through part of the HeLa cell with cytoplasm and small organelles, and the other mostly going through the nucleus. In general, it can be seen that both modalities show a high degree of correlation. This is expected as the presence of a higher number of cell molecules leads to a signal increase in both cases.

Some parts of the scans show differences between the Raman and phase curves, mostly visible at the edge of the cell. The most clear difference, marked with an ellipse, lies on the scan (b) around $x = 4 \mu\text{m}$ and we suspect it is due to edge effects that need further investigation.

Scan (c) shows a slightly more intense Raman signal compared to scan (b),

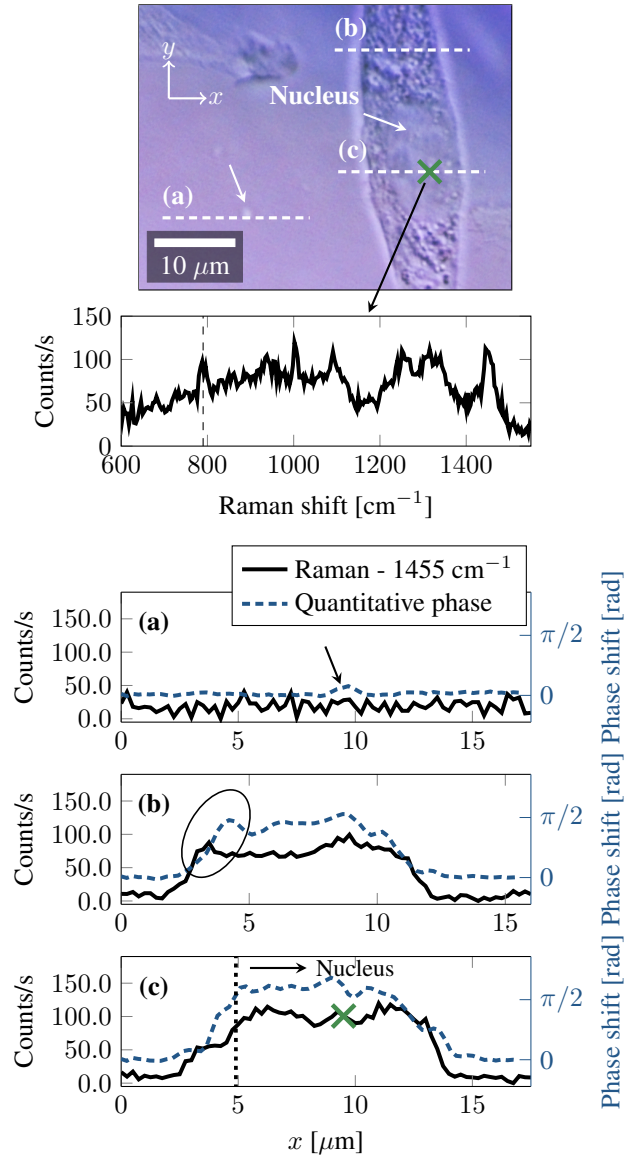


Figure 6.6: Raman and quantitative phase scans of a HeLa cell. On top, reflection bright-field image. Middle, reference Raman spectrum of the cell where the peak of interest at 784 cm^{-1} is indicated with a dashed line. Bottom, Raman and quantitative phase scans of three lines of the sample indicated with dashed white lines on the visible image. The evolution of the 784 cm^{-1} Raman peak in x is plotted in black. The corresponding Raman counts per second are indicated on the left vertical axis. The quantitative phase of the respective scans is indicated with dashed blue curves and are linked to the vertical axis on the right. The ellipse indicates a part of the Raman and QPM scans that greatly differs.

expected from the DNA Raman band analyzed. However, the setup in its current state is prone to stage thermal drifts between scans, which can affect the intensities of the different scans. In order to reduce them we realigned the objective lenses at the beginning of scans (a), (b) and (c). This realignment could be avoided enclosing all the optical components inside the same microscope stand, which would improve the thermal isolation of the setup. The quantitative phase scan is more robust against the misalignment because the substrate is reset as the 0 rad reference for every scan.

Looking at the visible image in Fig. 6.6, there is a small part of cytoplasm at the beginning of scan (c) before it reaches the nucleus of the cell. The quantitative phase information does not show a clear difference between both parts. Conversely, the Raman signal at the selected peak is higher at the cytoplasm part, which can be used to separate both contributions and shows how both modalities can complement each other in a practical application.

6.3 Conclusions

Raman microscopy is a powerful tool in the diagnosis of several diseases and, more in general, to study unstained biological samples. Despite its potential, the slow acquisition of data hinders its applicability in the study of dynamical processes or large sample areas. Here we discussed how a quick quantitative phase microscopy can speed up, substitute or complement the slow molecular Raman imaging process.

In its current state, the speed of the QPM modality is limited by the thermal phase fluctuations that need to be averaged out with several scans of the same spots, and by the communication with the scanning piezo stage. Both are solvable issues. Enclosing all the optics inside the same microscope stand in a compact way could potentially render the phase stabilization unnecessary, although a phase shifter would still be necessary to adjust the phase shift between beams at the sample plane. Regarding the communication with the scanning piezo stage, a ramp generator could be directly connected to it, instead of slowly communicating through a PC. Implementing these setup modifications would mean the QPM speed would only be limited by the sensitivity and speed of the photodetector, potentially reaching speeds for scans like the ones presented here in the order of 100 milliseconds or less, instead of the current ~ 17 minutes.

As a noticeable property, the quantitative phase modality of the proposed microscope is unconventional because it does not rely on the measurement of the sinusoidal term of an interferogram. Therefore, it does not suffer from phase-wrapping issues and does not require to unwrap the phase in a post-processing algorithm. The phase shift of the sample is directly proportional to the experi-

mentally measured voltage, i.e. the feedback voltage, over a 130 radians dynamic range.

The current method could be used to study the correlation between composition of inner structures within living organisms and their refractive index. When the data show a high degree of correlation using solely QPM to diagnose a given disease suffices. It greatly speeds up the process since the Raman measurements pose the speed limiting factor. In the opposite case, the uncorrelated data would show that different molecules within the sample have different refractive indices. In cell studies this will allow estimating the refractive index of the different sub-components from a Raman measurement.

The method explained here enables an accurate control of an optical interference pattern with respect to the sample that is insensitive to any surrounding perturbations. Here we use it to control the phase between excitation beams in a 4π Raman microscope, but it can be extended to other microscopy techniques where the phase between two or more coherent beams is critical, such as 4π fluorescence microscopy, I5M [6, 125–127] or MOM [128]. We hope this method will be useful to obtain more reliable images with unlimited field of views.

To conclude, we demonstrated that the 4π Raman and quantitative phase microscope discussed in this work offers several advantages compared to previous studies in terms of resolution and, most importantly, in terms of the inherent alignment between modalities.

7

Conclusion and Perspectives

| | |
|--|------------|
| 7.1 Conclusion | 7-1 |
| 7.2 Future perspectives | 7-2 |

7.1 Conclusion

The work carried out for this dissertation has led to the first ever 4π Raman microscope. We converted a commercial Raman microscope into a 4π microscope by attaching it to a tailored Michelson interferometer and demonstrated its superior Raman signal collection and resolution compared to a conventional confocal microscope.

The study of a particular sample, a nanolayer stack, concluded that our microscope can yield nanometer-scale super-resolution. This demonstration was not uniquely enabled by the 4π configuration. A conventional microscope could achieve super-resolution by following the same methodology, although the enhanced Raman signal collection and resolution of 4π microscopy provided a precision hardly feasible with other techniques to characterize nanolayer stacks. Additionally, our microscope has the fundamental advantage of being suited to simultaneously characterize several layers thanks to the independent and isolated Raman fingerprint

of the different nanolayers. In this regard, we expect 4π Raman microscopy to become a new tool for thin-film characterization, material sciences and artwork conservation efforts, among others.

The characterization of the point-spread-function of our microscope showed us that the secondary lobes contribute substantially to the image formation and can hinder the effective resolution. These sidelobes are also responsible for the lack of Raman contrast of the biological images and, consequently, a direct proof of axial resolution enhancement in a biological setting could not be obtained yet.

The special phase stabilization developed for this optical setup involves a very simple electronic scheme compared to the state of the art and without a dedicated laser source. It accurately controls the optical interference pattern with respect to the sample and renders it effectively insensitive to any surrounding phase perturbations. Moreover, it allows us to obtain the quantitative phase shift induced by the sample, which complements well the 4π Raman modality of the microscope as it can speed up the diagnosis of diseases where only Raman microscopy was previously used. The quantitative phase modality of the proposed microscope is unconventional because it is a point-scanning technique that does not rely on the measurement of the sinusoidal term of an interferogram. Therefore, it is insensitive to phase-wrapping issues and potentially does not require to unwrap the phase in a post-processing algorithm, as long as the feedback loop stabilization does not suffer 2π radians phase jumps.

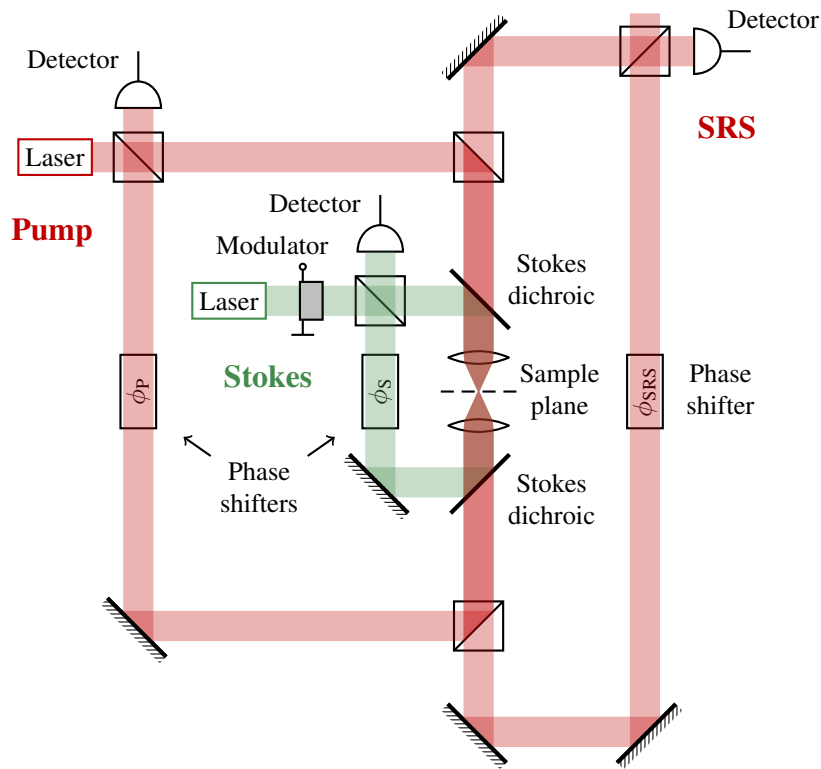
Fluorescence nanoscopy techniques involving 4π microscopy are the most light-efficient and the highest resolution approaches for three-dimensional live-cell imaging. 4π Raman microscopy, developed in this dissertation, has the potential to similarly help emerging super-resolution Raman imaging techniques to go further in terms of imaging resolution for biological samples.

7.2 Future perspectives

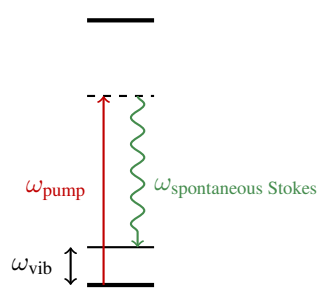
In this section we collect the improvements that we have been discussing along the different chapters of this thesis and suggest some new ones, hoping they will be of help in future research on the topic.

- **Thermal effects**

Phase variations and drifts of the piezo stages due to thermal effects limit the phase stabilization sensitivity and induce pump and Raman intensity changes over time as the optical components get misaligned. Enclosing all the optics inside the same microscope stand in a compact way could mitigate both



Spontaneous Raman



Stimulated Raman Scattering

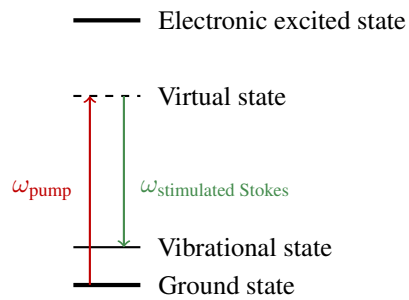
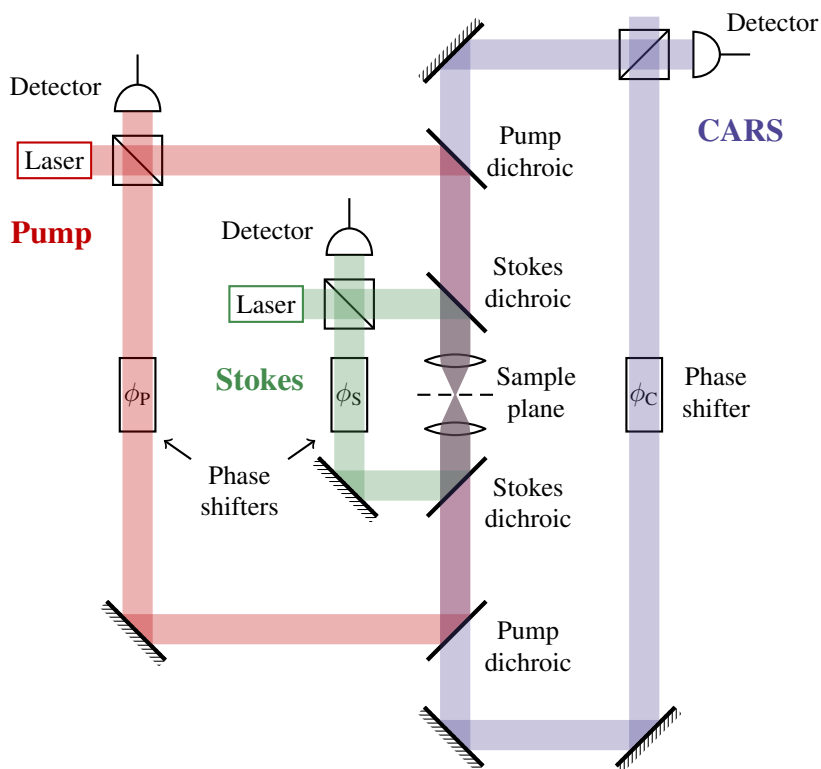


Figure 7.1: Tentative optical schematic of a 4π Type-C SRS microscope as a future option to remove the secondary lobes of 4π Raman microscopy and enhance the Raman signal collected. The energy diagrams of spontaneous and stimulated Raman scattering are shown at the bottom.



Coherent anti-Stokes Raman

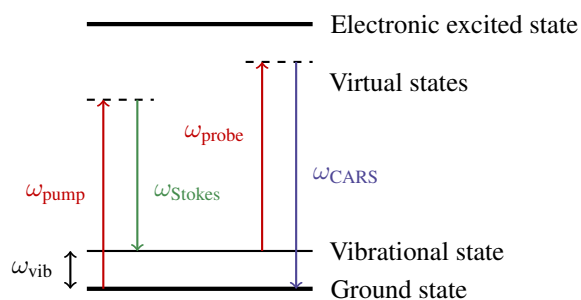


Figure 7.2: Tentative optical schematic of a 4π Type-C CARS microscope as a future option to remove the secondary lobes of 4π Raman microscopy and enhance the Raman signal collected. The pump laser also acts as the probe. The corresponding energy diagram is shown at the bottom.

issues. Ideally, a good thermal isolation would render the phase stabilization unnecessary.

- **Quantitative-phase and Raman microscope modalities**

The presence of phase fluctuations in the system, with which we dealt in the previous point, is also the factor preventing a simultaneous measurement of the quantitative phase and Raman signals.

Instead of obtaining simultaneous phase and Raman images, in some occasions a more interesting approach might be to obtain a broad and quick quantitative phase image of the sample to preselect the points that will be later studied with the slower Raman modality of the 4π microscope. In this regard, the system is currently greatly limited in speed due to the slow communication between the scanning piezo stage and the computer. A ramp generator could be directly connected to the scanning piezo, completely avoiding the slow communication through a PC, potentially reaching speeds for 10 μm line scans like the ones presented in this thesis in the order of 100 milliseconds or less.

- **Sidelobes**

We have taken many axial scans of biological samples aiming at demonstrating the improved resolution of 4π microscopy, but the secondary lobes do not let us see any resolution enhancement compared to conventional confocal microscopy. Moreover, to do a deconvolution we need secondary lobes smaller than 50%, much smaller than the lobes of our microscope.

The next natural step to continue this topic would be to remove the secondary lobes with a 4π Type C Raman microscope. However, this is probably not enough to sufficiently mitigate the sidelobes. The best results in 4π fluorescence microscopy have been obtained with two-photon excitation, so a coherent Raman Type C 4π microscopy would likely be required. Stimulated Raman Scattering (SRS) or Coherent Anti-Stokes Raman Spectroscopy (CARS), illustrated in Fig. 7.2, would be viable options. They are considered as multiphoton techniques so they would resemble the two-photon excitation often employed in 4π fluorescence microscopy, except for the fact that two lasers would be needed for the excitation part. The challenge would then be dispersion or optical path management between both excitation wavelengths and the Raman signal, as well as fulfilling the phase matching condition for both exciting lasers. However, we note that under tightly focused conditions the phase matching condition is generally not a constraint.

A rough calculation in [129] can help us compare continuous-wave excitation and pulsed-wave excitation SRS. The pulsed laser beam considered has a Gaussian temporal shape and the pump beam has the same pulse width as

the Stokes beam. The same average power is assumed for the pulsed laser and the continuous-wave laser. Under these circumstances, continuous-wave laser excitation would decrease the signal level by $1.3 \cdot 10^3$ times compared to pulsed excitation by a laser source typically employed for SRS applications (5 picoseconds pulse length, 80 MHz repetition rate). CARS can also yield a Raman signal enhancement, but it is only better than spontaneous Raman after a certain power threshold, which normally entails employing expensive pulsed sources with at least kilowatt peak power.

In conclusion, there is ample room for improvements and many options to be explored. A tentative outline for future research could start by exploring the simplest but less powerful approaches, and then increasingly more complex options. Namely, 4π Type C spontaneous Raman microscopy could be explored first, to then investigate 4π Type A, B or C continuous-wave stimulated Raman scattering, 4π Type A, B or C pulsed-wave stimulated Raman scattering and 4π Type A, B or C CARS microscopy.

4π microscopy provides the best axial resolution possible by solely optical means. As soon as the challenge of removing the secondary lobes is tackled, it will be an enabling approach for label-free biological imaging and super-resolution Raman applications.



The Matrix Transfer Method to Analyze Multilayer Stacks

The matrix transfer method is commonly used to analyze stacks of dielectric layers, as shown in Fig. A.1. The transfer matrix formulation can solve the amplitude and phase of the reflected and transmitted beams. Here we will be considering the case of a TE polarized plane wave incident on the stack. This means that the electric field of the electromagnetic wave will always be parallel to the interfaces, which are in the xy -plane of the drawing.

Each layer can be seen as a system of one input and one output port, which can be represented with a matrix of complex values. The complex valued refractive indices of the layers and their thicknesses fully define the problem. By cascading the matrices corresponding to the individual layers in the proper order, a matrix for the whole system can be built.

Figure A.2 shows an schematic representation of the problem with the definition of the variables we will be using in this formulation. Each layer has a refractive index n_i and a thickness d_i . For the TE incident wave, we can always choose to place the electric field of the electromagnetic wave in the x axis, such that the only angle of propagating that needs consideration is contained in the yz -plane. Within layer i , we term that angle θ_i . Additionally, the location of the interface between medium i and $i + 1$ will be referenced as z_i .

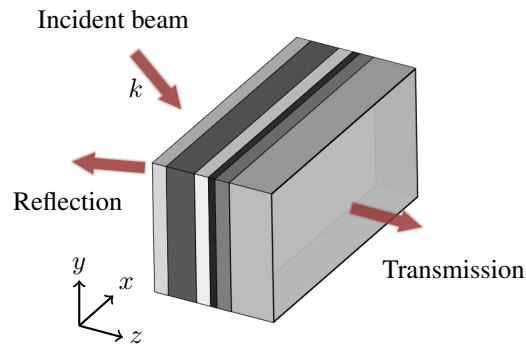


Figure A.1: A beam incident into a stack of dielectric layers with wave vector k gets reflected and transmitted. The transfer matrix formulation can be used to solve the amplitude and phase of the reflected and transmitted beams.

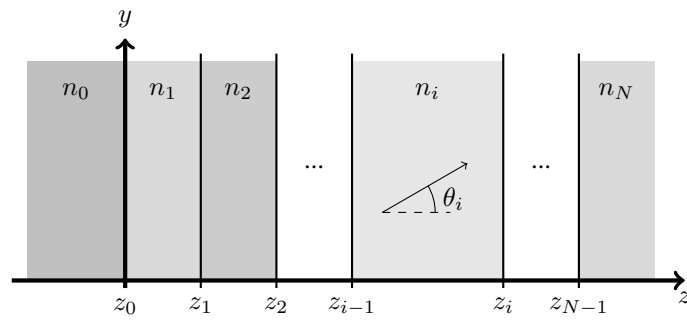


Figure A.2: Stack of $N + 1$ layers with different refractive indices $n_0 \dots n_N$. The propagation angle in layer i is indicated as θ_i .

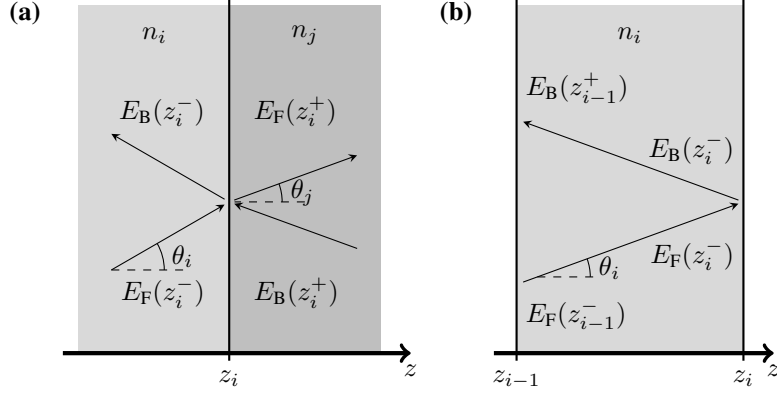


Figure A.3: (a) Reflected and transmitted beams at interface i , between layer i and j .
(b) Beams propagating through layer i

We make a distinction between the forward propagating waves (towards increasing z) and backward propagating waves (towards decreasing z) with the subscripts F and B, respectively. We also use the superscripts $-$ and $+$ to refer to a position right before a certain interface or right after, respectively. Thus, the complete transfer matrix T relates the complex amplitudes E_F and E_B right before and right behind the first and last interfaces of the stack.

$$\begin{bmatrix} E_F(z_0^-) \\ E_B(z_0^-) \end{bmatrix} = T \begin{bmatrix} E_F(z_{N-1}^+) \\ E_B(z_{N-1}^+) \end{bmatrix} \quad (\text{A.1})$$

First, we focus on building a transfer matrix for a single layer T_i , using the illustration in Fig. A.3(a). We need to apply the boundary conditions for the interfaces and consider the propagation between them, and both can be applied in a matrix form. If we call I_i the transfer matrix corresponding to the interface i , and P_i the matrix corresponding to the propagation within layer i , then we can define T_i as

$$T_i = I_{i-1} P_i I_i \quad (\text{A.2})$$

In order to understand how to define the interface matrices I , consider a single interface i . The relationship between the amplitudes of the forward and backward propagating waves, just before and just behind the interface, is the following

$$\begin{bmatrix} E_F(z_i^+) \\ E_B(z_i^-) \end{bmatrix} = \begin{bmatrix} t_{i(i+1)} & r_{(i+1)i} \\ r_{i(i+1)} & t_{(i+1)i} \end{bmatrix} \begin{bmatrix} E_F(z_i^-) \\ E_B(z_i^+) \end{bmatrix} \quad (\text{A.3})$$

where t and r are the complex Fresnel coefficients, valid for a single incident

wave on an interface. For a TE polarized wave they are

$$\begin{aligned} r_{i(i+1)} &= \frac{E_B(z_i^-)}{E_F(z_i^-)} = \frac{n_i \cos \theta_i - n_{(i+1)} \cos \theta_{(i+1)}}{n_i \cos \theta_i + n_{(i+1)} \cos \theta_{(i+1)}} \\ t_{i(i+1)} &= \frac{E_F(z_i^+)}{E_F(z_i^-)} = 1 + r_{i(i+1)} = \frac{2n_i \cos \theta_i}{n_i \cos \theta_i + n_{(i+1)} \cos \theta_{(i+1)}} \end{aligned} \quad (\text{A.4})$$

Fresnel coefficients have the following symmetry relations that we will later use to simplify expressions

$$\begin{aligned} r_{i(i+1)} &= -r_{(i+1)i} \\ t_{i(i+1)} t_{(i+1)i} - r_{i(i+1)} r_{(i+1)i} &= 1 \end{aligned} \quad (\text{A.5})$$

Equations A.3 are not in a form that we can cascade with other matrices. However, they can be rewritten to relate the forward and backward propagating waves in layer i with the forward and backward propagating waves in layer $i + 1$, which is in the form that we wanted

$$\begin{bmatrix} E_F(z_i^-) \\ E_B(z_i^-) \end{bmatrix} = \begin{bmatrix} \frac{1}{t_{i(i+1)}} & -\frac{r_{(i+1)i}}{t_{i(i+1)}} \\ \frac{r_{i(i+1)}}{t_{i(i+1)}} & t_{i(i+1)} - \frac{r_{i(i+1)}}{t_{i(i+1)}} r_{(i+1)i} \end{bmatrix} \begin{bmatrix} E_F(z_i^+) \\ E_B(z_i^+) \end{bmatrix} \quad (\text{A.6})$$

Now, we can simplify these equations by using the previous symmetry relationships in Eq. A.5, to obtain the following

$$\begin{bmatrix} E_F(z_i^-) \\ E_B(z_i^-) \end{bmatrix} = \frac{1}{t_{i(i+1)}} \begin{bmatrix} 1 & r_{i(i+1)} \\ r_{i(i+1)} & 1 \end{bmatrix} \begin{bmatrix} E_F(z_i^+) \\ E_B(z_i^+) \end{bmatrix} \quad (\text{A.7})$$

The result is the definition for the matrix I_i , which serves to propagate the wave between medium i and medium $(i + 1)$

$$I_i = \frac{1}{t_{i(i+1)}} \begin{bmatrix} 1 & r_{i(i+1)} \\ r_{i(i+1)} & 1 \end{bmatrix} \quad (\text{A.8})$$

In order to define the complete matrix for a complete layer, we still need to build the transfer matrix for the wave propagation through it, as illustrated in Fig. A.3(b). We can propagate the forward and backward waves between interfaces with the following equations

$$\begin{aligned} E_F(z_i^-) &= E_F(z_{i-1}^+) e^{-j\Phi_i} \\ E_B(z_{i-1}^+) &= E_B(z_i^-) e^{-j\Phi_i} \end{aligned} \quad (\text{A.9})$$

which directly gives the definition of the propagating matrix P_i

$$P_i = \begin{bmatrix} e^{j\Phi_i} & 0 \\ 0 & e^{-j\Phi_i} \end{bmatrix} \quad (\text{A.10})$$

where the phase shift Φ_i suffered by the wave, with wavelength in vacuum λ_0 , in layer i , is given by

$$\Phi_i = \frac{2\pi}{\lambda_0} n_i d_i \cos \theta_i \quad (\text{A.11})$$

Finally, we can obtain the complete transfer matrix T of a multilayer stack by extending the previous discussion for a single layer. Instead of having two matrices for the interfaces, plus another one for the propagation between them, now we have to cascade all the individual matrices for all the interfaces and for the propagation in between.

$$T = I_0 P_1 I_1 P_2 \dots P_{(N-1)} I_{(N-1)} \quad (\text{A.12})$$

References

- [1] S. Hell and E. H. Stelzer, "Fundamental improvement of resolution with a 4pi-confocal fluorescence microscope using two-photon excitation," *Optics Communications*, vol. 93, no. 5-6, pp. 277–282, 1992.
- [2] S. Hell and E. H. Stelzer, "Properties of a 4pi confocal fluorescence microscope," *JOSA A*, vol. 9, no. 12, pp. 2159–2166, 1992.
- [3] M. Schrader and S. Hell, "4pi-confocal images with axial superresolution," *Journal of Microscopy*, vol. 183, no. 2, pp. 110–115, 1996.
- [4] S. Hell, M. Schrader, and H. Van Der Voort, "Far-field fluorescence microscopy with three-dimensional resolution in the 100-nm range," *Journal of microscopy*, vol. 187, no. 1, pp. 1–7, 1997.
- [5] H. Gugel, J. Bewersdorf, S. Jakobs, J. Engelhardt, R. Storz, and S. W. Hell, "Cooperative 4pi excitation and detection yields sevenfold sharper optical sections in live-cell microscopy," *Biophysical journal*, vol. 87, no. 6, pp. 4146–4152, 2004.
- [6] M. G. Gustafsson, D. A. Agard, and J. W. Sedat, "Sevenfold improvement of axial resolution in 3d wide-field microscopy using two objective lenses," in *Three-Dimensional Microscopy: Image Acquisition and Processing II*, vol. 2412, pp. 147–157, International Society for Optics and Photonics, 1995.
- [7] S. Hell, M. Schrader, and H. Van Der Voort, "Far-field fluorescence microscopy with three-dimensional resolution in the 100-nm range," *Journal of microscopy*, vol. 187, no. 1, pp. 1–7, 1997.
- [8] H. Kano, S. Jakobs, M. Nagorni, and S. W. Hell, "Dual-color 4pi-confocal microscopy with 3d-resolution in the 100 nm range," *Ultramicroscopy*, vol. 90, no. 2-3, pp. 207–213, 2002.
- [9] U. Böhm, S. W. Hell, and R. Schmidt, "4pi-resolft nanoscopy," *Nature communications*, vol. 7, p. 10504, 2016.

- [10] G. Shtengel, J. A. Galbraith, C. G. Galbraith, J. Lippincott-Schwartz, J. M. Gillette, S. Manley, R. Sougrat, C. M. Waterman, P. Kanchanawong, M. W. Davidson, *et al.*, “Interferometric fluorescent super-resolution microscopy resolves 3d cellular ultrastructure,” *Proceedings of the National Academy of Sciences*, vol. 106, no. 9, pp. 3125–3130, 2009.
- [11] R. Schmidt, C. A. Wurm, S. Jakobs, J. Engelhardt, A. Egner, and S. W. Hell, “Spherical nanosized focal spot unravels the interior of cells,” *Nature methods*, vol. 5, no. 6, p. 539, 2008.
- [12] S. W. Hell, “Double-confocal scanning microscope,” Dec. 18 1990. European Patent Office EP0491289 (A1).
- [13] S. W. Hell, R. Schmidt, and A. Egner, “Diffraction-unlimited three-dimensional optical nanoscopy with opposing lenses,” *Nature Photonics*, vol. 3, no. 7, p. 381, 2009.
- [14] S. W. Hell, “Far-field optical nanoscopy,” *science*, vol. 316, no. 5828, pp. 1153–1158, 2007.
- [15] S. L. Veatch, S. S. Leung, R. E. Hancock, and J. L. Thewalt, “Fluorescent probes alter miscibility phase boundaries in ternary vesicles,” *The Journal of Physical Chemistry B*, vol. 111, no. 3, pp. 502–504, 2007.
- [16] M. J. Skaug, M. L. Longo, and R. Faller, “The impact of texas red on lipid bilayer properties,” *The Journal of Physical Chemistry B*, vol. 115, no. 26, pp. 8500–8505, 2011.
- [17] C. Krafft and J. Popp, “The many facets of raman spectroscopy for biomedical analysis,” *Analytical and bioanalytical chemistry*, vol. 407, no. 3, pp. 699–717, 2015.
- [18] A. Yashchenok, A. Masic, D. Gorin, B. S. Shim, N. A. Kotov, P. Fratzl, H. Möhwald, and A. Skirtach, “Nanoengineered colloidal probes for raman-based detection of biomolecules inside living cells,” *Small*, vol. 9, no. 3, pp. 351–356, 2013.
- [19] K. Watanabe, A. F. Palonpon, N. I. Smith, A. Kasai, H. Hashimoto, S. Kawata, K. Fujita, *et al.*, “Structured line illumination raman microscopy,” *Nature communications*, vol. 6, p. 10095, 2015.
- [20] C. Neumann, S. Reichardt, P. Venezuela, M. Drögeler, L. Banszerus, M. Schmitz, K. Watanabe, T. Taniguchi, F. Mauri, B. Beschoten, *et al.*, “Raman spectroscopy as probe of nanometre-scale strain variations in graphene,” *Nature communications*, vol. 6, p. 8429, 2015.

- [21] W. R. Silva, C. T. Graefe, and R. R. Frontiera, "Toward label-free super-resolution microscopy," *Acs Photonics*, vol. 3, no. 1, pp. 79–86, 2015.
- [22] L. Langelüddecke, P. Singh, and V. Deckert, "Exploring the nanoscale: fifteen years of tip-enhanced raman spectroscopy," *Applied spectroscopy*, vol. 69, no. 12, pp. 1357–1371, 2015.
- [23] C. Sheppard, "Depth of field in optical microscopy," *Journal of Microscopy*, vol. 149, no. 1, pp. 73–75, 1988.
- [24] D. Long, *The Raman Effect: A Unified Treatment of the Theory of Raman Scattering by Molecules*. Wiley, 2002.
- [25] C. W. Freudiger, W. Min, B. G. Saar, S. Lu, G. R. Holtom, C. He, J. C. Tsai, J. X. Kang, and X. S. Xie, "Label-free biomedical imaging with high sensitivity by stimulated raman scattering microscopy," *Science*, vol. 322, no. 5909, pp. 1857–1861, 2008.
- [26] P. Maker and R. Terhune, "Study of optical effects due to an induced polarization third order in the electric field strength," *Physical Review*, vol. 137, no. 3A, p. A801, 1965.
- [27] M. Müller and A. Zumbusch, "Coherent anti-stokes raman scattering microscopy," *ChemPhysChem*, vol. 8, no. 15, pp. 2156–2170, 2007.
- [28] M. Müller and A. Zumbusch, "Coherent anti-stokes raman scattering microscopy," *ChemPhysChem*, vol. 8, no. 15, pp. 2156–2170, 2007.
- [29] D. Cialla, A. März, R. Böhme, F. Theil, K. Weber, M. Schmitt, and J. Popp, "Surface-enhanced raman spectroscopy (sers): progress and trends," *Analytical and bioanalytical chemistry*, vol. 403, no. 1, pp. 27–54, 2012.
- [30] G. I. Petrov, R. Arora, V. V. Yakovlev, X. Wang, A. V. Sokolov, and M. O. Scully, "Comparison of coherent and spontaneous raman microspectroscopies for noninvasive detection of single bacterial endospores," *Proceedings of the National Academy of Sciences*, vol. 104, no. 19, pp. 7776–7779, 2007.
- [31] N. Banaei, A. Foley, J. M. Houghton, Y. Sun, and B. Kim, "Multiplex detection of pancreatic cancer biomarkers using a sers-based immunoassay," *Nanotechnology*, vol. 28, no. 45, p. 455101, 2017.
- [32] S. Ayas, G. Cinar, A. D. Ozkan, Z. Soran, O. Ekiz, D. Kocaay, A. Tomak, P. Toren, Y. Kaya, I. Tunc, *et al.*, "Label-free nanometer-resolution imaging of biological architectures through surface enhanced raman scattering," *Scientific reports*, vol. 3, p. 2624, 2013.

- [33] E. Cortés, P. G. Etchegoin, E. C. Le Ru, A. Fainstein, M. E. Vela, and R. C. Salvarezza, "Monitoring the electrochemistry of single molecules by surface-enhanced raman spectroscopy," *Journal of the American Chemical Society*, vol. 132, no. 51, pp. 18034–18037, 2010.
- [34] P. C. Wuytens, A. Z. Subramanian, W. H. De Vos, A. G. Skirtach, and R. Baets, "Gold nanodome-patterned microchips for intracellular surface-enhanced raman spectroscopy," *Analyst*, vol. 140, no. 24, pp. 8080–8087, 2015.
- [35] A. J. Berger, I. Itzkan, and M. S. Feld, "Feasibility of measuring blood glucose concentration by near-infrared raman spectroscopy," *Spectrochimica Acta Part A: Molecular and Biomolecular Spectroscopy*, vol. 53, no. 2, pp. 287–292, 1997.
- [36] Y. C. Cao, R. Jin, and C. A. Mirkin, "Nanoparticles with raman spectroscopic fingerprints for dna and rna detection," *Science*, vol. 297, no. 5586, pp. 1536–1540, 2002.
- [37] T. C. B. Schut, P. J. Caspers, G. J. Puppels, A. Nijssen, F. Heule, M. H. Neumann, and D. P. Hayes, "Discriminating basal cell carcinoma from its surrounding tissue by raman spectroscopy," *Journal of Investigative Dermatology*, vol. 119, no. 1, pp. 64–69, 2002.
- [38] L. A. Austin, S. Osseiran, and C. L. Evans, "Raman technologies in cancer diagnostics," *Analyst*, vol. 141, no. 2, pp. 476–503, 2016.
- [39] S. K. Paidi, A. Rizwan, C. Zheng, M. Cheng, K. Glunde, and I. Barman, "Label-free raman spectroscopy detects stromal adaptations in premetastatic lungs primed by breast cancer," *Cancer research*, vol. 77, no. 2, pp. 247–256, 2017.
- [40] R. Pandey, S. K. Paidi, T. A. Valdez, C. Zhang, N. Spegazzini, R. R. Dasari, and I. Barman, "Noninvasive monitoring of blood glucose with raman spectroscopy," *Accounts of chemical research*, vol. 50, no. 2, pp. 264–272, 2017.
- [41] R. J. Swain, S. J. Kemp, P. Goldstraw, T. D. Tetley, and M. M. Stevens, "Assessment of cell line models of primary human cells by raman spectral phenotyping," *Biophysical journal*, vol. 98, no. 8, pp. 1703–1711, 2010.
- [42] P. F. Bernath, *Spectra of atoms and molecules*. Oxford university press, 2015.
- [43] S. W. Hell, E. H. Stelzer, S. Lindek, and C. Cremer, "Confocal microscopy with an increased detection aperture: type-b 4pi confocal microscopy," *Optics letters*, vol. 19, no. 3, pp. 222–224, 1994.

- [44] S. W. Hell, S. Lindek, C. Cremer, and E. H. Stelzer, "Measurement of the 4pi-confocal point spread function proves 75 nm axial resolution," *Applied Physics Letters*, vol. 64, no. 11, pp. 1335–1337, 1994.
- [45] J. Pawley, *Handbook of biological confocal microscopy*. Springer Science & Business Media, 2006.
- [46] K. Bahlmann, S. Jakobs, and S. W. Hell, "4pi-confocal microscopy of live cells," *Ultramicroscopy*, vol. 87, no. 3, pp. 155–164, 2001.
- [47] A. Egner, S. Verrier, A. Goroshkov, H.-D. Söling, and S. W. Hell, "4pi-microscopy of the golgi apparatus in live mammalian cells," *Journal of structural biology*, vol. 147, no. 1, pp. 70–76, 2004.
- [48] A. Egner, S. Jakobs, and S. W. Hell, "Fast 100-nm resolution three-dimensional microscope reveals structural plasticity of mitochondria in live yeast," *Proceedings of the National Academy of Sciences*, vol. 99, no. 6, pp. 3370–3375, 2002.
- [49] X. Hao, J. Antonello, E. S. Allgeyer, J. Bewersdorf, and M. J. Booth, "Aberrations in 4pi microscopy," *Optics express*, vol. 25, no. 13, pp. 14049–14058, 2017.
- [50] M. Jang, A. Sentenac, and C. Yang, "Optical phase conjugation (opc)-assisted isotropic focusing," *Optics express*, vol. 21, no. 7, pp. 8781–8792, 2013.
- [51] A. Arkhipov and K. Schulten, "Limits for reduction of effective focal volume in multiple-beam light microscopy," *Optics express*, vol. 17, no. 4, pp. 2861–2870, 2009.
- [52] E. Mudry, E. Le Moal, P. Ferrand, P. C. Chaumet, and A. Sentenac, "Isotropic diffraction-limited focusing using a single objective lens," *Physical review letters*, vol. 105, no. 20, p. 203903, 2010.
- [53] S. W. Hell and M. Nagorni, "4pi confocal microscopy with alternate interference," *Optics letters*, vol. 23, no. 20, pp. 1567–1569, 1998.
- [54] C. M. Blanca, J. Bewersdorf, and S. W. Hell, "Determination of the unknown phase difference in 4pi-confocal microscopy through the image intensity," *Optics communications*, vol. 206, no. 4-6, pp. 281–285, 2002.
- [55] D. Baddeley, C. Carl, and C. Cremer, "4pi microscopy deconvolution with a variable point-spread function," *Applied optics*, vol. 45, no. 27, pp. 7056–7064, 2006.

- [56] A. Egner, M. Schrader, and S. W. Hell, "Refractive index mismatch induced intensity and phase variations in fluorescence confocal, multiphoton and 4pi-microscopy," *Optics communications*, vol. 153, no. 4-6, pp. 211–217, 1998.
- [57] G. Vicidomini, S. W. Hell, and A. Schönle, "Automatic deconvolution of 4pi-microscopy data with arbitrary phase," *Optics letters*, vol. 34, no. 22, pp. 3583–3585, 2009.
- [58] S. W. Hell, C. M. Blanca, and J. Bewersdorf, "Phase determination in interference-based superresolving microscopes through critical frequency analysis," *Optics letters*, vol. 27, no. 11, pp. 888–890, 2002.
- [59] M. Nagorni and S. W. Hell, "Coherent use of opposing lenses for axial resolution increase in fluorescence microscopy. i. comparative study of concepts," *JOSA A*, vol. 18, no. 1, pp. 36–48, 2001.
- [60] F. Huang, G. Sirinakis, E. S. Allgeyer, L. K. Schroeder, W. C. Duim, E. B. Kromann, T. Phan, F. E. Rivera-Molina, J. R. Myers, I. Irnov, *et al.*, "Ultra-high resolution 3d imaging of whole cells," *Cell*, vol. 166, no. 4, pp. 1028–1040, 2016.
- [61] J. Pawley, *Handbook of biological confocal microscopy*. Springer Science & Business Media, 2010.
- [62] B. R. Masters and B. R. Masters, *Confocal microscopy and multiphoton excitation microscopy: the genesis of live cell imaging*, vol. 161. SPIE press Bellingham, WA, 2006.
- [63] J. White, W. Amos, and M. Fordham, "An evaluation of confocal versus conventional imaging of biological structures by fluorescence light microscopy.," *The Journal of cell biology*, vol. 105, no. 1, pp. 41–48, 1987.
- [64] W. Denk, J. H. Strickler, and W. W. Webb, "Two-photon laser scanning fluorescence microscopy," *Science*, vol. 248, no. 4951, pp. 73–76, 1990.
- [65] S. W. Hell, S. Lindek, and E. H. Stelzer, "Enhancing the axial resolution in far-field light microscopy: Two-photon 4pi confocal fluorescence microscopy," *Journal of Modern Optics*, vol. 41, no. 4, pp. 675–681, 1994.
- [66] N. Sandeau and H. Giovannini, "Arrangement of a 4pi microscope for reducing the confocal detection volume with two-photon excitation," *Optics communications*, vol. 264, no. 1, pp. 123–129, 2006.
- [67] L. D. Ziegler, "Hyper-raman spectroscopy," *Journal of Raman Spectroscopy*, vol. 21, no. 12, pp. 769–779, 1990.

- [68] M. Schrader, K. Bahlmann, G. Giese, and S. W. Hell, "4pi-confocal imaging in fixed biological specimens," *Biophysical journal*, vol. 75, no. 4, pp. 1659–1668, 1998.
- [69] S. Lindek, N. Salmon, C. Cremer, and E. Stelzer, "Theta microscopy allows phase regulation in 4pi (a)-confocal two-photon fluorescence microscopy," *Optik*, vol. 98, pp. 15–20, 1994.
- [70] T. Vettenburg, H. I. Dalgarno, J. Nylk, C. Coll-Lladó, D. E. Ferrier, T. Čížmár, F. J. Gunn-Moore, and K. Dholakia, "Light-sheet microscopy using an airy beam," *Nature methods*, vol. 11, no. 5, p. 541, 2014.
- [71] S. W. Hell, S. Lindek, C. Cremer, and E. H. Stelzer, "Measurement of the 4pi-confocal point spread function proves 75 nm axial resolution," *Applied Physics Letters*, vol. 64, no. 11, pp. 1335–1337, 1994.
- [72] H. P. Kao and A. Verkman, "Tracking of single fluorescent particles in three dimensions: use of cylindrical optics to encode particle position," *Biophysical journal*, vol. 67, no. 3, pp. 1291–1300, 1994.
- [73] B. Huang, W. Wang, M. Bates, and X. Zhuang, "Three-dimensional super-resolution imaging by stochastic optical reconstruction microscopy," *Science*, vol. 319, no. 5864, pp. 810–813, 2008.
- [74] R. E. Bartolo, A. B. Tveten, and A. Dandridge, "Thermal phase noise measurements in optical fiber interferometers," *IEEE Journal of Quantum Electronics*, vol. 48, no. 5, pp. 720–727, 2012.
- [75] J. Martinez-Carranza, K. Falaggis, and T. Kozacki, "Fast and accurate phase-unwrapping algorithm based on the transport of intensity equation," *Appl. Opt.*, vol. 56, pp. 7079–7088, Sep 2017.
- [76] V. V. Krishnamachari, E. R. Andresen, S. R. Keiding, and E. O. Potma, "An active interferometer-stabilization scheme with linear phase control," *Optics Express*, vol. 14, no. 12, pp. 5210–5215, 2006.
- [77] G. Jotzu, T. J. Bartley, H. B. Coldenstrodt-Ronge, B. J. Smith, and I. A. Walmsley, "Continuous phase stabilization and active interferometer control using two modes," *Journal of Modern Optics*, vol. 59, no. 1, pp. 42–45, 2012.
- [78] M. Wehner, M. Ulm, and M. Wegener, "Scanning interferometer stabilized by use of pancharatnam's phase," *Optics letters*, vol. 22, no. 19, pp. 1455–1457, 1997.

- [79] M. A. Choma, C. Yang, and J. A. Izatt, “Instantaneous quadrature low-coherence interferometry with 3×3 fiber-optic couplers,” *Optics letters*, vol. 28, no. 22, pp. 2162–2164, 2003.
- [80] D. Xu, F. Yang, D. Chen, F. Wei, H. Cai, Z. Fang, and R. Qu, “Laser phase and frequency noise measurement by michelson interferometer composed of a 3×3 optical fiber coupler,” *Optics express*, vol. 23, no. 17, pp. 22386–22393, 2015.
- [81] D. Wu, R.-h. Zhu, L. Chen, and J.-y. Li, “Transverse spatial phase-shifting method used in vibration-compensated interferometer,” *Optik-International Journal for Light and Electron Optics*, vol. 115, no. 8, pp. 343–346, 2004.
- [82] A. Freschi and J. Frejlich, “Adjustable phase control in stabilized interferometry,” *Optics letters*, vol. 20, no. 6, pp. 635–637, 1995.
- [83] A. Rosenthal, S. Kellnberger, G. Sergiadis, and V. Ntziachristos, “Wide-band fiber-interferometer stabilization with variable phase,” *IEEE Photonics Technology Letters*, vol. 24, no. 17, pp. 1499–1501, 2012.
- [84] S.-B. Cho and T.-G. Noh, “Stabilization of a long-armed fiber-optic single-photon interferometer,” *Optics express*, vol. 17, no. 21, pp. 19027–19032, 2009.
- [85] D. Grassani, M. Galli, and D. Bajoni, “Active stabilization of a michelson interferometer at an arbitrary phase with subnanometer resolution,” *Optics letters*, vol. 39, no. 8, pp. 2530–2533, 2014.
- [86] M. J. Rust, M. Bates, and X. Zhuang, “Sub-diffraction-limit imaging by stochastic optical reconstruction microscopy (storm),” *Nature methods*, vol. 3, no. 10, p. 793, 2006.
- [87] X. Zhuang, “Nano-imaging with storm,” *Nature photonics*, vol. 3, no. 7, p. 365, 2009.
- [88] M. Heilemann, S. Van De Linde, M. Schüttelz, R. Kasper, B. Seefeldt, A. Mukherjee, P. Tinnefeld, and M. Sauer, “Subdiffraction-resolution fluorescence imaging with conventional fluorescent probes,” *Angewandte Chemie International Edition*, vol. 47, no. 33, pp. 6172–6176, 2008.
- [89] E. Betzig, G. H. Patterson, R. Sougrat, O. W. Lindwasser, S. Olenych, J. S. Bonifacino, M. W. Davidson, J. Lippincott-Schwartz, and H. F. Hess, “Imaging intracellular fluorescent proteins at nanometer resolution,” *Science*, vol. 313, no. 5793, pp. 1642–1645, 2006.

- [90] S. T. Hess, T. P. Girirajan, and M. D. Mason, "Ultra-high resolution imaging by fluorescence photoactivation localization microscopy," *Biophysical journal*, vol. 91, no. 11, pp. 4258–4272, 2006.
- [91] J. Fölling, V. Belov, R. Kunetsky, R. Medda, A. Schönle, A. Egner, C. Eggeling, M. Bossi, and S. e. Hell, "Photochromic rhodamines provide nanoscopy with optical sectioning," *Angewandte Chemie International Edition*, vol. 46, no. 33, pp. 6266–6270, 2007.
- [92] A. Egner, C. Geisler, C. Von Middendorff, H. Bock, D. Wenzel, R. Medda, M. Andresen, A. C. Stiel, S. Jakobs, C. Eggeling, *et al.*, "Fluorescence nanoscopy in whole cells by asynchronous localization of photoswitching emitters," *Biophysical journal*, vol. 93, no. 9, pp. 3285–3290, 2007.
- [93] S. W. Hell and J. Wichmann, "Breaking the diffraction resolution limit by stimulated emission: stimulated-emission-depletion fluorescence microscopy," *Optics letters*, vol. 19, no. 11, pp. 780–782, 1994.
- [94] T. Müller, C. Schumann, and A. Kraegeloh, "Sted microscopy and its applications: new insights into cellular processes on the nanoscale," *ChemPhysChem*, vol. 13, no. 8, pp. 1986–2000, 2012.
- [95] J. Liu, S. Tang, Y. Lu, G. Cai, S. Liang, W. Wang, and X. Chen, "Synthesis of mo 2 n nanolayer coated moo 2 hollow nanostructures as high-performance anode materials for lithium-ion batteries," *Energy & Environmental Science*, vol. 6, no. 9, pp. 2691–2697, 2013.
- [96] D. Nesheva, M. # 138cepanovic, S. Askrabic, Z. Levi, I. Bineva, and Z. Popovic, "Raman scattering from znse nanolayers," *Acta Physica Polonica-Series A General Physics*, vol. 116, no. 1, p. 75, 2009.
- [97] M. Choi, K.-G. Kim, J. Heo, H. Jeong, S. Y. Kim, and J. Hong, "Multilayered graphene nano-film for controlled protein delivery by desired electro-stimuli," *Scientific reports*, vol. 5, p. 17631, 2015.
- [98] H. Vogel and F. Jähnig, "Models for the structure of outer-membrane proteins of escherichia coli derived from raman spectroscopy and prediction methods," *Journal of molecular biology*, vol. 190, no. 2, pp. 191–199, 1986.
- [99] J. Ando, A. F. Palonpon, M. Sodeoka, and K. Fujita, "High-speed raman imaging of cellular processes," *Current opinion in chemical biology*, vol. 33, pp. 16–24, 2016.
- [100] C. Conti, M. Realini, C. Colombo, A. Botteon, M. Bertasa, J. Striova, M. Barucci, and P. Matousek, "Determination of thickness of thin turbid

- painted over-layers using micro-scale spatially offset raman spectroscopy,” *Philosophical Transactions of the Royal Society A: Mathematical, Physical and Engineering Sciences*, vol. 374, no. 2082, p. 20160049, 2016.
- [101] K. Saurav, S. Kumari, and N. Le Thomas, “Cmos fabricated large array of free standing substrate-less photonic crystal cavities for biosensing applications,” *IEEE Photonics Journal*, vol. 9, no. 2, pp. 1–8, 2017.
- [102] D. E. Aspnes and A. Studna, “Dielectric functions and optical parameters of si, ge, gap, gaas, inp, inas, and insb from 1.5 to 6.0 ev,” *Physical review B*, vol. 27, no. 2, p. 985, 1983.
- [103] S. W. Hell, R. Schmidt, and A. Egner, “Diffraction-unlimited three-dimensional optical nanoscopy with opposing lenses,” *Nature Photonics*, vol. 3, no. 7, p. 381, 2009.
- [104] A. Rothen, “The ellipsometer, an apparatus to measure thicknesses of thin surface films,” *Rev. Sci. Instrum.*, vol. volume **, 1945.
- [105] T. D. Pollard, W. C. Earnshaw, J. Lippincott-Schwartz, and G. Johnson, *Cell Biology E-Book*. Elsevier Health Sciences, 2016.
- [106] Y. Shen, F. Hu, and W. Min, “Raman imaging of small biomolecules,” *Annual review of biophysics*, vol. 48, pp. 347–369, 2019.
- [107] A. Syed and E. A. Smith, “Raman imaging in cell membranes, lipid-rich organelles, and lipid bilayers,” *Annual Review of Analytical Chemistry*, vol. 10, pp. 271–291, 2017.
- [108] J. Schilling, K. Sengupta, S. Goennenwein, A. R. Bausch, and E. Sackmann, “Absolute interfacial distance measurements by dual-wavelength reflection interference contrast microscopy,” *Physical Review E*, vol. 69, no. 2, p. 021901, 2004.
- [109] P. Wang, R. Bista, R. Bhargava, R. E. Brand, and Y. Liu, “Spatial-domain low-coherence quantitative phase microscopy for cancer diagnosis,” *Optics letters*, vol. 35, no. 17, pp. 2840–2842, 2010.
- [110] B. Rappaz, E. Cano, T. Colomb, J. Kuhn, C. D. Depeursinge, V. Simanis, P. J. Magistretti, and P. P. Marquet, “Noninvasive characterization of the fission yeast cell cycle by monitoring dry mass with digital holographic microscopy,” *Journal of biomedical optics*, vol. 14, no. 3, p. 034049, 2009.
- [111] K. J. Chalut, A. E. Ekpenyong, W. L. Clegg, I. C. Melhuish, and J. Guck, “Quantifying cellular differentiation by physical phenotype using digital holographic microscopy,” *Integrative biology*, vol. 4, no. 3, pp. 280–284, 2012.

- [112] L. Kastl, M. Isbach, D. Dirksen, J. Schnekenburger, and B. Kemper, "Quantitative phase imaging for cell culture quality control," *Cytometry Part A*, vol. 91, no. 5, pp. 470–481, 2017.
- [113] K. Lee, K. Kim, J. Jung, J. Heo, S. Cho, S. Lee, G. Chang, Y. Jo, H. Park, and Y. Park, "Quantitative phase imaging techniques for the study of cell pathophysiology: from principles to applications," *Sensors*, vol. 13, no. 4, pp. 4170–4191, 2013.
- [114] H.-J. van Manen, Y. M. Kraan, D. Roos, and C. Otto, "Single-cell raman and fluorescence microscopy reveal the association of lipid bodies with phagosomes in leukocytes," *Proceedings of the National Academy of Sciences*, vol. 102, no. 29, pp. 10159–10164, 2005.
- [115] C. Patil, J. Kalkman, D. J. Faber, J. S. Nyman, T. G. van Leeuwen, and A. Mahadevan-Jansen, "Integrated system for combined raman spectroscopy-spectral domain optical coherence tomography," *Journal of biomedical optics*, vol. 16, no. 1, p. 011007, 2011.
- [116] J. W. Kang, N. Lue, C.-R. Kong, I. Barman, N. C. Dingari, S. J. Goldfless, J. C. Niles, R. R. Dasari, and M. S. Feld, "Combined confocal raman and quantitative phase microscopy system for biomedical diagnosis," *Biomedical optics express*, vol. 2, no. 9, pp. 2484–2492, 2011.
- [117] J. Klossa, B. Wattelier, T. Happillon, D. Toubas, L. de Laulanie, V. Untereiner, P. Bon, and M. Manfait, "Quantitative phase imaging and raman microspectroscopy applied to malaria," in *Diagnostic pathology*, vol. 8, p. S42, BioMed Central, 2013.
- [118] S. Singh, S. Kang, J. W. Kang, P. T. So, R. R. Dasari, Z. Yaqoob, and I. Barman, "Label-free characterization of ultra violet-radiation-induced changes in skin fibroblasts with raman spectroscopy and quantitative phase microscopy," *Scientific reports*, vol. 7, no. 1, p. 10829, 2017.
- [119] N. Pavillon, A. J. Hobro, and N. I. Smith, "Cell optical density and molecular composition revealed by simultaneous multimodal label-free imaging," *Biophysical journal*, vol. 105, no. 5, pp. 1123–1132, 2013.
- [120] N. Pavillon and N. I. Smith, "Implementation of simultaneous quantitative phase with raman imaging," *EPJ Techniques and Instrumentation*, vol. 2, no. 1, p. 5, 2015.
- [121] D. Roitshtain, N. A. Turko, B. Javidi, and N. T. Shaked, "Flipping interferometry and its application for quantitative phase microscopy in a micro-channel," *Optics letters*, vol. 41, no. 10, pp. 2354–2357, 2016.

- [122] G. Popescu, Y. Park, N. Lue, C. Best-Popescu, L. Deflores, R. R. Dasari, M. S. Feld, and K. Badizadegan, "Optical imaging of cell mass and growth dynamics," *American Journal of Physiology-Cell Physiology*, vol. 295, no. 2, pp. C538–C544, 2008.
- [123] K. Edward, T. W. Mayes, B. Hocken, and F. Farahi, "Trimodal imaging system capable of quantitative phase imaging without 2π ambiguities," *Optics letters*, vol. 33, no. 3, pp. 216–218, 2008.
- [124] B. Bhaduri, H. Pham, M. Mir, and G. Popescu, "Diffraction phase microscopy with white light," *Optics letters*, vol. 37, no. 6, pp. 1094–1096, 2012.
- [125] J. Bewersdorf, R. Schmidt, and S. Hell, "Comparison of i5m and 4pi-microscopy," *Journal of microscopy*, vol. 222, no. 2, pp. 105–117, 2006.
- [126] M. G. Gustafsson, D. Agard, J. Sedat, *et al.*, "i5m: 3d widefield light microscopy with better than 100nm axial resolution," *Journal of microscopy*, vol. 195, no. 1, pp. 10–16, 1999.
- [127] L. Shao, B. Isaac, S. Uzawa, D. A. Agard, J. W. Sedat, and M. G. Gustafsson, "i5s: wide-field light microscopy with 100-nm-scale resolution in three dimensions," *Biophysical journal*, vol. 94, no. 12, pp. 4971–4983, 2008.
- [128] O. Haeberlé, C. Xu, A. Dieterlen, and S. Jacquy, "Multiple-objective microscopy with three-dimensional resolution near 100 nm and a long working distance," *Optics letters*, vol. 26, no. 21, pp. 1684–1686, 2001.
- [129] C.-R. Hu, M. N. Slipchenko, P. Wang, P. Wang, J. D. Lin, G. Simpson, B. Hu, and J.-X. Cheng, "Stimulated raman scattering imaging by continuous-wave laser excitation," *Optics letters*, vol. 38, no. 9, pp. 1479–1481, 2013.

